The Pennsylvania State University

The Graduate School

Department of Materials Science and Engineering

TEMPERATURE DEPENDENCE OF THE PIEZOELECTRIC RESPONSE OF LEAD ZIRCONATE TITANATE FILMS FOR MEMS APPLICATIONS

A Thesis in

Ceramic Science and Engineering

by

Richard A. Wolf Jr.

©2001 Richard A. Wolf Jr.

Submitted in Partial Fulfillment
of the Requirements
for the Degree of

Master of Science

December 2001

We approve the thesis of Richard A. Wolf Jr.

Date of Signature

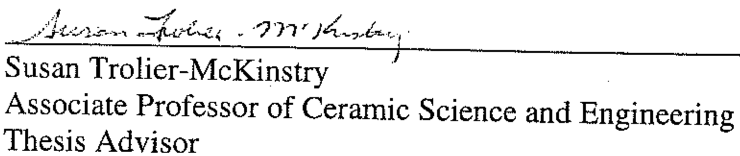

11-13-01

Susan Trolier-McKinstry
Associate Professor of Ceramic Science and Engineering
Thesis Advisor

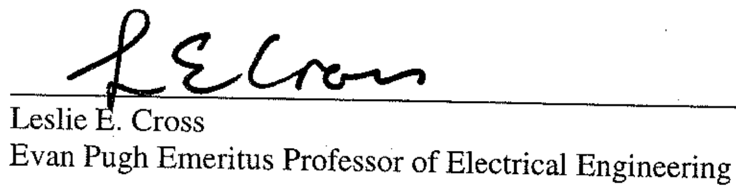

9th Nov 2001

Leslie E. Cross
Evan Pugh Emeritus Professor of Electrical Engineering

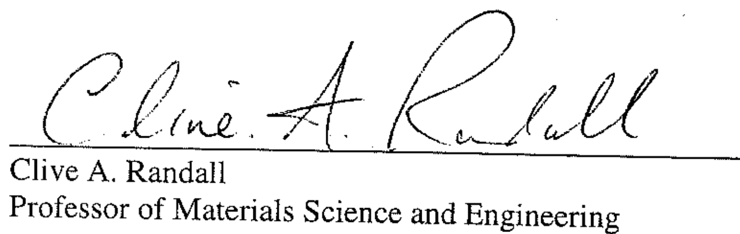

9 Nov 2001

Clive A. Randall
Professor of Materials Science and Engineering

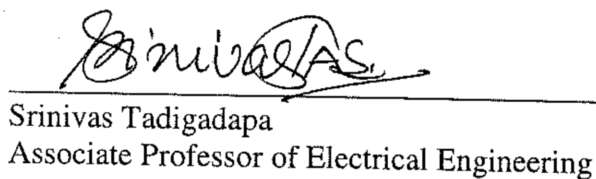

12 Nov. 2001.

Srinivas Tadigadapa
Associate Professor of Electrical Engineering

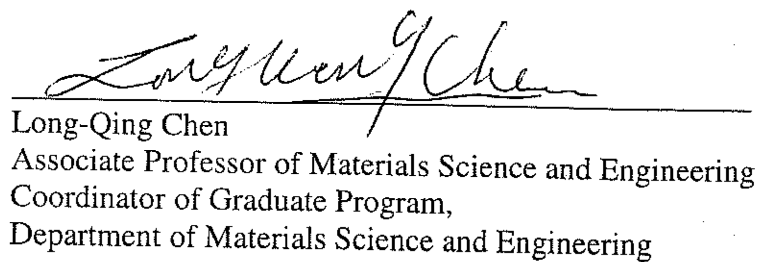

12 Nov. 2001

Long-Qing Chen
Associate Professor of Materials Science and Engineering
Coordinator of Graduate Program,
Department of Materials Science and Engineering

Abstract

Lead zirconate titanate (PZT) ferroelectric films are attractive for application as piezoelectrics in microelectromechanical systems (MEMS) as a result of their comparatively large piezoelectric coefficients. For effective utilization of PZT films in these devices, knowledge of the temperature dependence of their electromechanical response over the operating temperature range is necessary. However, to date, little data is available in the literature that reports on the piezoelectric behavior of PZT films as a function of temperature. The temperature dependence of the piezoelectric properties of PZT films may deviate from their bulk counterparts due to factors associated with clamping to a rigid substrate.

Thus, the goals of this research were (1) to design, fabricate, and characterize PZT film-based piezoelectric MEMS accelerometers with high resonance frequency (≥20 kHz) and charge sensitivity (≥1.0 pC/g), (2) to develop a method to measure the effective transverse piezoelectric coefficient ($e_{31,f}$) of films as a function of temperature between -55 and 85°C (a common MEMS device specification), and (3) to characterize the temperature dependence of $e_{31,f}$ of chemical solution processed PZT films of varying thickness and composition deposited on Pt/Ti/SiO_2/Si substrates.

MEMS accelerometers utilized 6 μm-thick chemical solution deposited PZT 52/48 films deposited on Pt-coated Si substrates. Devices were processed using standard silicon processing techniques and deep-trench reactive ion etching (DRIE). A tradeoff between sensitivity and resonance frequency was found to be closely related to the Si beam thickness below the active PZT layer. The highest measured sensitivity for a device with a resonance frequency ≥20 kHz was ~0.5 pC/g.

Additionally, the modified wafer flexure technique was developed to measure the effective transverse piezoelectric coefficient ($e_{31,f}$) of films as a function of temperature between -55 and 85°C. Resistive heating and liquid nitrogen-cooling of the uniform pressure rig enabled measurements above and below room temperature. The standard clamping condition was adjusted to account for the thermal expansion mismatch between film-coated substrate and pressure rig. A strain gage, thermocouple, and top electrode were positioned at the same radius near the center of the film-coated wafer during measurement. $e_{31,f}$ was calculated within the -55 to 85°C temperature range by simultaneously monitoring the piezoelectric charge output and strain in the film during wafer flexure.

This method was used to characterize the temperature dependence of $e_{31,f}$ in PZT films with 2 μm, 4 μm, and 6 μm thickness and 40/60, 52/48, and 60/40 Zr/Ti ratios. $|e_{31,f}|$ was found to increase with temperature and average increases were 46%, 32%, and 12% for films with PZT 60/40, 52/48, and 40/60 compositions, respectively. Measurement uncertainty ranged from ±3–12%. The measured temperature dependences of $e_{31,f}$ were consistent with the rapid rise in intrinsic d_{31} as T_c is approached, suggesting that they were controlled by intrinsic contributions.

Additional contributors to the measured variation in the PZT film piezoelectric response over the measured temperature range were identified. Changes in film elastic properties could have decreased measured $e_{31,f}$ values by 1–4% in heating from -55 to 85°C. Changes in the biaxial film stress with temperature were expected to account for 1–3% of the measured increase in $e_{31,f}$ from -55 to 85°C.

Table of Contents

List of Figures ... ix

List of Tables ... xvi

Acknowledgements ... xviii

Chapter 1 : Introduction ... 1

Chapter 2 : Literature Review ... 3

2.1 Introduction ... 3

2.2 Microelectromechanical Systems (MEMS) Devices ... 3
2.2.1 Figures of Merit for MEMS Applications ... 5
2.2.2 MEMS Accelerometers ... 7

2.3 Lead Zirconate Titanate ... 12
2.3.1 Ferroelectricity ... 12
2.3.1.1 Spontaneous Polarization ... 12
2.3.1.2 Polarization–Electric Field Hysteresis ... 13
2.3.1.3 Curie-Weiss Behavior ... 14
2.3.2 Characteristics of Lead Zirconate Titanate ... 15
2.3.2.1 Structural Features ... 15
2.3.2.2 Structure-Property Relations ... 17

2.4 Piezoelectricity ... 19
2.4.1 Fundamentals ... 19
2.4.2 Tensor Treatment ... 20
2.4.3 Additional Piezoelectric Coefficients ... 21

2.5 Domain and Lattice Contributions to Piezoelectric Properties in PZT ... 22
2.5.1 Lattice Contributions ... 22
2.5.2 Domain Contributions ... 23

2.6 Film Considerations ... 27
2.6.1 The Effective Transverse Piezoelectric Coefficient $e_{31,f}$ ... 30
2.6.2 The Effective Electrostrictive Coefficient Q_f ... 32

2.7 Temperature Dependence of Piezoelectric Properties of PZT Ceramics ... 35
2.7.1 Bulk Ceramics ... 35
2.7.2 Elastic Moduli ... 38

2.8 Compositional Dependence of Piezoelectric Properties of PZT ... 40
2.8.1 Bulk Ceramics ... 40
2.8.2 Films ... 40
2.8.3 Elastic Moduli ... 45

Chapter 3 : Experimental Procedure 46
3.1 Introduction 46
3.2 Lead Zirconate Titanate Film Preparation 46
3.2.1 Solution Preparation 46
3.2.2 Spin Coating 48
3.2.3 Edge Bead Removal 49
3.3 Structural Characterization 49
3.3.1 X-Ray Diffraction (XRD) 50
3.3.2 Scanning Electron Microscopy (SEM) 50
3.3.3 Surface Profilometry 50
3.4 High and Low Field Electrical Characterization 51
3.4.1 Electrical Contacts 51
3.4.2 PZT Film Patterning 51
3.4.3 Electrode Probing 52
3.4.4 Low Field Characterization 53
3.4.5 High Field Characterization 54
3.4.6 Temperature Dependent Characterization 54
3.5 MEMS Accelerometers 54
3.5.1 Design 55
3.5.2 Fabrication 57
3.5.3 Testing 59
3.5.3.1 Frequency Response Measurement 59
3.5.3.2 Impedance Resonance Measurement 60
3.6 Modified Wafer Flexure Technique for Measurement of the Effective Transverse Piezoelectric Coefficient $e_{31,f}$ and its Variation with Temperature 61
3.6.1 Wafer Flexure Technique 61
3.6.1.1 Principle of Operation 61
3.6.1.2 Theoretical Calculations of Film Strain 63
3.6.1.3 Uniform Pressure Rig 64
3.6.1.4 Peripheral Electronics 65
3.6.1.5 Charge Amplifier 65
3.6.2 Temperature Control Modifications 66
3.6.2.1 High Temperature Modification 66
3.6.2.2 Low Temperature Modification 68
3.6.2.3 Wafer Clamping Modification 69
3.6.2.4 Strain Measurement 71
3.6.2.5 Wafer Preparation 73
Chapter 4 : Results and Discussion 75
4.1 Introduction 75

4.2 Structural Characterization 75
4.2.1 X-Ray Diffraction Analysis 75
4.2.2 Atomic Force Microscopy Analysis 76
4.2.3 Scanning Electron Microscopy Analysis 77
4.2.4 Surface Profilometry 77

4.3 High and Low Field Electrical Characterization 78
4.3.1 Low Field Characterization 78
4.3.2 High Field Characterization 79
4.3.3 Temperature Dependent Characterization 81
4.3.3.1 Low Field Results 82
4.3.3.1.1 Curie Temperature Determination 82
4.3.3.1.2 Near Room Temperature Characterization 84
4.3.3.2 High Field Results 87

4.4 Piezoelectric Characterization 92
4.4.1 Room Temperature $e_{31,f}$ Characterization 93
4.4.2 Temperature Dependent Piezoelectric Characterization 94
4.4.2.1 Electrode-to-Electrode Uniformity 95
4.4.2.2 Wafer-to-Wafer Uniformity 96
4.4.2.3 Temperature Dependence of $e_{31,f}$ 96

4.5 Factors Affecting Electromechanical Properties of PZT Films During Temperature Cycling Between -55 and 85°C 100
4.5.1 Intrinsic Contributions to Piezoelectricity 101
4.5.2 Film Elastic Properties 101
4.5.3 Substrate Elastic Properties 102
4.5.4 Residual Stress State 102
4.5.5 Biaxial Stress Measurements 105

4.6 MEMS Accelerometers 108
4.6.1 Frequency Response Results 108
4.6.2 Impedance Resonance Results 110
4.6.3 Temperature Considerations 111

Chapter 5 : Conclusions and Future Work 113

5.1 Conclusions 113
5.1.1 The Modified Wafer Flexure Technique for Temperature Dependent Measurement of the Effective Transverse Piezoelectric Coefficient $e_{31,f}$ of Films 113
5.1.2 Temperature Dependent Characterization of the Piezoelectric Behavior of PZT Films on Pt-coated Silicon Substrates Between -55 and 85°C 114
5.1.3 Piezoelectric MEMS Accelerometers Involving PZT Films 116

5.2 Recommendations for Future Work 117
5.2.1 Investigation of the Stress Dependence of Non-180° Domain Wall Mobility 117
5.2.2 Introduction of Porosity in Films as a Means of Enhancing Figures of Merit for Specific Applications 120
5.2.3 Doping to Modify Dielectric and Piezoelectric Responses in Thick Ferroelectric Films 121

References 123

List of Figures

Figure 2.1 Top view of PZT thin film-based piezoelectric cantilever microvalve.[4] 4

Figure 2.2 Top view of piezoelectric micropump with both input and output ports.[4] 5

Figure 2.3 Ultrasonic elastic fin micromotor.[5] 5

Figure 2.4 Cross-sectional schematic view of a PI-FET accelerometer developed by Chen *et al.*[13] 8

Figure 2.5 Cross-sectional schematic view of thin-film piezoelectric accelerometer designed by Nemirovsky *et al.*[14] The PZT pads are poled perpendicular to the substrate plane. 9

Figure 2.6 Bulk micromachined ZnO-based piezoelectric accelerometers fabricated by de Reus *et al.*[15] (a) and (b) show top views of electrode pairing configurations A and B, respectively, while corresponding cross-sectional views are shown in (c) and (d). 10

Figure 2.7 Schematic cross-sections and SEM micrographs of ZnO-based surface micromachined piezoelectric accelerometers (PiXLs) presented by DeVoe *et al.*[16] The cantilevers shown in (a) were fabricated using a sacrificial oxide process while the PiXL shown in (b) was fabricated through a sacrificial silicon process. 10

Figure 2.8 Top view schematic of thick film PZT/micromachined silicon accelerometer reported by Beeby *et al.*[17] The dimensions of the inertial mass, beam, PZT, and top electrode were 2 mm × 2 mm, 975 μm × 750 μm, 900 μm × 660 μm, and 800 μm × 420 μm, respectively. 11

Figure 2.9 Polarization–electric field hysteresis loop characteristic of ferroelectric materials. The saturation polarization (P_{sat}), remanent polarization (P_r), and coercive field (E_c) are shown.[21] 14

Figure 2.10 Phase diagram for the $PbZrO_3$–$PbTiO_3$ solid solution system. P_C is the cubic paraelectric phase. F_R, F_T, and F_M are the rhombohedral, tetragonal, and monoclinic ferroelectric phases, respectively. Data of Jaffe *et al.*[20] are plotted as open circles. Recent results of synchrotron x-ray powder diffraction measurements by Noheda *et al.*[22] are plotted as closed squares. The morphotropic phase boundary (MPB) is indicated. 15

Figure 2.11 Schematic representation of the cubic (m3m) prototype structure of perovskite ABO_3 compounds. The oxygen octahedron is highlighted. In $Pb(Zr,Ti)O_3$, $A = Pb^{2+}$, $B = Zr^{4+}$ or Ti^{4+}, and $O = O^{2-}$. 16

Figure 2.12 Unit cell distortions that result from the spontaneous polarization (P_s) in $BaTiO_3$. Dotted lines designate (a) the prototypic cubic (m3m) phase that exists above T_c. P_s can be oriented along (b) the 6 equivalent <001> directions in the tetragonal phase, (c) the 12 equivalent <011> directions in the orthorhombic phase and (d) the 8 equivalent <111> directions in the rhombohedral phase. All directions are in reference to the cubic prototype.[23] 17

Figure 2.13 Compositional dependence of relative permittivity (ε_r) and piezoelectric coupling coefficient (k) the $PbZrO_3$–$PbTiO_3$ solid solution system. Note the peak in properties at the MPB.[21] 18

Figure 2.14 Phenomenologically-derived values of intrinsic relative permittivity (ε_{ij}) of PZT as a function of temperature for tetragonal (PZT 40/60), near MPB (PZT 50/50), and rhombohedral (PZT 60/40) compositions. The ε_{33} coefficient is plotted for PZT 40/60 and 50/50 while ε_{11} and ε_{12} are shown for PZT 60/40. Equations taken from Haun.[26] 24

Figure 2.15 Phenomenologically-derived values of spontaneous polarization (P_S) of PZT as a function of temperature for tetragonal (PZT 40/60), near MPB (PZT 50/50), and rhombohedral (PZT 60/40) compositions. Equations taken from Haun.[26] 24

Figure 2.16 Phenomenologically-derived values of the intrinsic piezoelectric d_{31} coefficient of PZT as a function of temperature for tetragonal (PZT 40/60), near MPB (PZT 50/50), and rhombohedral (PZT 60/40) compositions. Equations taken from Haun.[26] 25

Figure 2.17 Temperature dependence of relative permittivity (ε_{33}) and transverse piezoelectric coefficient (d_{31}) measured between 4.2 and 300 K for Navy-type 1, 2, 3, and 4 PZT ceramics (from Zhang[27]). All have base PZT compositions near the MPB. Types 2 and 4 are doped with softeners Nb_2O_5 and Sb_2O_3, respectively. Types 1 and 3 are doped with hardeners NiO and Fe_2O_3, respectively. 26

Figure 2.18 Plots of normalized (a) capacitance and (b) d_{33} piezoelectric coefficient as a function of applied stress for a poled 1 μm <111>-oriented PZT 52/48 film with an average grain size ~100 nm (from Xu *et al.*[29]). To illustrate extrinsic contributions to piezoelectric properties in the bulk, a PZT-5A bulk ceramic is also shown in (b). 28

Figure 2.19 Plots of normalized (a) dielectric constant and (b) d_{33} piezoelectric coefficient as a function of AC field at 1 kHz. All films were poled at 250 kV/cm at room temperature and randomly oriented with an average grain size ~100 nm (from Xu *et al.*[29]). 29

Figure 2.20 Temperature dependence of dielectric constant (ε_{33}) of several chemical solution deposited PZT 52/48 films measured at 1 kHz between 4.2 and 298 K. Films 1 and 3 are <100>-oriented while 2, 4, 5, and 6 are <111>-oriented (from Xu *et al.*[29]). 30

Figure 2.21 Effective electrostriction coefficient of a <111>-oriented, 0.3 μm-thick PZT 45/55 film prepared by a modified sol-gel process plotted versus electric field.[31] Values were extrapolated from measured dielectric, ferroelectric, and piezoelectric data through Equation 2.17. 33

Figure 2.22 Measured values of Q_f for differently textured PZT thin films (from Kholkin *et al.*[31]) plotted as a function of composition. As comparison, thermodynamic calculations[26] of upper and lower limits of Q_{11} are shown for bulk PZT........ 34

Figure 2.23 Experimental fit of Curie temperature (T_c) as a function of composition across the $Pb(Zr,Ti)O_3$ solid solution system.[32] PZT 60/40, 52/48, and 40/60 compositions are highlighted. 36

Figure 2.24 Temperature dependence of the transverse piezoelectric coefficient d_{31} of PZT-5H ceramic samples measured under large electric fields (up to 5 kV/cm).[33].. 37

Figure 2.25 Low temperature elastic compliance coefficient (s_{11}^E) plotted as a function of temperature for several tetragonal and rhombohedral PZT compositions.[34] 39

Figure 2.26 Intrinsic contributions to s_{11} derived from measured data for undoped $Pb(Zr_xTi_{1-x})O_3$ ceramics (from Herbiet *et al.*[36]). 39

Figure 2.27 Composition dependence of bulk ceramic piezoelectric d coefficients around the MPB[20]. Maximum values occur at 52 mol% $PbZrO_3$. 40

Figure 2.28 (a) Dielectric permittivity, (b) remanent polarization and coercive field, and (c) effective d_{33} as a function of Zr/Ti ratio in 1 μm sol-gel PZT films.[38] Maximum values of ε_{33}, P_r, and $d_{33,f}$ are located at the MPB PZT 52/48 composition and correspond to bulk maxima. Bulk data were taken from Berlincourt *et al.*[39] 41

Figure 2.29 Variation of effective transverse piezoelectric coefficient $e_{31,f}$ with composition for several PZT thin films[30]. The highest $e_{31,f}$ values were observed on the tetragonal side of the MPB (PZT 45/55). 43

Figure 2.30 As-grown (virgin) and maximum (poled) values of $d_{33,f}$ in reactively sputtered PZT thin films deposited on Pt<111> and RuO_2-coated substrates.[41] Calculated results represent bulk ceramic data that is corrected for the substrate clamping condition. 44

Figure 2.31 (a) Elastic compliance coefficient (s_{11}^E) and (b) Poisson's ratio (ν) at 4.2 and 300 K plotted as a function of PZT composition.[34] 45

Figure 3.1 Chemical solution spin-on process flow for PZT films prepared in this investigation. 47

Figure 3.2 Pt electrodes were contacted in two ways: (a) probe tip pressure contact and (b) alligator clip contact to epoxied wire leads. 53

Figure 3.3 Cross-sectional view of circular diaphragm sensing structure of MEMS accelerometer (courtesy of Wilcoxon Research, Inc.). 56

Figure 3.4 Radial and tangential stresses as a function of radial position along the annular diaphragm. σ_r and σ_θ correspond to the solid and dashed lines, respectively. 57

Figure 3.5 Fabrication process flow for MEMS accelerometer structure.[19] The two step DRIE sequence shown was used for through-etched parts. In the annular-type device, the entire backside of the structure was protected in step (7), and the annulus was exposed and etched during step (8). 58

Figure 3.6 Frequency response measurement system. 60

Figure 3.7 Room temperature wafer flexure measurement setup. 62

Figure 3.8 Simplified circuit diagram of charge amplifier 66

Figure 3.9 Measured temperature profile across a 3" wafer with the aluminum housing heated to 125°C. The maximum temperature used in subsequent experiments was 85°C. 67
Figure 3.10 Low temperature wafer flexure measurement setup. 68
Figure 3.11 Uniformly loaded circular plate with (a) clamped edge and (b) simply supported edge. Boundary conditions are given above. r is radial position (m), a is support radius (m), p is pressure (N/m^2), w is deflection (m), and M_r is the radial bending moment (N·m). 70
Figure 3.12 Stress variation with radial position for a uniformly loaded circular plate with clamped edge and simply supported edge. The zero stress baseline is shown for each case. The wafer clamping modification results in a condition intermediate between these extremes. 71
Figure 3.13 Schematic diagram of quarter bridge circuit used in strain measurements. 72
Figure 3.14 3" PZT-coated wafer preparation for modified wafer flexure measurement of $e_{31,f}$ with temperature (not to scale). 73
Figure 4.1 X-ray diffraction patterns of chemical solution deposited PZT films characterized in this study. 76
Figure 4.2 AFM image of the surface of a 2 μm PZT 40/60 film. Average grain size was 150–200 nm. 77
Figure 4.3 SEM micrographs of (a) cross-section of a 6 μm PZT 60/40 film and (b) near surface morphology of a 4 μm PZT 52/48 film. 78
Figure 4.4 Plots of room temperature (a) relative permittivity and (b) loss tangent as a function of Zr/Ti ratio for 2 μm, 4 μm, and 6 μm PZT films. Error bars are nested within symbols in (a). 80
Figure 4.5 Plots of room temperature (a) remanent polarization and (b) coercive field as a function of Zr/Ti ratio for 2, 4, and 6 μm PZT films. 81
Figure 4.6 Polarization-electric field hysteresis loops for 6 μm PZT films measured at room temperature. 82

Figure 4.7 Plot of relative permittivity (ε_{33}) of 2 μm PZT films with different Zr/Ti ratios as a function of temperature used in determining Curie temperatures. Measurements were made at 20 kHz and ~0.15 kV/cm. 83

Figure 4.8 Relative permittivity and dielectric loss tangent of Pt/PZT/Pt stack plotted as a function of temperature for (a) 2 μm, (b) 4 μm, and (c) 6 μm films measured at 1 kHz. 85

Figure 4.9 Relative permittivity of Pt/PZT/Pt stack plotted as a function of temperature for (a) PZT 40/60, (b) 52/48, and (c) 60/40 films measured at 1 kHz. 86

Figure 4.10 Temperature dependence of remanent polarization and coercive field for (a) 2 μm, (b) 4 μm, and (c) 6 μm PZT films. In E_c plots, error bars are nested within symbols. 89

Figure 4.11 Temperature dependence of remanent polarization and coercive field for (a) PZT 40/60, (b) 52/48, and (c) 60/40 films. In E_c plots, error bars are nested within symbols. 90

Figure 4.12 Polarization-electric field hysteresis loops as a function of temperature for the 2 μm PZT 40/60 film. 91

Figure 4.13 Room temperature transverse piezoelectric coefficient $e_{31,f}$ as a function of Zr/Ti ratio for 2 μm, 4 μm, and 6 μm PZT films. 93

Figure 4.14 Plot of normalized $|e_{31,f}|$ as a function of temperature for a 2 μm PZT 60/40 film. Data were collected from three distinct electrodes (denoted 1, 2, and 3) during three separate experiments. 95

Figure 4.15 Temperature dependence of normalized $|e_{31,f}|$ for (a) 2 μm, (b) 4 μm, and (c) 6 μm PZT films measured using the modified wafer flexure technique. 97

Figure 4.16 Temperature dependence of normalized $|e_{31,f}|$ for (a) PZT 40/60, (b) 52/48, and (c) 60/40 films measured using the modified wafer flexure technique. 98

Figure 4.17 Chemical solution deposited PZT 53/47 thin film stress as a function of temperature on cooling from T_c for a film deposited on platinum-coated (100) silicon.[55] 104

Figure 4.18 Unit cell distortions along *a*- and *c*-axes of PZT 32/68 as a function of temperature measured by high temperature powder x-ray diffraction.[26] 104

Figure 4.19 Sample preparation for room temperature measurement of $e_{31,f}$ as a function of external biaxial stress (schematic not to scale). 106

Figure 4.20 Normalized $e_{31,f}$ coefficient of a 2 μm PZT 52/48 film measured at room temperature as a function of external strain. The stress was calculated assuming E = 101 GPa and ν = 0.3 for the PZT film. 108

Figure 4.21 Photographs of (a) frontside and (b) backside processed annular MEMS accelerometers (courtesy of Wilcoxon Research, Inc.).[19] Device packaging is also included in (b). 109

Figure 4.22 Measured frequency response of an annular diaphragm-type MEMS accelerometer. The resonant frequency was 22.1 kHz and the sensitivity was 0.47 pC/g. 109

Figure 4.23 Sensitivity plotted as a function of resonance frequency for several types of MEMS accelerometers with varying support beam thicknesses.[19] 110

Figure 4.24 Impedance characteristics of a cantilever-type MEMS accelerometer showing fundamental resonance at 8.2 kHz. Z and θ are impedance and phase angle, respectively. 111

Figure 5.1 PZT film porosity study. The observed layer thickness increase shown in (a) is attributed to an increasing pore fraction. Normalized permittivity ε_{33} and piezoelectric coefficient $e_{31,f}$ plotted in (b) and (c). 122

List of Tables

Table 2.1 Several MEMS application areas in which ferroelectric films are competitive candidates. Key materials, phenomena, and figures of merit are given for each category.[6,7] 6

Table 2.2 Effective transverse piezoelectric coefficients of various PZT films[30]. The bulk e_{31} coefficient has been included for comparison[20] 31

Table 2.3 Dielectric permittivity, remanent polarization, and effective d_{33} of several 1 μm sol-gel deposited PZT films with different preferred orientations and Zr/Ti ratios near the MPB.[28] 42

Table 3.1 Two-step wet etching process for thick PZT films used to expose the bottom electrode. 52

Table 3.2 Elastic constants of Si used in this investigation. The Si wafer was treated as an isotropic plate.[49] 64

Table 4.1 Measured thicknesses of ten PZT films characterized in this study. 78

Table 4.2 Measured Curie temperatures of 2 μm-thick PZT films and bulk PZTs. 84

Table 4.3 Percent increase in permittivity from –55 to 85°C based on second order polynomial regression fits to measured data for PZT films. 87

Table 4.4 Percent decrease in remanent polarization from -55°C to 85°C based on linear regression fits to measured data for PZT films. 91

Table 4.5 Percent decrease in coercive field from -55°C to 85°C based on linear regression fits to measured data for PZT films. 91

Table 4.6 Normalized percent changes in P_s predicted by phenomenology on heating from -55°C to 85°C based on PZT Zr/Ti ratio. Measured P_r values are shown for comparison. 92

Table 4.7 Percent increase in $|e_{31,f}|$ from –55°C to 85°C based on second order polynomial regression fits to measured data for PZT films. 99

Table 4.8 Intrinsic d_{31} values of several PZT compositions (from Figure 2.16). The percent increase from -55°C to 85°C is also given. 101

Table 4.9 Normalized sensitivity and temperature dependence of sensitivity of a hypothetical MEMS sensor involving a piezoelectric PZT film element. Values are based on $e_{31,f}$ vs. temperature data obtained in this study. 112

Table 5.1 Approximate magnitudes of film stress developed on cooling as a result of the thermal mismatch between PZT film and substrate. Calculations based on Equation 4.1 using substrate thermal expansion coefficients (from Bever[58]). Stress is given in three columns: 700°C–T_c is the stress developed on cooling from the crystallization temperature to T_c, T_c–25°C is that developed on cooling from T_c to room temperature, and 700–25°C is the total residual stress at room temperature. 119

Acknowledgements

My journey to completing the M.S. was not made alone and I would like to thank a number of people for their help along the way. First, I would like to express gratitude to my advisor, Dr. Susan Trolier-McKinstry, for her guidance and trust throughout my tenure at Penn State. Her advising style and high expectations have greatly assisted my personal and professional growth. Second, I want to thank Li-Peng Wang, who was chiefly responsible for MEMS device fabrication and with whom I shared many technical discussions and good times. I would also like to acknowledge members of our research group, both past and present. Ron Polcawich, Wei Ren, and Fei Xu "showed me the ropes" when I began my research and have since moved on to bigger and better things. Later, discussions with experienced ferroelectricians including Eunki Hong, Qifa Zhou, Qingqi Zhang, and Takeshi Yoshimura furthered my development. Other group members, particularly Mike Biegalski, Lisa Friedman, and Ryan Thayer, made my time spent at the lab an enjoyable experience.

In addition, I would like to show appreciation to the entire MRL support staff, whose tireless efforts in assisting students are vital to the success of the lab. In particular, I would like to thank Paul Moses for the useful advice and guidance he provided. Jeff Long, Chris Jabco, and Gaylord Shawver were also helpful and always went the extra mile to keep my research running smoothly.

This work was supported through a NIST Advanced Technology Program under contract WR-ATP-001. Our collaboration with Wilcoxon Research, Inc. on the MEMS accelerometer is gratefully recognized.

Last, but certainly not least, I would like to make special acknowledgement to my family for their love and support. This thesis is dedicated to my Dad.

Chapter 1 : Introduction

Microelectromechanical systems (MEMS) technology unites conventional silicon-based integrated circuit (IC) electronics with micro-scale sensors and actuators.[1] Many devices in this growing field rely on thin film piezoelectrics to produce the desired electromechanical response. Of these, lead zirconate titanate ($PbZr_xTi_{1-x}O_3$), or PZT, films are of great interest due to their large piezoelectric coefficients, which are an order of magnitude larger than those of more widely-used film materials such as zinc oxide (ZnO) and aluminum nitride (AlN).[2] However, PZT belongs to a class of materials known as ferroelectrics whose behavior is more complex than simple piezoelectrics, and which often require higher processing temperatures. As a result, non-ferroelectric ZnO and AlN films continue to be used in many piezoelectric MEMS applications.

Clamping to a rigid substrate changes the piezoelectric properties of thin films as compared to bulk ferroelectrics. Suppressed piezoelectric responses are a typical consequence and several causes have been suggested. The constraints imposed by the substrate can lead to (1) reduced extrinsic contributions to the piezoelectric response, (2) considerable residual stresses on cooling from the film's crystallization temperature, and (3) decreased film strain due to the requirement that the massive substrate be moved along with it.[2]

To date, little data is available that describes the way in which substrate clamping modifies the temperature dependence of the electromechanical response of PZT. Since piezoelectric MEMS devices are designed to operate over a finite temperature range, it is essential that any changes in the piezoelectric properties of PZT films be characterized

over this range. With this knowledge, electronic compensation can be used to account for variations in piezoelectric coefficients with temperature.

A major goal of this thesis was to determine the effective transverse piezoelectric coefficients $e_{31,f}$ of PZT films as a function of temperature with the aim of gaining a better understanding of the influence of the substrate on the temperature dependent piezoelectric responses. To accomplish this objective, the wafer flexure technique[3] was modified to enable temperature variable characterization. An attempt was made to identify the mechanisms responsible for the observed piezoelectric temperature dependence in PZT films. The succeeding chapters provide relevant background information on both MEMS technology and lead zirconate titanate films, describe the experimental methods by which films were prepared and characterized, and present and discuss measured results. In addition, details of the design, fabrication, and characterization of PZT film-based MEMS accelerometers are included. Finally, conclusions are drawn and suggestions for future work are offered.

Chapter 2 : Literature Review

2.1 Introduction

The objectives of this undertaking were to fabricate MEMS accelerometers involving PZT films, characterize the temperature dependent transverse piezoelectric behavior of the films, and gain insight into the mechanisms governing this behavior. To this end, this chapter provides a short review of MEMS devices, with a focus on microaccelerometers, and background information related to PZT and the unique origin of its piezoelectric properties.

2.2 Microelectromechanical Systems (MEMS) Devices

With the constant push for device miniaturization, microelectromechanical systems (MEMS) have become an active research topic in recent years. Commercial devices have been designed and fabricated for use in biomedical, manufacturing, information processing, and automotive industries, among others.[1]

Some MEMS devices incorporate a piezoelectric material, typically in thick or thin film form, to serve a sensing or actuating function. When used in MEMS actuators, the piezoelectric film produces motion when excited by an electrical signal. As a sensor, it is used to generate an electrical signal in response to a mechanical stress. Several examples of piezoelectric MEMS devices are shown in Figures 2.1 through 2.3.

A piezoelectric microvalve is presented in Figure 2.1. Here, a piezoelectric film capacitor is fabricated atop a non-piezoelectric cantilever support structure (silicon). By applying a voltage across the film, the free tip of the cantilever can be controllably

displaced. For a PZT thin film-based microvalve, a vertical tip displacement of 2.1 μm in a 100 μm × 400 μm × 1.5 μm cantilever has been achieved with an applied voltage of 25 V.[4]

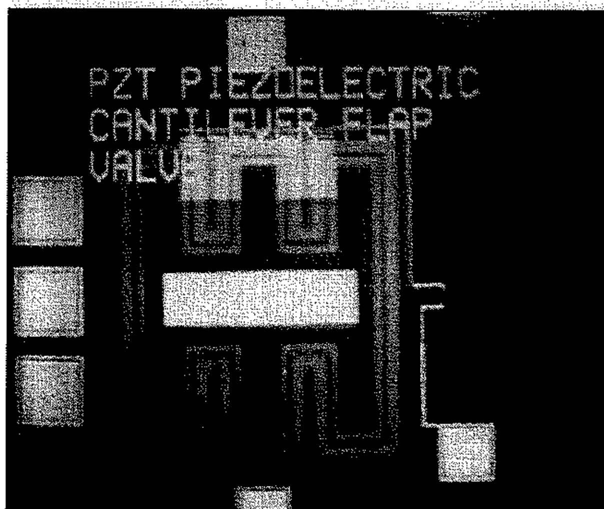

Figure 2.1 Top view of PZT thin film-based piezoelectric cantilever microvalve.[4]

Figure 2.2 shows a MEMS micropump capable of transporting fluid through cavity reservoirs. Each annular membrane is overlayed with a piezoelectric film capacitor and pumping is achieved through the sequential actuation of these deformable membranes.

An ultrasonic elastic fin micromotor is illustrated in Figure 2.3. A detailed description of the operating principles of this device can be found elsewhere.[5] A piezoelectric film actuates the membrane of the stator and motion of the membrane structure toward and away from the fins is used to produce the torque in the rotor.

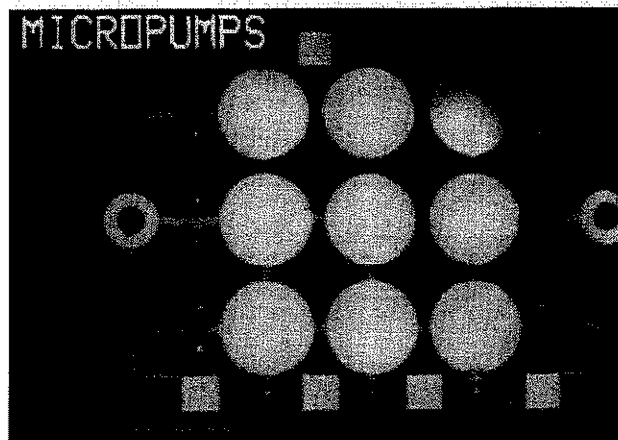

Figure 2.2 Top view of piezoelectric micropump with both input and output ports.[4]

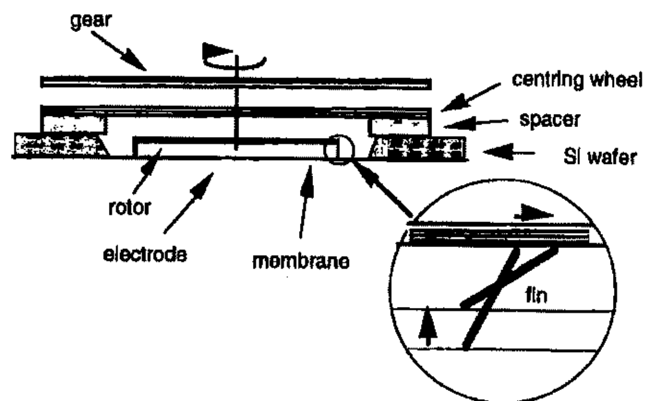

Figure 2.3 Ultrasonic elastic fin micromotor.[5]

2.2.1 Figures of Merit for MEMS Applications

A figure of merit based on a material property or combination of properties can be established to compare different materials for a specific application. To point out some of these relevant properties, Table 2.1 presents figures of merit in several MEMS application areas. Candidate film materials and device operating phenomena are included as well.

Table 2.1 Several MEMS application areas in which ferroelectric films are competitive candidates. Key materials, phenomena, and figures of merit are given for each category.[6,7] Symbols are defined below*.

Application	*Film Materials*	*Phenomenon*	*Figure(s) of Merit*
Microsensors	$Pb(Zr,Ti)O_3$ ZnO AlN	Piezoelectric	*current mode*: $e_{31,f}$, $d_{33,f}$ *voltage mode*: $e_{31,f} / \varepsilon_{33,f}$, $d_{33,f} / \varepsilon_{33,f}$
Microactuators	$Pb(Zr,Ti)O_3$ ZnO AlN	Piezoelectric	$e_{31,f}$, $d_{33,f}$
Resonant Devices	$Pb(Zr,Ti)O_3$ ZnO AlN	Piezoelectric	k_f , Z
Infrared Detectors	$(Pb,La)(Zr,Ti)O_3$ $Pb(Ca,Ti)O_3$ $(Sr,Ba)Nb_2O_6$	Pyroelectric	$p / \varepsilon_{33,f}$, $p / \sqrt{\varepsilon_{33,f} \tan\delta}$
Electro-Optic Devices	$LiNbO_3$ $(Pb,La)(Zr,Ti)O_3$ $K(Ta,Nb)O_3$	Electro-Optic	r , R , n , *transmission loss*

*$e_{31,f}$: transverse piezoelectric coefficient (C/m^2)
$d_{33,f}$: longitudinal piezoelectric coefficient (pC/N)
$\varepsilon_{33,f}$: permittivity
k_f: electromechanical coupling coefficient
Z: acoustic impedance ($kg/s \cdot m^2$)
p: pyroelectric coefficient ($C/m^2 \cdot K$)
$\tan\delta$: dielectric loss tangent
r: primary electrooptic coefficient (m/V)
R: secondary electrooptic coefficient (m^2/V^2)
n: index of refraction

As far as piezoelectric MEMS are concerned, piezoelectric coefficients and permittivities are found to be important design parameters. These will be described in detail later in this thesis.

2.2.2 MEMS Accelerometers

In the above discussion, only MEMS actuator devices were presented. Accelerometers are another important MEMS application and these fall into the class of sensors. The popularity of these devices in recent years has been due primarily to their wide range of automotive uses in safety, vehicle stability and electronic suspension systems. In 1997, they were second only to pressure sensors for volume sales of silicon-based sensors. However, with the prospect of being able to manufacture these miniature, high-performance sensors at lower costs, the market is continuously expanding with applications in consumer products, the biomedical field, industrial monitoring and the military.[8]

Of the various types of accelerometers, including piezoresistive[9] and capacitive,[10] piezoelectric accelerometers offer advantages of a high Q (≥ 80), high output impedance, low damping, and a relatively large temperature range of operation.[11] ZnO, AlN and lead zirconate titanate (PZT) films have been employed in piezoelectric microaccelerometers. Of these candidates, PZT films exhibit the highest piezoelectric coefficients and can potentially offer very high sensitivities. Thin film piezoelectric coefficients of PZT are an order of magnitude larger than those of ZnO and AlN.[12]

Numerous reports of MEMS piezoelectric accelerometers are available in the literature,[13-17] mostly involving ZnO films. Figures 2.4 through 2.8 present several of these MEMS designs. The measured device characteristics are given when available.

Figure 2.4 shows one of the earliest reported MEMS accelerometers. This piezoelectric-film field-effect transistor (PI-FET) accelerometer was developed by Chen *et al.*[13] The device incorporated a thick silicon proof mass and a 2 μm sputtered ZnO

film served as the piezoelectric. A nearly flat frequency response of 5 mV/g was reported from near DC to 2.5 kHz and the mechanical resonance occurred at 8.4 kHz.

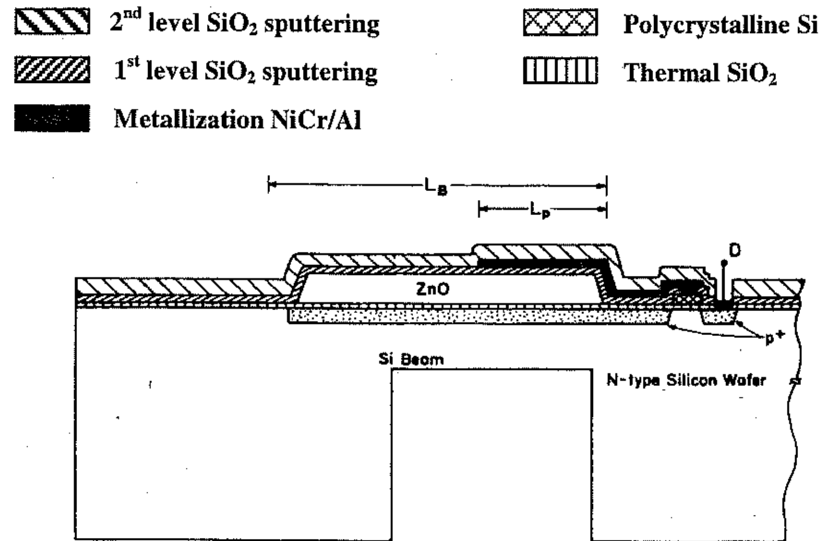

Figure 2.4 Cross-sectional schematic view of a PI-FET accelerometer developed by Chen *et al.*[13]

A novel design for a thin-film PZT-based accelerometer is shown in Figure 2.5.[14] In response to accelerations perpendicular to the substrate plane, a seismic mass exerts a force across each of an array of PZT thin film pads and voltage is developed through the direct piezoelectric effect. Damping is achieved through a viscous polymer that fills voids between the pads. The design is unique in that it exploits the d_{33}-mode piezoelectric response of the PZT film, where the primary stress in the film is directed along its polarization direction. This d_{33}-mode response is typically about two times greater than the d_{31}-mode response used in most MEMS accelerometers. Authors reported a theoretical sensitivity of 320 mV/g, a mechanical resonance at 225 kHz, and lower and upper cut-off frequencies of 1 Hz and 200 kHz, respectively. However, this device has not been fabricated to date.

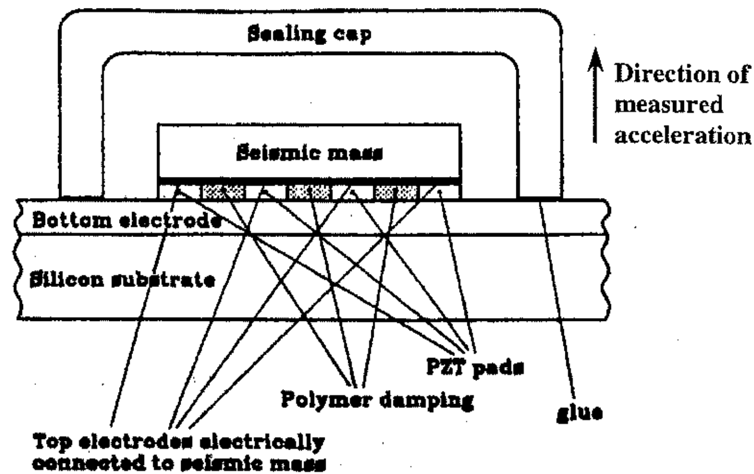

Figure 2.5 Cross-sectional schematic view of thin-film piezoelectric accelerometer designed by Nemirovsky *et al.*[14] The PZT pads are poled perpendicular to the substrate plane.

Figure 2.6 shows a bulk micromachined piezoelectric accelerometers based on ZnO that was fabricated by de Reus *et al.*[15] Structures were capable of sensing accelerations in either vertical or horizontal directions, depending on the pairing of inner and outer electrodes. Configuration A was used to sense acceleration in the vertical direction where deflection in the two support beams is symmetrical. For asymmetric bending, which results from horizontal acceleration, configuration B was used. The vertical sensitivity was reported as 0.1 pC/g with a resonance frequency above 4.5 kHz. The horizontal sensitivity was found to be two orders of magnitude lower.

In 2001, Devoe *et al.*[16] presented ZnO-based surface micromachined piezoelectric accelerometers (PiXLs), as shown in Figure 2.7. For the simple cantilever device, a sensitivity of 0.95 fC/g and a resonance frequency of 3.3 kHz were reported. Higher sensitivities were measured in the sacrificial Si processed PiXL: 13.3 fC/g and 44.7 fC/g at resonance frequencies of 2.23 kHz and 1.02 kHz, respectively.

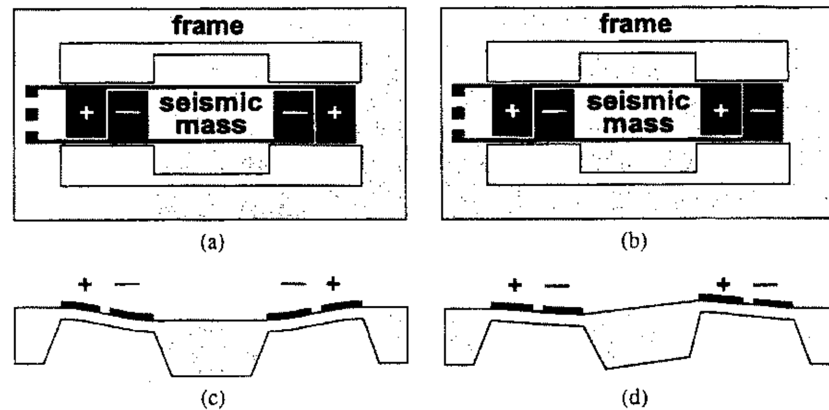

Figure 2.6 Bulk micromachined ZnO-based piezoelectric accelerometers fabricated by de Reus *et al.*[15] (a) and (b) show top views of electrode pairing configurations A and B, respectively, while corresponding cross-sectional views are shown in (c) and (d).

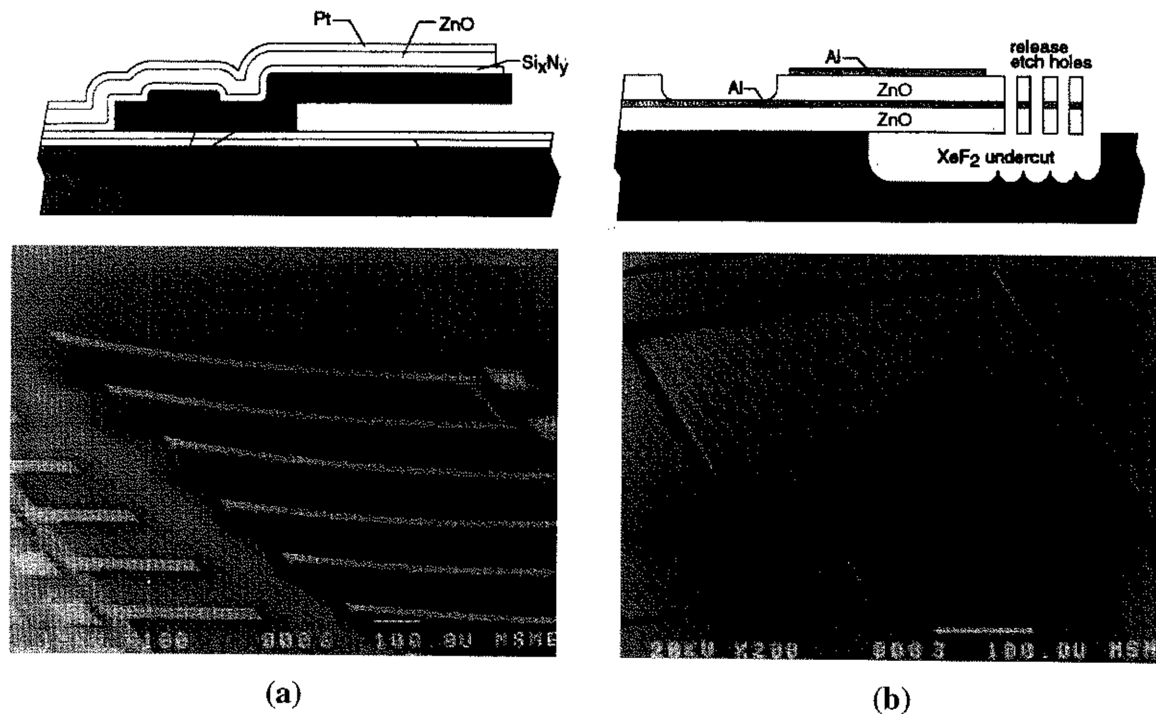

Figure 2.7 Schematic cross-sections and SEM micrographs of ZnO-based surface micromachined piezoelectric accelerometers (PiXLs) presented by DeVoe *et al.*[16] The cantilevers shown in (a) were fabricated using a sacrificial oxide process while the PiXL shown in (b) was fabricated through a sacrificial silicon process.

Beeby *et al.* at the University of Southampton (UK) designed and fabricated a bulk micromachined silicon accelerometer that utilized thick screen-printed PZT films.[17]

A silicon inertial mass was suspended by four silicon support beams, each coated with a 60 μm PZT film (Figure 2.8). Authors measured a sensitivity of 16 pC/g in the z-direction. However, obvious design flaws and results that are not self-consistent place this large reported sensitivity under doubt. From the design standpoint, a blanket top electrode that spans the length of the beam is imprudent because stresses near the frame and inertial mass are of opposite sign; a situation that will result in substantial cancellation of charge output. Next, the reported mass and dimensions of the silicon inertial mass did not correlate. Authors reported dimensions of 4 $mm^2 \times 525$ μm and a 17 mg mass but these dimensions correspond to a mass of less than 5 mg for silicon's 2.3 g/cc density.[18] Furthermore, the voltage sensitivity (100 μV/g) was not consistent with the charge sensitivity (16 pC/g) for the reported sensor capacitance (360 pF).[19] Finally, low measured PZT thick film piezoelectric coefficients (d_{31} = -33 pC/g) and Young's moduli (Y = 20 GPa) make the 16 pC/g reported sensitivity even more suspect.

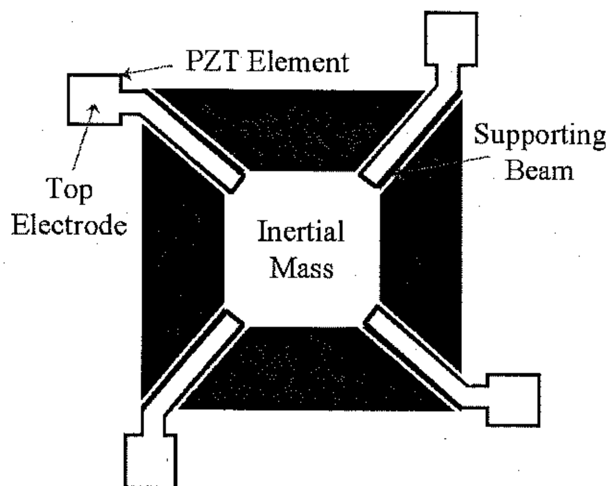

Figure 2.8 Top view schematic of thick film PZT/micromachined silicon accelerometer reported by Beeby *et al.*[17] The dimensions of the inertial mass, beam, PZT, and top electrode were 2 mm × 2 mm, 975 μm × 750 μm, 900 μm × 660 μm, and 800 μm × 420 μm, respectively.

In all of these designs, accelerometer sensitivity is dependent on the piezoelectric coefficients of the sensing film, and the magnitude of the stress that can be imparted on the film by the inertial mass. In order to obtain higher piezoelectric coefficients, there is renewed interest in ferroelectric thin film-based sensors.

2.3 Lead Zirconate Titanate

As a consequence of its superior dielectric and piezoelectric properties, lead zirconate titanate has gained widespread popularity since its discovery in the mid-1950s.[20] At low temperatures (below ≈300°C) and in compositions across most of the $PbZrO_3$–$PbTiO_3$ phase diagram, it is ferroelectric.

2.3.1 Ferroelectricity

2.3.1.1 Spontaneous Polarization

By definition, a ferroelectric material possesses a spontaneous polarization that can be reoriented between two or more crystallographically equivalent states by a realizable electric field. A spontaneous polarization is one that exists in the absence of an applied field. This phenomenon shares close analogy with ferromagnetism, in which spontaneous alignment of magnetic dipoles occurs within localized regions below a critical temperature. Much of the ferroelectric terminology is borrowed from that established in the field of ferromagnetism.[20]

As a ferroelectric is cooled below a certain critical temperature, known as the Curie temperature, T_c, relative atomic shifts cause a reorientable spontaneous dipole to develop within each unit cell. At T_c there is a transition from a high temperature

paraelectric phase to a low temperature ferroelectric phase. Domains develop, and within each domain, neighboring unit cells share the same polarization direction. The domain structure forms as the material responds to both electrostatic and mechanical stresses.[20]

In randomly-oriented polycrystalline ferroelectrics, the domain structure is randomized upon cooling through T_c and there is usually little or no measurable polarization at a macroscopic level. To use these materials as piezoelectrics or pyroelectrics, they must be poled. In poling, a DC electric field is used (frequently at elevated temperature) to reorient and align domains. When the field is removed, a certain fraction of domains will remain aligned in the field direction, giving rise to a net macroscopic polarization and the realization of piezoelectric and pyroelectric properties. Electrostatic and mechanical stresses, in addition to the presence of local internal fields (from defect dipoles, trapped charges, etc.) prevent complete alignment of domains upon removal of the field and are responsible for the domain structure.[21]

2.3.1.2 Polarization–Electric Field Hysteresis

The single most distinctive feature of a ferroelectric material is the polarization–electric field hysteresis loop (Figure 2.9), which shows how the magnitude and direction of the applied electric field affect the macroscopic polarization. Hysteresis behavior results from switching of the ferroelectric domains and exemplifies the reorientability of the spontaneous polarization.

Three important parameters are used to describe the polarization–electric field hysteresis loop of a ferroelectric and these are indicated in Figure 2.9. The saturation polarization, P_{sat}, is the linear extrapolation of the high field polarization to zero field and

represents the maximum degree of domain alignment possible at zero field. P_r is the remanent polarization, which is the net polarization retained upon removal of the field. The coercive field, E_c, is that required to return the net polarization to zero.

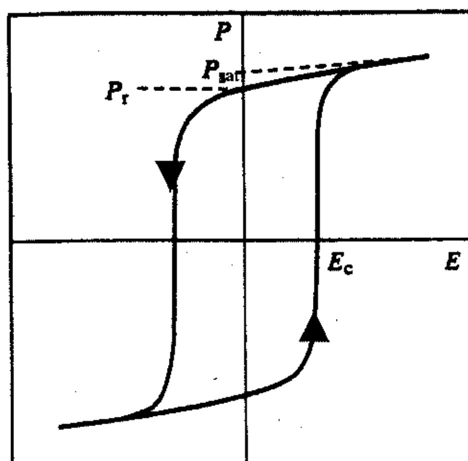

Figure 2.9 Polarization–electric field hysteresis loop characteristic of ferroelectric materials. The saturation polarization (P_{sat}), remanent polarization (P_r), and coercive field (E_c) are shown.[21]

2.3.1.3 Curie-Weiss Behavior

Ferroelectric materials commonly exhibit anomalously high dielectric permittivities.[20] In addition, in proper ferroelectrics, the dielectric constant shows a peak at the Curie temperature. Above T_c where the material is paraelectric, the Curie-Weiss Law (Equation 2.1) describes the temperature dependence of the permittivity.

$$\varepsilon_r - 1 = \frac{C}{T - T_o} \tag{2.1}$$

ε_r is the relative permittivity, C is the Curie constant (°C), T is temperature (°C), and T_o is the Curie-Weiss temperature (°C), not to be confused with the Curie temperature, T_c.

2.3.2 Characteristics of Lead Zirconate Titanate

2.3.2.1 Structural Features

The PZT phase diagram is shown in Figure 2.10. The cubic paraelectric phase is stable at high temperature and depending on the Zr/Ti ratio, there are transitions to either tetragonal or rhombohedral ferroelectric phases upon cooling through T_c. Recently, synchrotron x-ray powder diffraction analysis revealed a monoclinic phase between the well-known tetragonal and rhombohedral regimes.[22]

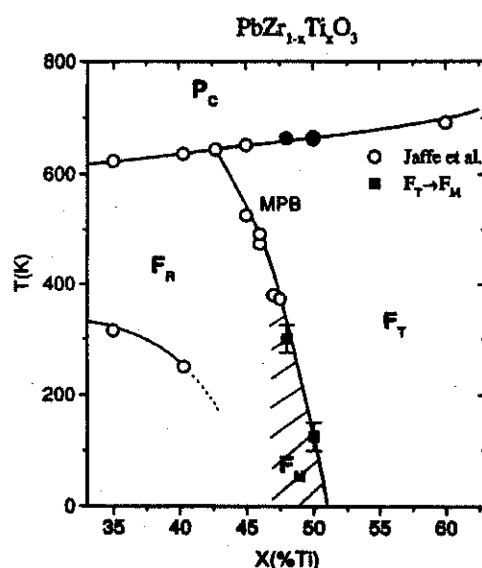

Figure 2.10 Phase diagram for the $PbZrO_3$–$PbTiO_3$ solid solution system. P_C is the cubic paraelectric phase. F_R, F_T, and F_M are the rhombohedral, tetragonal, and monoclinic ferroelectric phases, respectively. Data of Jaffe *et al.*[20] are plotted as open circles. Recent results of synchrotron x-ray powder diffraction measurements by Noheda *et al.*[22] are plotted as closed squares. The morphotropic phase boundary (MPB) is indicated.

The cubic paraelectric phase of PZT exhibits the perovskite crystal structure (Figure 2.11), which is the most important structure of inorganic ferroelectrics.[20] The ABO_3 structure is comprised of corner-linked oxygen octahedra with the smaller B-site

cations occupying sites within the octahedra and larger A-site cations occupying dodecahedral sites between octahedra.

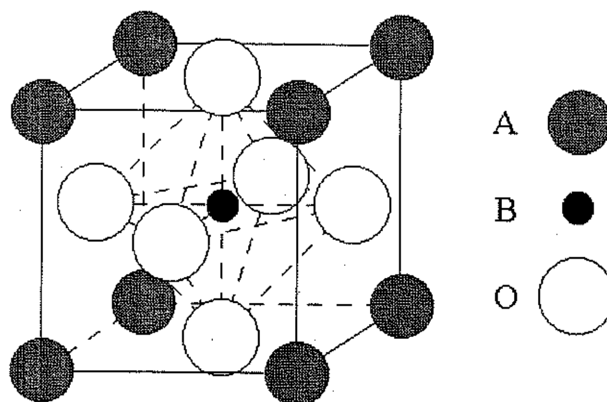

Figure 2.11 Schematic representation of the cubic (m3m) prototype structure of perovskite ABO_3 compounds. The oxygen octahedron is highlighted. In $Pb(Zr,Ti)O_3$, A = Pb^{2+}, B = Zr^{4+} or Ti^{4+}, and O = O^{2-}.

The transition from the centrosymmetric prototype to any one of the non-centrosymmetric ferroelectric forms of PZT is accompanied by a lengthening of the unit cell along the newly developed polar axis. Slight shifts in the positions of A-site, B-site and O ions result in a separation between the centers of positive and negative charge within the unit cell and the creation of a dipole. To a first approximation, the shift of the tetravalent B-site cation along the polar axis is responsible for the dipole moment. For example, in the tetragonal structure, the central B-site cation is displaced along one of the 6 equivalent <001> directions, resulting in an elongation of the unit cell in that direction. Similarly, a shift along one of the 8 equivalent <111> directions produces a rhombohedral cell. To illustrate, Figure 2.12 shows the unit cell distortions in the tetragonal (4mm), orthorhombic (mm2) and rhombohedral (3m) phases of $BaTiO_3$, relative to the cubic prototype.

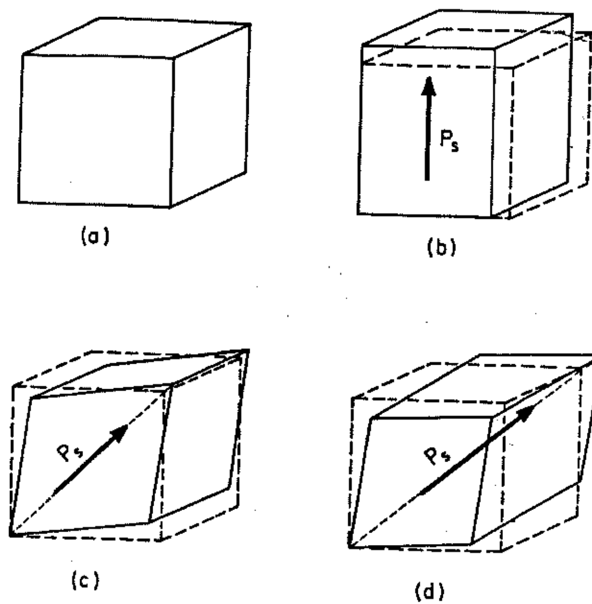

Figure 2.12 Unit cell distortions that result from the spontaneous polarization (P_s) in $BaTiO_3$. Dotted lines designate (a) the prototypic cubic (m3m) phase that exists above T_c. P_s can be oriented along (b) the 6 equivalent <001> directions in the tetragonal phase, (c) the 12 equivalent <011> directions in the orthorhombic phase and (d) the 8 equivalent <111> directions in the rhombohedral phase. All directions are in reference to the cubic prototype.[23]

2.3.2.2 Structure-Property Relations

At this point, a reexamination of the PZT phase diagram, Figure 2.10, is useful in rationalizing the superior dielectric and piezoelectric properties attainable in the solid solution system. Traditionally, it has been believed that, at a Zr/Ti ratio of ≈52/48, the morphotropic phase boundary (MPB) represents a tetragonal/rhombohedral structural change with composition at roughly constant temperature.[21] At this boundary, the phases possess the same thermodynamic stability and the B-site cation is free to shift in any of the 6 <001> or 8 <111> directions of the original cube. This results in 14 possible orientations of the spontaneous polarization, which greatly enhances polarizability and facilitates efficient poling. As expected, peaks in permittivity and piezoelectric

coefficients are observed at this composition. The fact that this phase boundary remains relatively constant with temperature is useful in many piezoelectric applications. Figure 2.13 shows a plot of relative permittivity (ε_r) and piezoelectric coupling coefficient (k) as a function of composition in the $PbZrO_3$–$PbTiO_3$ system. The square of the coupling coefficient (k^2) is defined as the ratio of output to input energies in the process of electromechanical energy conversion.

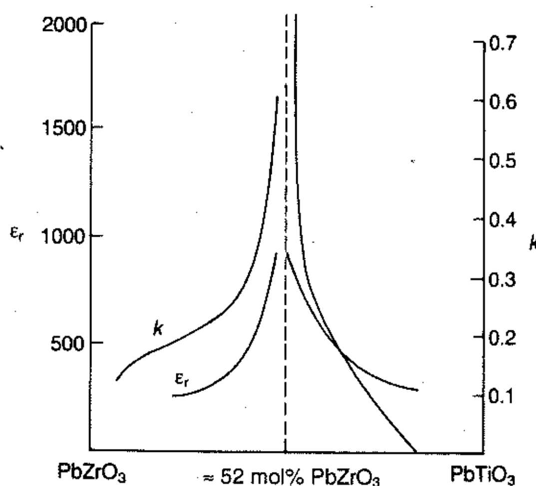

Figure 2.13 Compositional dependence of relative permittivity (ε_r) and piezoelectric coupling coefficient (k) the $PbZrO_3$–$PbTiO_3$ solid solution system. Note the peak in properties at the MPB.[21]

The recently discovered monoclinic phase brings this classical perception of the tetragonal/rhombohedral phase transition region into question.[22] However, these studies are still in their preliminary stages and the precise origin of PZT's superior electromechanical properties is by no means clearly understood.

2.4 Piezoelectricity

2.4.1 Fundamentals

All insulating materials will deform to some extent in response to an applied electric field. The phenomenon in which the induced strain (x_{ij}) is proportional to the square of the polarization (P_kP_l) is known as electrostriction and the constant of proportionality (Q_{ijkl}), the electrostrictive coefficient. The relationship is expressed in Equation 2.2.

$$x_{ij} = Q_{ijkl} P_k P_l \tag{2.2}$$

Materials that develop a dielectric displacement (or polarization) that is linearly proportional to an applied stress are termed piezoelectric, and the phenomenon, piezoelectricity. Similarly, the strain in the piezoelectric material is linearly proportional to an applied electric field. The constant of proportionality (d_{ijk}) is known as the piezoelectric coefficient and the expressions for the 'direct' and 'converse' piezoelectric effects are given as Equations 2.3 and 2.4, respectively. By convention, the first subscript in d_{ijk} is related to the electric field or displacement while the remaining coefficients are associated with the mechanical stress or strain. The d_{ijk} are numerically equivalent when expressed in this way. It should be noted, however, that if d_{ijk} is defined with respect to polarization ($P_i = d_{ijk} X_{jkl}$) it is no longer equal to those of Equations 2.3 and 2.4, though the difference is very small in perovskite ferroelectrics.[24]

$$D_i = d_{ijk} X_{jkl} \tag{2.3}$$

$$x_{jk} = d_{ijk} E_i \tag{2.4}$$

Another important distinction between piezoelectricity and electrostriction is that in electrostriction, deformation is independent of the polarity of the applied electric field.

By contrast, in piezoelectric materials the strain changes sign when the field polarity is reversed (at least well below the coercive field).

In materials where piezoelectric contributions are significant (and electrostriction can be ignored), transduction can be described using the piezoelectric equations of state[20] (Equations 2.5 and 2.6). These equations include piezoelectric, elastic and dielectric contributions.

$$D_i = d_{ijk} X_{jk} + \varepsilon_{il}{}^{X} E_l \tag{2.5}$$

$$x_{jk} = s_{jklm}{}^{E} X_{lm} + d_{ijk} E_i \tag{2.6}$$

D is dielectric displacement (C/m^2), X is applied stress (N/m^2), ε is absolute permittivity, E is applied electric field (V/m), and s is elastic compliance (m^2/N). The superscripted coefficients are held constant.

2.4.2 Tensor Treatment

It is evident from the above discussion that the piezoelectric coefficient (d_{ijk}) is a third rank tensor. However, not all 27 tensor components are independent. The condition that X_{ij} must be symmetrical dictates that d_{ijk} is symmetrical in j and k and reduces the number of independent coefficients to 18. This allows the use of more concise matrix notation.[25] Matrix notation reduces the number of subscripts from 3 in tensor notation (d_{ijk}) to 2 (d_{ij}). Additionally, to fully describe the property, the j subscript can take on any integral value between 1 and 6. Equations 2.7 and 2.8 present that way in which the d coefficient is described in tensor and matrix notation, respectively. Note that in tensor form d_{ijk} is a 3-dimensional (cubic) array.

$$d_{ijk} = \overset{\textit{1}^{st}\ \textit{Layer}}{\underset{i=1}{}}\begin{pmatrix} d_{111} & d_{112} & d_{113} \\ d_{112} & d_{122} & d_{123} \\ d_{113} & d_{123} & d_{133} \end{pmatrix} \overset{\textit{2}^{nd}\ \textit{Layer}}{\underset{i=2}{}}\begin{pmatrix} d_{211} & d_{212} & d_{213} \\ d_{212} & d_{222} & d_{223} \\ d_{213} & d_{223} & d_{233} \end{pmatrix} \overset{\textit{3}^{rd}\ \textit{Layer}}{\underset{i=3}{}}\begin{pmatrix} d_{311} & d_{312} & d_{313} \\ d_{312} & d_{322} & d_{323} \\ d_{313} & d_{323} & d_{333} \end{pmatrix} \quad (2.7)$$

$$d_{ij} = \begin{pmatrix} d_{11} & d_{12} & d_{13} & d_{14} & d_{15} & d_{16} \\ d_{21} & d_{22} & d_{23} & d_{24} & d_{25} & d_{26} \\ d_{31} & d_{32} & d_{33} & d_{34} & d_{35} & d_{36} \end{pmatrix} \quad (2.8)$$

The number of independent coefficients can be further reduced by crystal symmetry arguments. Neumann's Law states, "the symmetry elements of any physical property of a crystal must include the symmetry elements of the point group of that crystal."[25] For example, the Curie group of a poled polycrystalline ferroelectric, such as PZT, is ∞m (where the poling axis is defined as x_3). This conical symmetry eliminates all but the d_{15}, d_{24}, d_{31}, d_{32}, and d_{33} coefficients, and owing to planar isotropy perpendicular to the poling direction, $d_{31} = d_{32}$ and $d_{15} = d_{24}$. The d coefficient matrix for poled polycrystalline PZT is given as Equation 2.9.

$$d_{ij} = \begin{pmatrix} 0 & 0 & 0 & 0 & d_{15} & 0 \\ 0 & 0 & 0 & d_{15} & 0 & 0 \\ d_{31} & d_{31} & d_{33} & 0 & 0 & 0 \end{pmatrix} \quad (2.9)$$

2.4.3 Additional Piezoelectric Coefficients

In addition to d, there are three other piezoelectric coefficients (e, g and h) that are used for specific applications[20]. The e coefficient (C/m^2) relates applied strain to induced displacement at constant field. The g coefficient (V·m/N) relates the induced field to an

applied stress at constant dielectric displacement. The h coefficient (N/C) relates the induced stress at constant strain to a change in dielectric displacement. Explicit definitions of each of the four piezoelectric coefficients are given as Equations 2.10 through 2.13.

$$d_{ijk} = (\partial x_{jk} / \partial E_i)_X = (\partial D_i / \partial X_{jk})_E \quad (2.10)$$

$$e_{ijk} = (\partial D_i / \partial x_{jk})_E = (-\partial X_{jk} / \partial E_i)_x \quad (2.11)$$

$$g_{ijk} = (-\partial E_i / \partial X_{jk})_D = (\partial x_{jk} / \partial D_i)_X \quad (2.12)$$

$$h_{ijk} = (-\partial X_{jk} / \partial D_i)_x = (-\partial E_i / \partial x_{jk})_D \quad (2.13)$$

2.5 Domain and Lattice Contributions to Piezoelectric Properties in PZT

There are two distinct contributions to piezoelectric properties in ferroelectric materials in which both 180° and non-180° domain walls are possible (i.e. two or more possible axial orientations of the spontaneous polarization). All ferroelectric phases of PZT belong to this class. Lattice, or intrinsic, contributions encompass the responses of each individual unit cell of material. Domain, or extrinsic, contributions are those that arise primarily from the motion of domain walls. Understanding and controlling these contributions in PZT has been the topic of extensive research efforts.

2.5.1 Lattice Contributions

Intrinsic piezoelectric coefficients can be directly correlated to dielectric, ferroelectric, and electrostrictive properties. For instance, Equations 2.14 and 2.15 were derived using phenomenological theory and relate the transverse piezoelectric coefficient

(d_{31}) to permittivities, electrostrictive coefficients, and the polarization for tetragonal and rhombohedral PZTs, respectively.[26]

$$d_{31} = 2\varepsilon_o \varepsilon_{33} Q_{12} P_3 \tag{2.14}$$

$$d_{31} = 2\varepsilon_o [\varepsilon_{11} Q_{12} + \varepsilon_{12}(Q_{11} + Q_{12})] P_3 \tag{2.15}$$

ε_o is the permittivity of free space (8.854×10^{-12} F/m), ε_{33}, ε_{11}, and ε_{12} are relative permittivities, Q_{11} and Q_{12} are electrostrictive coefficients, and P_3 is the spontaneous polarization.

It is important to recognize that while electrostrictive coefficients are weakly temperature dependent (and generally assumed constant for a given composition), intrinsic permittivity and polarization vary considerably with temperature in PZT materials. The absolute value of permittivity increases rapidly with temperature as T_c is approached (Figure 2.14) while the spontaneous polarization shows the opposite trend, disappearing at T_c (Figure 2.15).

And in accordance with Equations 2.14 and 2.15, the considerable dependence of dielectric and ferroelectric properties on temperature gives rise to temperature dependence in the intrinsic d_{31} piezoelectric coefficient (Figure 2.16).

2.5.2 Domain Contributions

Extrinsic contributions associated with the motion of non-180° domain walls act to further enhance the piezoelectric effect. Despite being a major contributor to the dielectric response, 180° domain wall motion does not contribute to piezoelectricity because there is no associated strain change.

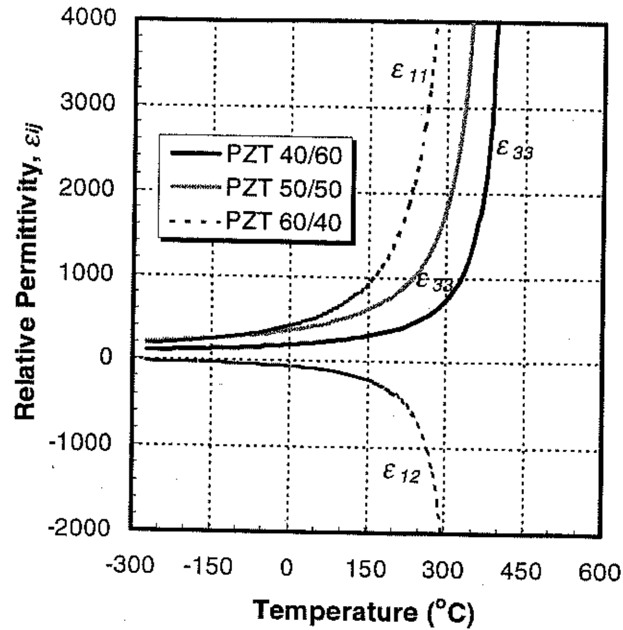

Figure 2.14 Phenomenologically-derived values of intrinsic relative permittivity (ε_{ij}) of PZT as a function of temperature for tetragonal (PZT 40/60), near MPB (PZT 50/50), and rhombohedral (PZT 60/40) compositions. The ε_{33} coefficient is plotted for PZT 40/60 and 50/50 while ε_{11} and ε_{12} are shown for PZT 60/40. Equations taken from Haun.[26]

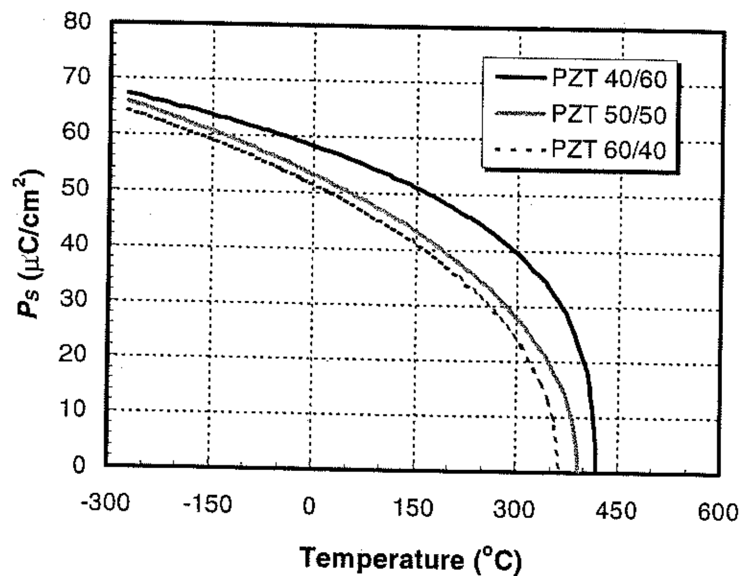

Figure 2.15 Phenomenologically-derived values of spontaneous polarization (P_S) of PZT as a function of temperature for tetragonal (PZT 40/60), near MPB (PZT 50/50), and rhombohedral (PZT 60/40) compositions. Equations taken from Haun.[26]

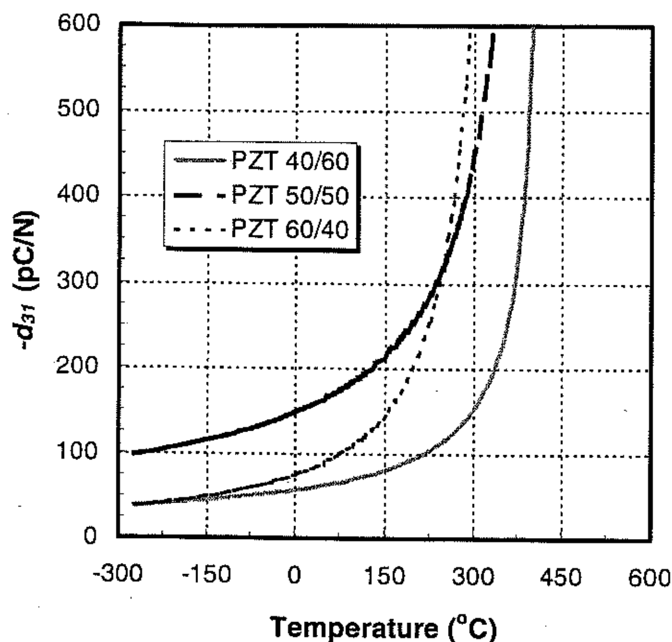

Figure 2.16 Phenomenologically-derived values of the intrinsic piezoelectric d_{31} coefficient of PZT as a function of temperature for tetragonal (PZT 40/60), near MPB (PZT 50/50), and rhombohedral (PZT 60/40) compositions. Equations taken from Haun.[26]

One way to distinguish between domain and lattice contributions to properties is to conduct electrical property measurements near 0 K. Since domain wall motion is a thermally-activated process (domain wall mobility increases with temperature), this can be used to effectively "freeze out" extrinsic contributions. Zhang *et al.*[27] measured the dielectric and piezoelectric properties of Navy-type 1, 2, 3, and 4 PZT ceramics down to liquid helium temperatures (Figure 2.17). These samples had base PZT compositions near the MPB and were modified by either "soft" or "hard" dopants. Soft dopants, such as those in types 2 and 4, facilitate (or at least do not substantially impede) domain wall mobility, which can lead to higher piezoelectric coefficients and dielectric permittivities and losses, lower coercive fields, and a greater temperature dependence of properties. Hard dopants, such as those in types 1 and 3, minimize dielectric losses and temperature

coefficients of dielectric and piezoelectric properties at the expense of lower permittivities and piezoelectric coefficients and higher coercive fields.

As shown in Figure 2.17, compositions modified by softeners showed considerably higher properties at room temperature due to differences in the magnitude of extrinsic contributions to the dielectric and piezoelectric response. But despite significant differences at room temperature, properties converged as temperatures neared 0 K. Clearly, dopant effects (domain contributions) were eliminated at extremely low temperatures and only intrinsic properties remained.

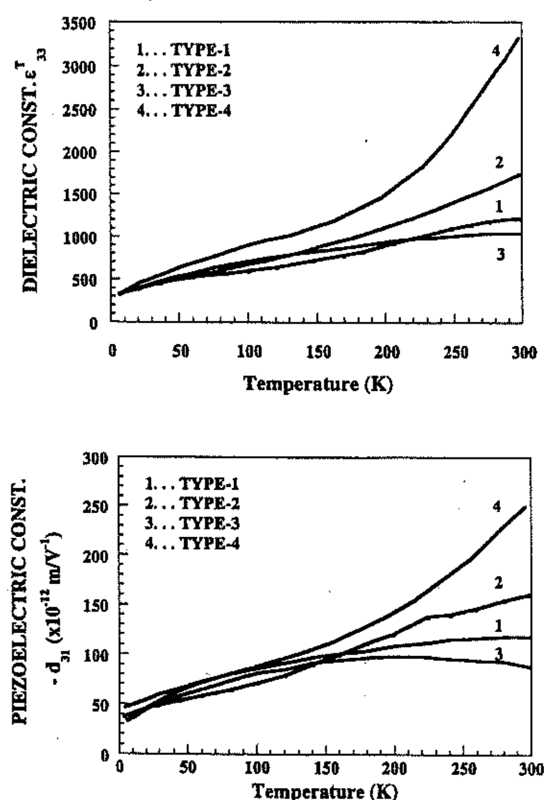

Figure 2.17 Temperature dependence of relative permittivity (ε_{33}) and transverse piezoelectric coefficient (d_{31}) measured between 4.2 and 300 K for Navy-type 1, 2, 3, and 4 PZT ceramics (from Zhang[27]). All have base PZT compositions near the MPB. Types 2 and 4 are doped with softeners Nb_2O_5 and Sb_2O_3, respectively. Types 1 and 3 are doped with hardeners NiO and Fe_2O_3, respectively.

2.6 Film Considerations

In most cases, thin (≤1 μm) or thick (≥1 μm) film ferroelectric materials behave somewhat differently from bulk materials of the same composition. Films tend to have smaller dielectric, ferroelectric, and piezoelectric properties in comparison with their ceramic counterparts.[2] Several factors can be identified to qualitatively account for these differences. Clamping to the substrate and residual film stresses are two of the most important. First, the film is rigidly clamped to the substrate on which it was deposited and therefore is not free to expand or contract in response to electrical stimuli. This constraint imposed by the substrate results in reduced (or "clamped") dielectric, ferroelectric, and electromechanical responses. As a result, effective piezoelectric coefficients are reported for films, and these will be discussed in section 2.6.1. In addition, because ferroelectric films require high temperatures for crystallization (typically >600°C), differences in thermal expansion characteristics between the film and substrate materials give rise to significant residual stresses at room temperature. This can lead to substantial local stresses that make non-180° domain wall motions difficult, severely hindering extrinsic contributions to the piezoelectric effect in ferroelectric films. Other possible factors that may lead to a difference in measured properties of film materials include phase transformation stresses, grain size effects, and crystallographic orientation.[28]

Xu *et al.*[29] investigated contributions from extrinsic sources, notably 180° and non-180° domain wall motions, in PZT films by measuring the stress and field dependence of dielectric, ferroelectric, and piezoelectric responses. They examined MPB compositions of varying thickness. It was discovered that there is a very weak

dependence (<2%) of dielectric permittivity on compressive normal stresses up to 20 MPa in films ranging from 0.5 to 3 μm (Figure 2.18a). In addition, changes in remanent polarization and coercive field were negligible. Results indicate difficulty in reorienting domains to directions closer to the film plane and thus limited ferroelastic non-180° domain wall motions. This argument was further supported by measurement of the longitudinal piezoelectric coefficient d_{33} as a function stress[29] (Figure 2.18b). The d_{33} coefficient was constant up to 6 MPa for a 1 μm film while a nonlinear increase of ~20% was observed in a bulk ceramic sample. Changes in piezoelectric activity with applied stress is indicative of non-180° domain wall contributions.

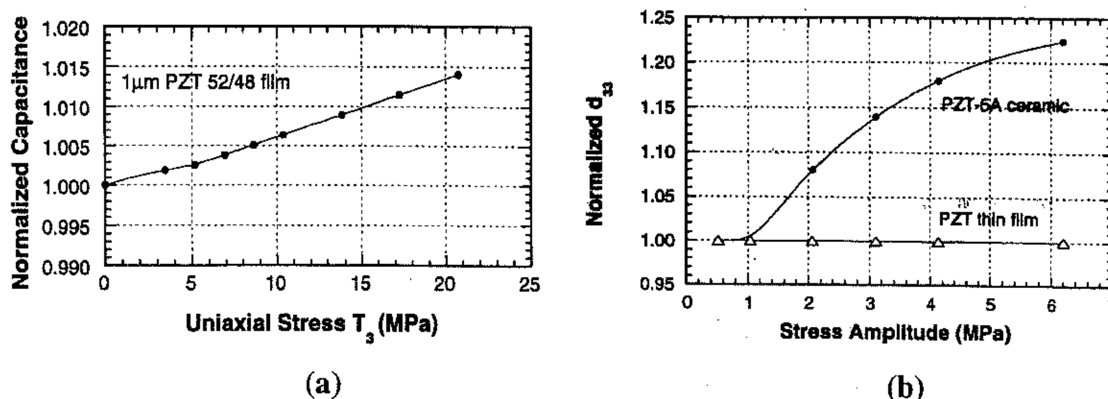

Figure 2.18 Plots of normalized (a) capacitance and (b) d_{33} piezoelectric coefficient as a function of applied stress for a poled 1 μm <111>-oriented PZT 52/48 film with an average grain size ~100 nm (from Xu *et al.*[29]). To illustrate extrinsic contributions to piezoelectric properties in the bulk, a PZT-5A bulk ceramic is also shown in (b).

Dielectric and piezoelectric measurements were also made as a function of applied AC field. Films of three different thicknesses (1.5, 3.2, and 6.7 μm) were examined and results are shown in Figure 2.19. The dielectric constant was found to increase nonlinearly with thickness for all films (Figure 2.19a). Different behavior was observed in the longitudinal piezoelectric coefficient (Figure 2.19b). Thinner films (1.5

μm) showed little change in d_{33} as the field was increased, while a significant nonlinear increase was found in the 6.7 μm-thick film. Additionally, the threshold field for the onset of nonlinearity decreased with increasing film thickness.

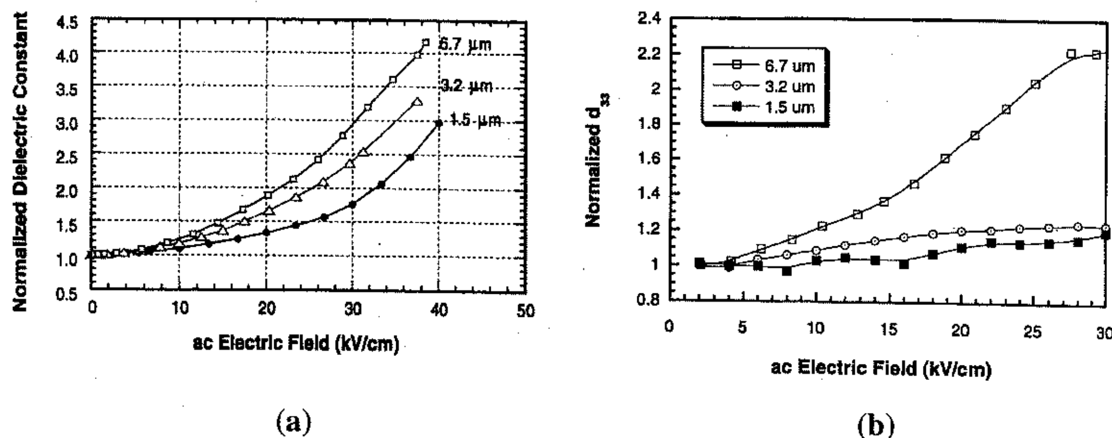

Figure 2.19 Plots of normalized (a) dielectric constant and (b) d_{33} piezoelectric coefficient as a function of AC field at 1 kHz. All films were poled at 250 kV/cm at room temperature and randomly oriented with an average grain size ~100 nm (from Xu *et al.*[29]).

Two important conclusions can be drawn from these data. First, for films thicker than 2 μm, dielectric and piezoelectric coefficients showed larger increases with increasing film thickness, which indicates that contributions from extrinsic sources become more significant as film thickness increases. The fact that the threshold field for the onset of piezoelectric nonlinearity decreased with increasing film thickness implies that non-180° domain wall pinning is reduced in thicker films. Non-180° domain wall pinning is severe in PZT thin films and therefore extrinsic contributions to piezoelectric properties are limited in films <2 μm. Possible reasons for higher extrinsic contributions in thicker films include larger grain size and reduced film/substrate interfacial effects. Second, the huge difference in nonlinearity between permittivities and piezoelectric

coefficients suggests that 180° domain wall motions represent a larger portion of the extrinsic dielectric response in PZT films, as compared to non-180° wall motions.

Xu *et al.*[29] also conducted temperature dependent dielectric measurements down to 4.2 K, which were similar to those done by Zhang *et al.*[27] on bulk ceramic samples. In films of varying thickness, orientation, and average grain size, permittivities were found to converge near 0 K where extrinsic contributions were frozen out (Figure 2.20). Based on room temperature permittivity values, increasing thickness, <100> preferred orientation, and larger grain size all contributed to a greater extrinsic dielectric response in PZT films. These results were in agreement with their stress and field dependent property measurements.

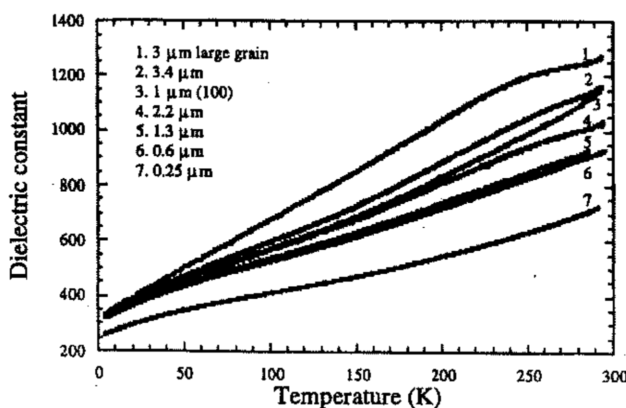

Figure 2.20 Temperature dependence of dielectric constant (ε_{33}) of several chemical solution deposited PZT 52/48 films measured at 1 kHz between 4.2 and 298 K. Films 1 and 3 are <100>-oriented while 2, 4, 5, and 6 are <111>-oriented (from Xu *et al.*[29]).

2.6.1 The Effective Transverse Piezoelectric Coefficient $e_{31,f}$

The differences in boundary conditions between bulk ceramics and films create a need for describing the properties of film materials in terms of "effective" coefficients. This terminology acknowledges the various effects such as residual stress and substrate

clamping that influence measured properties in films. A subscript "*f*" is commonly used to indicate an effective coefficient (i.e. $d_{31,f}$). Along with the value of an effective property coefficient, it is useful to specify film thickness, texture, grain size, deposition technique, etc. To illustrate the wide range of possible magnitudes of a single film property, some effective transverse piezoelectric coefficient $e_{31,f}$ values of PZT films with differing thickness, composition, and texture and prepared by different deposition methods are given in Table 2.2.

Table 2.2 Effective transverse piezoelectric coefficients of various PZT films[30]. The bulk e_{31} coefficient has been included for comparison[20].

Form	*Deposition Method*	*Zr/Ti Ratio*	*Preferred Orientation*	*Thickness (μm)*	$e_{31,f}$ *(C/m²)*	e_{31} *(C/m²)*
Thin Film	Sputtered	45/55	<100>	0.43	-3.78	--
Thin Film	Sol-gel	45/55	<111>	0.90	-8.28	--
Thin Film	Sol-gel	53/47	<111>	0.88	-6.83	--
Ceramic	--	53/47*	random	--	--	-5.2

* Sample was doped with 6 mol% Sr which occupied A-sites.

For many years, research groups throughout the world have reported the effective transverse piezoelectric coefficient $d_{31,f}$ of PZT films. Unfortunately, calculation of this coefficient requires that the film's elastic constants are accurately known. Since the elastic constants of PZT films are often unavailable, $e_{31,f}$ is the more appropriate coefficient for describing the transverse electromechanical characteristics of a PZT film.[12]

As discussed previously, the *e* piezoelectric coefficient correlates applied strain and induced dielectric displacement at constant field. Taking into account clamping by

the substrate, Equation 2.16 relates effective film coefficients $e_{31,f}$ to bulk values of d_{31}, e_{31}, and e_{33} through elastic parameters.[12]

$$e_{31,f} = \frac{d_{31}}{s_{11}^{E} + s_{12}^{E}} = e_{31} - \frac{c_{13}^{E}}{c_{33}^{E}} e_{33} \tag{2.16}$$

s_{ij}^{E} (m^2/N) and c_{ij}^{E} (N/m^2) correspond to film elastic compliance and stiffness coefficients, respectively, measured at constant field.

We see that intrinsically $|e_{31,f}| > |e_{31}|$ and this circumstance arises from the mechanical boundary conditions of a film/substrate composite.[12] It is simplest to visualize for the converse piezoelectric effect, where the e coefficient relates applied electric field to induced stress (Equation 2.11). A film is free to move in the longitudinal direction yet is restricted by the substrate within the plane. A field applied in the thickness direction will facilitate the development of larger transverse stresses in comparison with an unconstrained situation (as in a bulk material) where these stresses can be partially relieved by expansion/contraction.

2.6.2 The Effective Electrostrictive Coefficient Q_f

It is also important to recognize that the free electrostriction coefficient of a material may be modified by in-plane substrate constraints, texture, size effects, etc. that are associated with a film. Again, it is useful to define an effective coefficient that averages individual strains within each domain and takes these factors into account.

Kholkin *et al.*[31] conducted an extensive study of the effective electrostriction coefficients (Q_f) of ferroelectric thin films that placed primary emphasis on PZT. Values were calculated from measured relative permittivity ($\varepsilon_{33,f}$), remanent polarization, and

longitudinal piezoelectric coefficient ($d_{33,f}$) data using a polydomain modification of Equation 2.14 given by Equation 2.17.

$$Q_f = \frac{d_{33,f}}{2\varepsilon_o \varepsilon_{33,f} P_r} \tag{2.17}$$

Figure 2.21 is a plot of Q_f as a function of electric field for a <111>-textured PZT 45/55 thin film. Strong anomalies near the coercive field are a consequence of small differences in coercive fields determined through static ($d_{33,f}$ and $\varepsilon_{33,f}$) and dynamic (P_r) measurements. Q_f was thereby found to increase slightly with field, regardless of polarity, which is indicative of the weak (but nevertheless, significant) non-180° domain contribution to piezoelectric properties in PZT thin films.

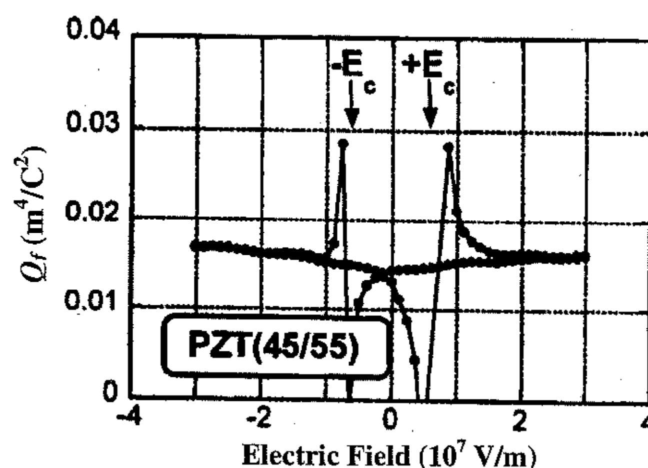

Figure 2.21 Effective electrostriction coefficient of a <111>-oriented, 0.3 μm-thick PZT 45/55 film prepared by a modified sol-gel process plotted versus electric field.[31] Values were extrapolated from measured dielectric, ferroelectric, and piezoelectric data through Equation 2.17.

A number of sol-gel prepared PZT thin films of various composition and orientation were analyzed in a similar fashion. Results are shown in Figure 2.22. Additionally, upper and lower limits of Q_{11} for PZT ceramics (corresponding to parallel

and series models, respectively) that were derived using polycrystalline averaging equations and available ceramic data[26] are given. It was clear that effective coefficients in films were suppressed from corresponding values in ceramics. Substrate clamping, film texture, and possible size effects were given as primary causes for the reduction.[31]

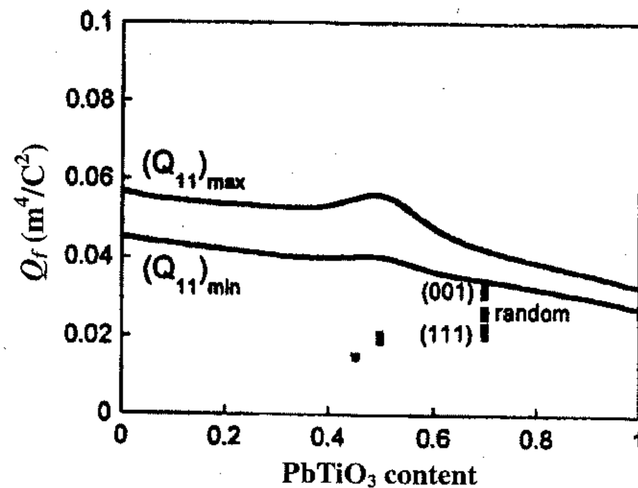

Figure 2.22 Measured values of Q_f for differently textured PZT thin films (from Kholkin *et al.*[31]) plotted as a function of composition. As comparison, thermodynamic calculations[26] of upper and lower limits of Q_{11} are shown for bulk PZT.

The effect of in-plane constraints imposed by the substrate on the electrostriction coefficient was quantified. For the case of perfect clamping, where transverse deformation is restricted but longitudinal deformation is unconstrained, the Q_f of Equation 2.17 is related to bulk coefficients Q_{11} and Q_{12} and film elastic compliances $s_{11}{}^D$ and $s_{12}{}^D$ through Equation 2.18.[31]

$$Q_f = Q_{11} - 2\frac{s_{12}{}^D}{s_{11}{}^D + s_{12}{}^D} Q_{12} \tag{2.18}$$

Note that Equation 2.18 is suitable only for polycrystalline films poled perpendicular to the substrate plane (conical ∞m symmetry).

Finally, it was discovered that effects associated with substrate clamping and film orientation may modify the compositional dependence of the effective electrostrictive coefficients in PZT thin films.[31] In <111>-textured films, measured Q_f coefficients for rhombohedral (70/30) films were larger than those for tetragonal (45/55) ones, which is opposite that predicted by phenomenological theory.

2.7 Temperature Dependence of Piezoelectric Properties of PZT Ceramics

2.7.1 Bulk Ceramics

Both intrinsic and extrinsic sources contribute to the piezoelectric properties of PZT and each of these contributions is markedly dependent on temperature. The temperature dependence of intrinsic piezoelectric properties has been discussed formerly and the phenomenological d_{31} coefficient is plotted in Figure 2.16 for several PZT compositions. Because the intrinsic piezoelectric coefficients increase rapidly with temperature toward T_c, their greatest temperature dependence is expected in ranges nearest to T_c.

For virtually all piezoelectric devices involving PZT, large piezoelectric coefficients with minimal temperature dependence are desired. One would therefore think to choose a composition with a very high T_c, far from the operating temperature range. Amin *et al.*[32] measured the Curie temperatures of pure PZT ceramics as a function of Zr/Ti ratio across the entire solid solution system (Figure 2.23). T_c was found to increase gradually with $PbTiO_3$ content from a minimum of 212°C in $PbZrO_3$ to 492°C in $PbTiO_3$. Based on these results, more highly Ti-rich PZT compositions possess the

highest Curie temperatures, which generally result in the smallest temperature dependence of intrinsic piezoelectric properties.

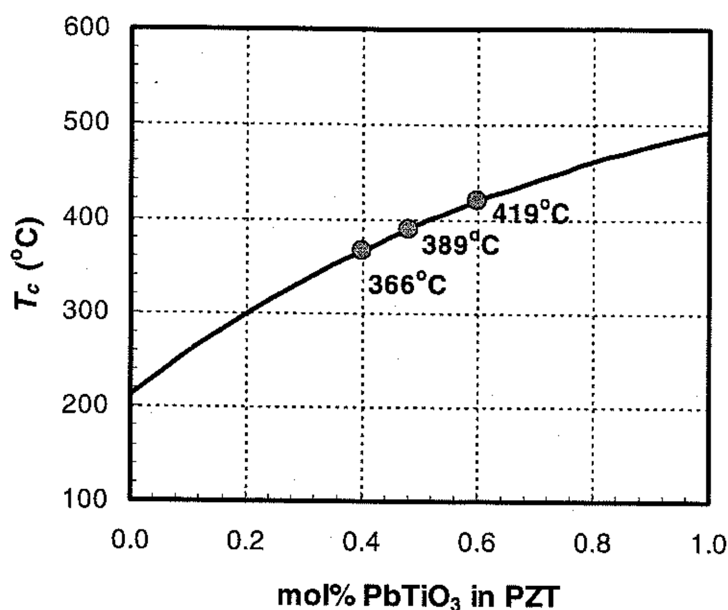

Figure 2.23 Experimental fit of Curie temperature (T_c) as a function of composition across the $Pb(Zr,Ti)O_3$ solid solution system.[32] PZT 60/40, 52/48, and 40/60 compositions are highlighted.

In PZT ceramics, sizeable domain contributions can add to measured electromechanical responses and these relative contributions can be strongly dependent upon temperature. To illustrate, it is useful to re-examine the permittivity vs. temperature data for PZT films of varying thickness presented by Xu *et al.*[29] (Figure 2.20). As the temperature was raised from 4.2 to 300 K, an increase in the difference in permittivities between thick and thin films of similar microstructure and orientation was seen. Results suggest that extrinsic contributions to dielectric properties increase with temperature, and that these contributions are larger in thicker films. Similar observations were made previously for bulk PZT ceramics modified by different dopants.[27]

Wang *et al.* measured piezoelectric *d* coefficients of commercially available PZT-5H ceramics using bonded strain gages to measure the three pertinent strains (x_{11}, x_{33}, and x_{13}). Temperature variable measurements were made in an environmental test chamber and d_{31} results are shown in Figure 2.24. An increase of 42% from -55°C to 85°C was observed.

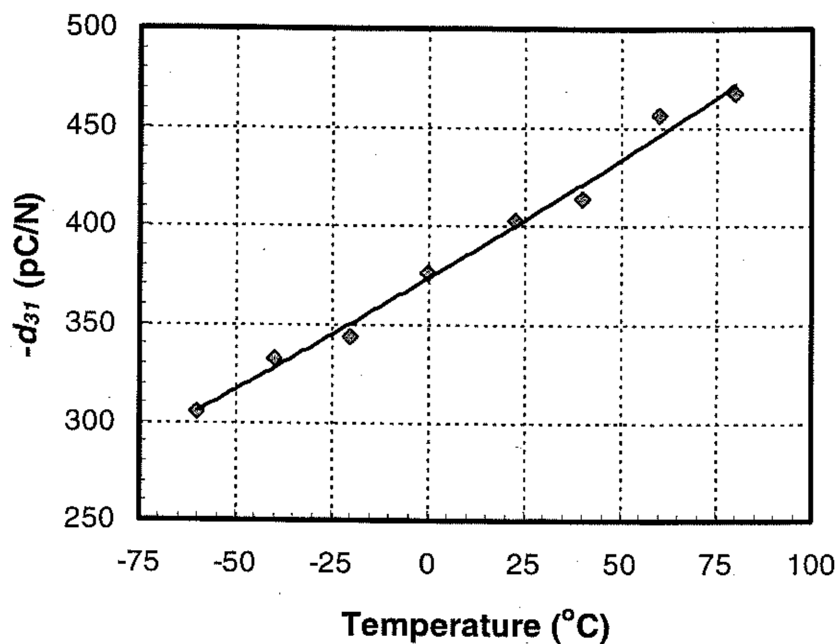

Figure 2.24 Temperature dependence of the transverse piezoelectric coefficient d_{31} of PZT-5H ceramic samples measured under large electric fields (up to 5 kV/cm).[33]

To this point, the discussion has been limited to temperature dependent electromechanical properties of bulk PZT materials. Owing to difficulties in making piezoelectric coefficient measurements of films as a function of temperature, no data has been found in the literature that elucidates the temperature dependence of the piezoelectric response in PZT films.

2.7.2 Elastic Moduli

According to Equation 2.16, the clamped piezoelectric coefficient $e_{31,f}$ of a film is related to its free d_{31} through its elastic moduli (s_{ij}^E or c_{ij}^E). Therefore, predictions of $e_{31,f}$ versus temperature behavior could be made on the basis of experimental measurements of these coefficients. It has been shown that bulk d_{31} coefficients are strongly dependent on temperature (Figure 2.24) but reliable data on the elastic moduli of PZT films (at any temperature) are unavailable.

Zhuang *et al.* measured the elastic compliance coefficients (s_{11}^E) of pure PZT ceramics with several Zr/Ti ratios as a function of temperature from 4.2 to 300 K using a resonance technique.[34] Results are plotted in Figure 2.25. As expected, the compliance coefficients increased with temperature for all compositions. Near MPB compositions showed the strongest dependence on temperature. The apparent drop-off in s_{11}^E on heating above 225 K is most likely due to an aging effect and s_{11}^E is expected to continue to increase monotonically with temperature, to at least 100°C.[35]

The temperature dependence of s_{11}^E is expected to be even lower (than those of Figure 2.25) if only intrinsic contributions are considered. Herbiet *et al.*[36] derived an approximate form of the temperature dependence of $s_{11,intrinsic}$ in PZT compositions near the MPB. A phenomenological model of a vibrating non-180° domain wall in electric and mechanical stress fields (previously reported by Arlt[37]), along with resonance measurements of several undoped PZT ceramics over a range of temperature, were used in the derivation. Results are plotted in Figure 2.26. The greatest temperature dependence of the $s_{11,intrinsic}$ was observed at the MPB (PZT 52/48) where rhombohedral and tetragonal phases coexist.

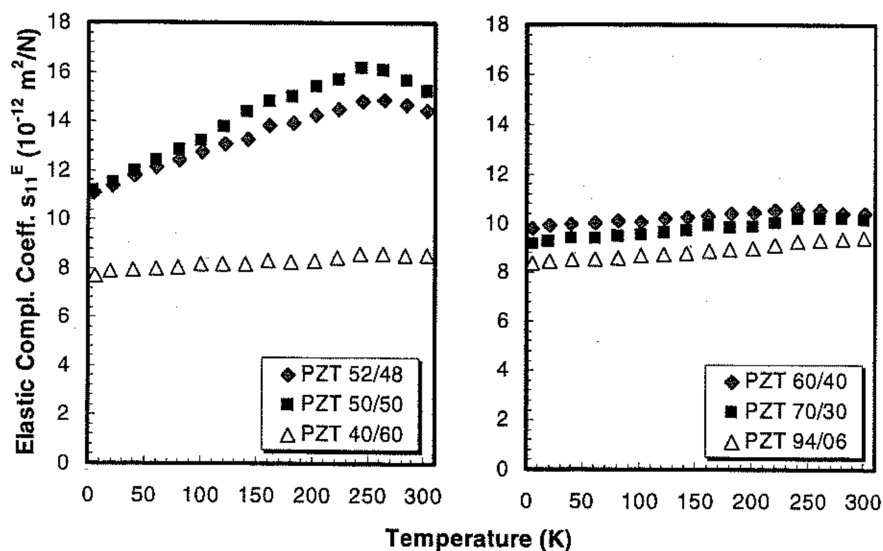

Figure 2.25 Low temperature elastic compliance coefficient (s_{11}^{E}) plotted as a function of temperature for several tetragonal and rhombohedral PZT compositions.[34]

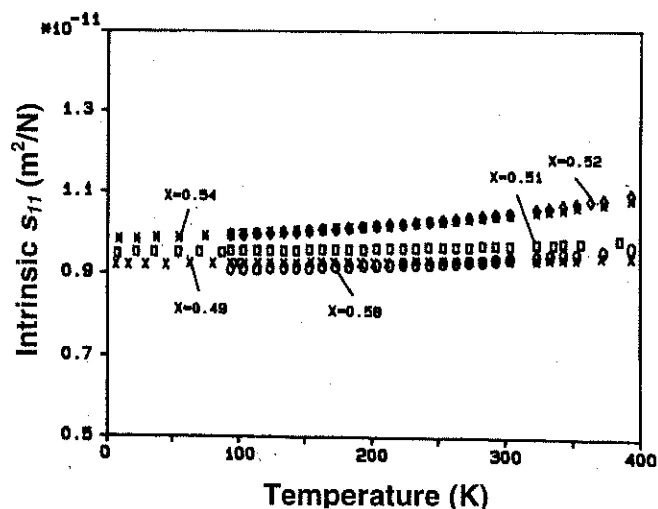

Figure 2.26 Intrinsic contributions to s_{11} derived from measured data for undoped $Pb(Zr_xTi_{1-x})O_3$ ceramics (from Herbiet *et al.*[36]).

2.8 Compositional Dependence of Piezoelectric Properties of PZT

2.8.1 Bulk Ceramics

The compositional dependence of electromechanical properties has been well characterized for bulk PZTs. A plot of piezoelectric *d* coefficients as a function of $PbZrO_3$ content in undoped compositions is given as Figure 2.27. All *d* coefficients peak at the MPB (Zr/Ti ≈ 52/48).

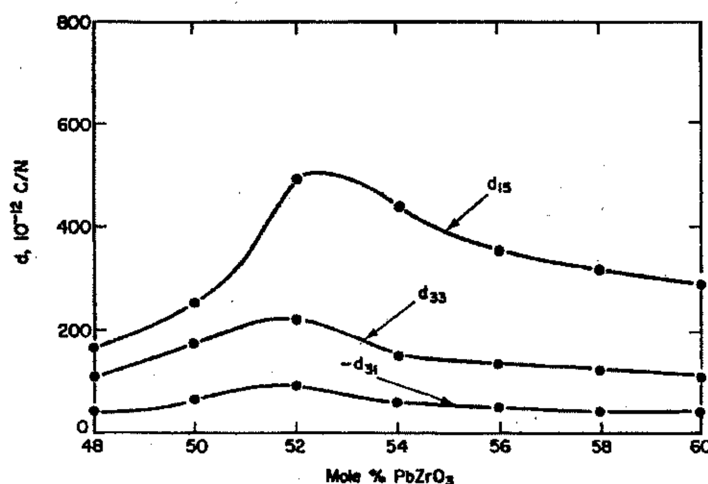

Figure 2.27 Composition dependence of bulk ceramic piezoelectric *d* coefficients around the MPB[20]. Maximum values occur at 52 mol% $PbZrO_3$.

2.8.2 Films

In addition, several groups have reported $e_{31,f}$, $d_{31,f}$, or $d_{33,f}$ for PZT films as a function of composition. It is interesting to note that their results do not agree on a single composition of maximum piezoelectric activity. Key articles on the subject have come from the Swiss Federal Institute of Technology (Lausanne, Switzerland) and The Pennsylvania State University (University Park, PA).

One of the first comprehensive studies of dielectric, ferroelectric, and piezoelectric property variation as a function of Zr/Ti ratio in PZT films was done in

1995 by Chen *et al.*[38] ε_{33}, P_r, and effective d_{33} of 1 μm sol-gel films deposited on platinum-coated silicon substrates (poled at 150 kV/cm for 2 min at room temperature) were measured (Figure 2.28). $d_{33,f}$ coefficients were determined by double-beam laser interferometry. Peaks in property coefficients were found to coincide with those for bulk ceramics of the same composition, occurring at the MPB composition PZT 52/48. As expected, the magnitudes of effective film properties were lower than bulk properties, and differences were attributed to substrate clamping effects and unoptimized poling conditions.

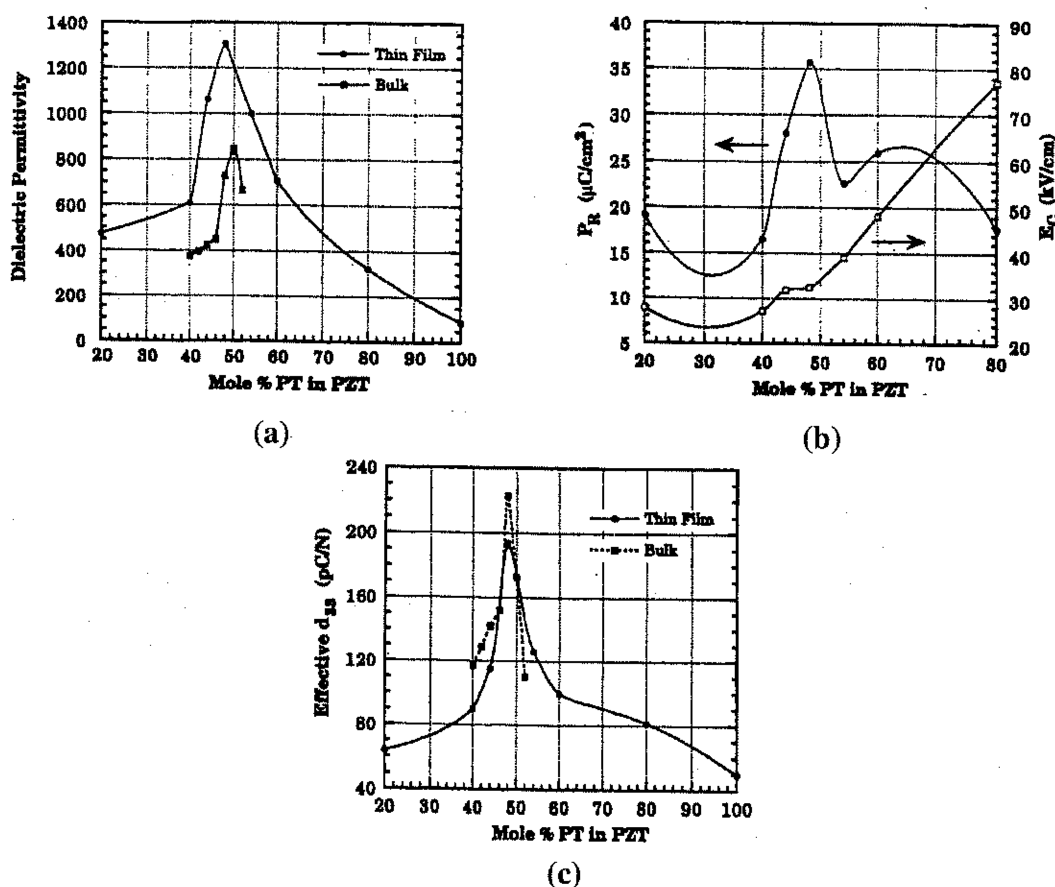

Figure 2.28 (a) Dielectric permittivity, (b) remanent polarization and coercive field, and (c) effective d_{33} as a function of Zr/Ti ratio in 1 μm sol-gel PZT films.[38] Maximum values of ε_{33}, P_r, and $d_{33,f}$ are located at the MPB PZT 52/48 composition and correspond to bulk maxima. Bulk data were taken from Berlincourt *et al.*[39]

Several years later, Xu reinforced Chen's contention that piezoelectric activity was maximized in films of the MPB composition.[28] In this work, $d_{33,f}$ coefficients were measured using the pneumatic pressure charge technique.[40] Films were sol-gel prepared, 1 μm in thickness, and poled at 150 kV/cm for 10 min at room temperature. They were deposited on either Pt<111> or Pt<100>-coated silicon substrates. As film orientation was controlled by the orientation of the bottom electrode, films deposited on Pt<111> and Pt<100> were strongly <111> and <100>-textured, respectively. Measured properties are tabulated in Table 2.3. Despite magnitude differences between <111> and <100>-oriented films, maxima in ε_{33}, P_r, and $d_{33,f}$ were observed at the MPB composition.

Table 2.3 Dielectric permittivity, remanent polarization, and effective d_{33} of several 1 μm sol-gel deposited PZT films with different preferred orientations and Zr/Ti ratios near the MPB.[28]

Texture		<111>			<100>	
Zr/Ti ratio	48/52	52/48	56/44	48/52	52/48	56/44
ε_{33}	950-1000	950-1000	950-1000	1030-1080	1150-1200	1000-1050
P_r ***(μC/cm²)***	23-26	27-30	20-23	21-24	24-27	17-20
$d_{33,f}$ ***(pC/N)***	100-105	110-120	80-85	90-95	95-105	75-80

Dubois *et al.* measured both $d_{33,f}$ and $e_{31,f}$ of PZT thin films with different Zr/Ti ratios around the MPB[30]. Films were deposited either by sol-gel or reactive sputtering on platinum-coated silicon wafers with either TiO_2 or Ta adhesion layers. Sol-gel films were all <111>-textured and ~900 nm in thickness. Sputtered films were thinner (~500 nm) and <100> texture was achieved using the Ta adhesion layer. $d_{33,f}$ was determined by double-beam laser interferometry. $e_{31,f}$ was measured by forced deflection of a

clamped cantilever. In this technique, a small alternating displacement (resulting in ~20 $\mu\varepsilon$ along the beam length) is superimposed on a static strain and the piezoelectrically-generated charge in the film is collected.

The largest $e_{31,f}$ was obtained at a tetragonal PZT 45/55 composition (Figure 2.29) while $d_{33,f}$ was observed to peak at the MPB (PZT 53/47). The authors attributed the shift and broadening of the $e_{31,f}$ peak, as compared to the relatively sharp MPB peak observed in the bulk, to substrate clamping and differences in film and bulk elastic compliance coefficients (s_{ij}). In the case of a film clamped to a substrate, $d_{33,f}$ and $e_{31,f}$ are both related to bulk piezoelectric coefficients through elastic compliances as defined by Equation 2.19.

$$d_{33,f} = d_{33} - \frac{2s_{13}{}^{E}}{s_{11}{}^{E} + s_{12}{}^{E}} d_{31} = d_{33} - 2s_{13}{}^{E} e_{31,f} \tag{2.19}$$

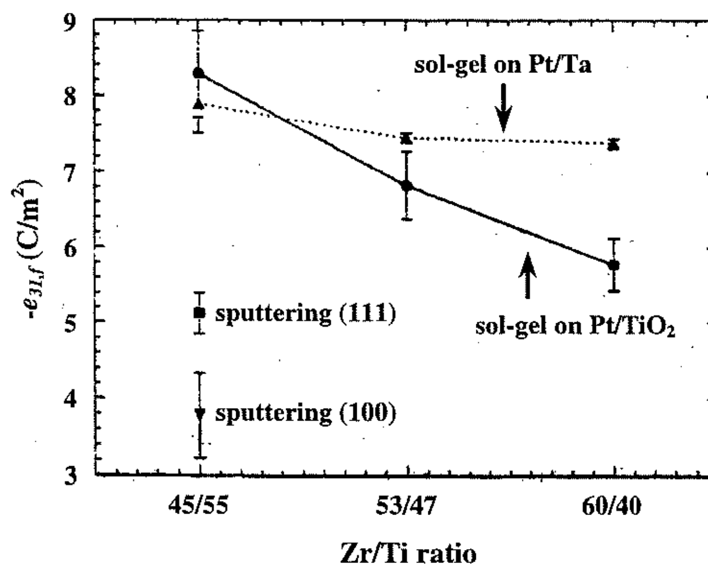

Figure 2.29 Variation of effective transverse piezoelectric coefficient $e_{31,f}$ with composition for several PZT thin films[30]. The highest $e_{31,f}$ values were observed on the tetragonal side of the MPB (PZT 45/55).

Further evidence of a shift in the composition of maximum piezoelectric activity of PZT thin films away from the MPB and toward more tetragonal compositions was presented by Hiboux *et al.*[41] The $d_{33,f}$ coefficients of reactively sputtered, 300 nm-thick PZT films of <111> and random orientation were measured using double-beam laser interferometry.

Samples with $PbZrO_3$ contents between 10 and 70 mol% in steps of 5-10 mol% were measured and peaks were observed in $d_{33,f}$ at the tetragonal PZT 40/60 composition for <111>-oriented films on Pt electrodes (Figure 2.30). For random films on RuO_2 electrodes, peaks in as-grown (virgin) and maximum (poled) $d_{33,f}$ values occurred at PZT 35/65 and 55/45 compositions, respectively.

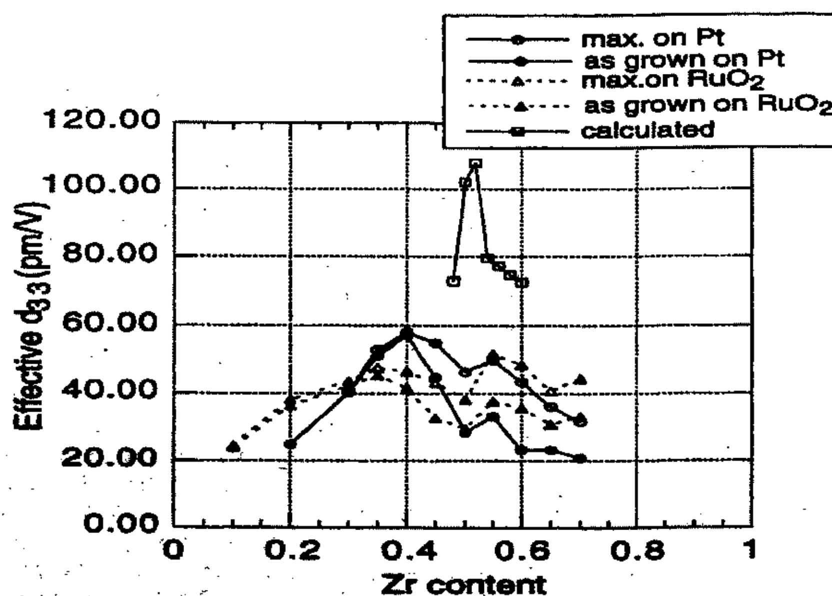

Figure 2.30 As-grown (virgin) and maximum (poled) values of $d_{33,f}$ in reactively sputtered PZT thin films deposited on Pt<111> and RuO_2-coated substrates.[41] Calculated results represent bulk ceramic data that is corrected for the substrate clamping condition.

The contradictions between results in the above studies emphasize the idea that processing conditions significantly impact properties (and likely poling efficiency) in ferroelectric thin films.

2.8.3 Elastic Moduli

In addition to temperature, the elastic moduli of PZT are dependent on Zr/Ti ratio. To reiterate, reliable data on the elastic properties of PZT films of different composition and thickness are unavailable. However, Zhuang *et al.* measured the elastic compliance coefficient s_{11}^{E} and Poisson's ratios ($\nu = -\frac{s_{12}}{s_{11}}$) of pure PZT ceramics across much of the solid solution system at constant temperature[34] (Figure 2.31). Both measured coefficients were found to rise sharply near and pass through a maximum at the MPB composition ($\approx$ 48 mol% $PbTiO_3$).

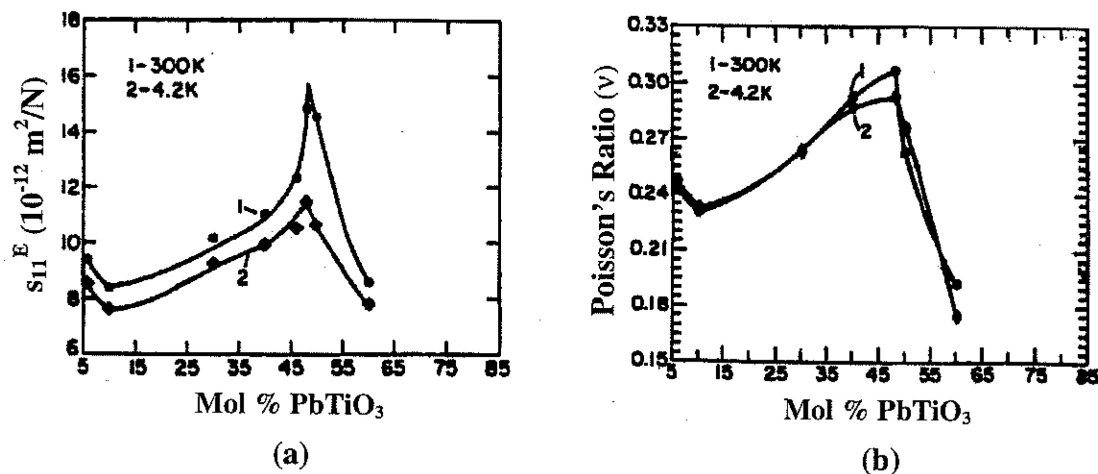

Figure 2.31 (a) Elastic compliance coefficient (s_{11}^{E}) and (b) Poisson's ratio (ν) at 4.2 and 300 K plotted as a function of PZT composition.[34]

Chapter 3 : Experimental Procedure

3.1 Introduction

This chapter provides details on the PZT film processing and electrical characterization, a brief summary of MEMS accelerometer design, fabrication, and testing methods as well as the experimental procedure used in development of the modified wafer flexure technique.

3.2 Lead Zirconate Titanate Film Preparation

Chemical solution spin-on deposition is a popular technique for the fabrication of ferroelectric films owing to its precise stoichiometry control, high purity, coating uniformity, and low manufacturing costs. Furthermore, the intimacy of mixing and high reactivity of the liquid constituents facilitates crystallization at temperatures several hundred degrees below those necessary in conventional mixed-oxide processing, which can enable direct on-chip integration with semiconductor devices.[42] For the purposes of this study, thick (> 1 μm) PZT films were prepared using a chemical solution deposition process. The complete film production sequence is shown in Figure 3.1.

3.2.1 Solution Preparation

The PZT solution utilized 2-methoxyethanol ($CH_3O(CH_2)_2OH$), (Aldrich Chemical Co., Milwaukee, WI), or 2-MOE, as the solvent.[43] Precursors were lead acetate trihydrate ($Pb(CH_3CO_2)_2 \cdot 3H_2O$), zirconium n-propoxide ($Zr[O(CH_2)_2CH_3]_4$), and titanium iso-propoxide ($Ti[OCH(CH_3)_2]_4$) (Aldrich Chemical Co., Milwaukee, WI). The

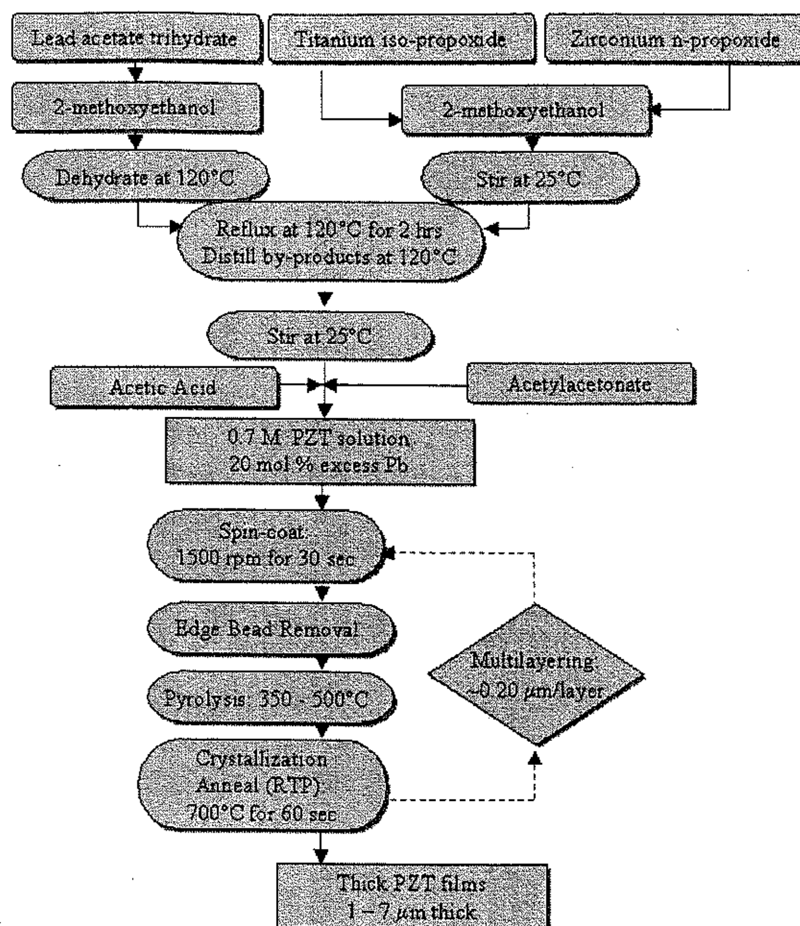

Figure 3.1 Chemical solution spin-on process flow for PZT films prepared in this investigation.

procedure used was a modification of that first introduced by Budd, Dey, and Payne[44] for processing of PZT films ≤ 2.5 μm-thick.

Initially, lead acetate trihydrate was added to 2-MOE in a rotary evaporator flask under Ar. To facilitate dissolution, the flask was lowered into an oil bath heated to 70°C on a hot plate and the temperature of the bath was gradually increased to 120°C. The solution was then dehydrated under vacuum until a semi-dry powder remained. A mixture of zirconium n-propoxide and titanium iso-propoxide in 2-MOE at room temperature was added and the entire solution was refluxed for 2 h under Ar at 120°C.

After refluxing, the solution was vacuum distilled and 2-MOE was added until the desired solution molarity was achieved. Following modification with both acetylacetonate (20 vol%) and acetic acid (5 vol%), the solution was 0.70 M with 20 mol% Pb in excess of stoichiometry to compensate for high Pb volatility.[45]

3.2.2 Spin Coating

Many of the substrates used in this study were commercially manufactured 375 μm Si/10,000 Å SiO_2/200 Å Ti/1500 Å Pt (Nova Electronic Materials, Inc., Richardson, TX). The Pt film was primarily (111)-oriented. Substrates were preannealed at 500°C for 60 s. Spin coating was used to apply a uniform layer of solution on the surface of the substrate. Solutions were dispensed through a syringe with a 0.1 μm Whatman filter (Aldrich Chemical Co., Milwaukee, WI) and the substrate was spun at 1500 rpm for 30 s using a PWM32 photoresist spinner (Headway Research, Inc., Garland, TX). Following each spin-coated layer, films were subjected to a series of heat treatments to drive off organic, densify, and crystallize the film. The first and second pyrolysis steps, each 60 s in duration, were performed using a hot plate at 350°C and 500°C, respectively. During the second treatment, a 1 mm–thick aluminum plate was positioned parallel to and ~3.5 mm above the film surface to enhance heating by convection. A crystallization anneal was performed for each layer in a Heatpulse 610 rapid thermal processing (RTP) unit (AG Associates, Sunnyvale, Ca) at 700°C for 60 s. The RTP anneal converted the film structure to polycrystalline perovskite with some degree of preferred orientation. Each sequence produced a layer approximately 0.20 μm in thickness and the sequence was repeated to obtain the desired film thickness. This method was used to prepare films of

varying thickness (2 μm, 4 μm, and 6 μm) with compositions spanning the morphotropic phase boundary (Zr/Ti ratios of 40/60, 45/55, 52/48, and 60/40).

3.2.3 Edge Bead Removal

It was discovered that for films thicker than 4 μm, cracking often occurred. These cracks originated at the film edge and radiated toward the center of the substrate. Edge bead removal was employed to prevent cracking and achieve thicker films. This technique is commonly used in silicon processing for the spinning of photoresist. During the spinning process, an edge bead of dried solution, several times thicker than the film, can build up.[18] The greater the layer thickness, the higher the tendency for cracking during rapid shrinkage associated with the pyrolysis steps. As a result, the edge bead is more susceptible to cracking than the remainder of the film.

Immediately following each spin-coating, a cotton-tipped applicator was moistened with 2-MOE and carefully run along the edge of the substrate. This removed a ~2 mm ring of solution at the outer edge, leaving the underlying Pt visible. Using this technique, crack-free films of thickness >7 μm were achieved.

3.3 Structural Characterization

It is well known that the structure of materials, both on a macroscopic and microscopic level, has a marked effect on their properties. This is particularly important in PZT films where structural features can significantly impact domain wall mobility and therefore extrinsic contributions to dielectric, piezoelectric, and ferroelectric properties. The goals of this characterization were to determine film orientation, crystal structure,

grain size and shape, and thickness in order to correlate these structural characteristics to measured properties.

3.3.1 X-Ray Diffraction (XRD)

Orientation and crystal structure of the PZT films were determined using a Scintag x-ray diffractometer (Scintag, Inc., Sunnyvale, CA). Ni-filtered Cu $K\alpha$ radiation was used and x-ray diffraction data were collected between 20° and 60° 2θ at a rate of 2° 2θ/min.

3.3.2 Scanning Electron Microscopy (SEM)

Microstructural features of the films were examined using an S-3500N scanning electron microscope (Hitachi Ltd., Tokyo, Japan). SEM analysis provided both surface and cross-sectional topographical information including grain size and shape. The surface of each film was etched by submerging the entire sample in a dilute HF/HCl solution for ~3 s and immediately rinsing with deionized water. Because films etch more rapidly along grain boundaries, this etching step was performed to reveal the surface morphology. Samples were first sputter-coated with a thin Au film to increase electrical conductivity at the surface and prevent charging that tends to decrease image clarity.

3.3.3 Surface Profilometry

Measurements of film thickness were made using an Alpha-Step 500 surface profilometer (Tencor Instruments, Inc., Mountain View, CA) with Å resolution. In this measurement, a sensitive stylus, in light mechanical contact with the sample surface,

travels over a distance of 500 μm at a rate of 50 μm/s. By positioning the stylus such that it would run across a step between the exposed bottom Pt electrode and PZT film, the film thickness was determined by the vertical displacement of the stylus.

3.4 High and Low Field Electrical Characterization

The aims of this section were to characterize both high and low field dielectric and ferroelectric properties of the PZT films. The properties of interest included relative permittivity, dielectric loss tangent, remanent polarization, and coercive field.

3.4.1 Electrical Contacts

To enable electrical characterization, Pt/PZT/Pt capacitors were fabricated. For characterization purposes, platinum top electrodes were deposited using a SCD 050 sputter coater (BAL-TEC AG, Germany) through a mechanical mask at a base pressure of 0.05–0.1 mbar. Electrodes were circular with a diameter of 1.5 mm and a thickness of approximately 1500 Å. Following deposition, a 5 min hot plate anneal at 500°C was used to improve the quality of the film/top electrode interface. In some cases, wire leads were attached to the Pt electrodes using CW2400 conductive epoxy (Chemtronics, Kennesaw, GA), which required high temperature curing (~10 min at 120°C).

3.4.2 PZT Film Patterning

In order to make electrical contact with the bottom Pt electrode, it was necessary to pattern the PZT film. For films ≤2 μm-thick, patterning was accomplished by defining

an area with Scotch™ tape (3M, St. Paul, MN) and etching with a dilute HF/HCl solution.

This method proved impractical for etching thicker films due to poor selectivity and a lithographic approach was taken. The two-step wet etching process for PZT thick films has been previously reported.[19] A small rectangular piece of Scotch™ tape was used as a mask in the lithography step. The area of the PZT film defined by the tape represented the area that would later be etched. The etching sequence is shown in Table 3.1.

Table 3.1 Two-step wet etching process for thick PZT films used to expose the bottom electrode.

Step	*Description*	*Details*	*Function*
1	Dehydration bake	115°C, ~10 min	H_2O removal
2	Scotch™ tape application	--	Mechanical masking
3	HMDS* spin coat	3000 rpm, 15 s	Enhance film/photoresist adhesion
4	Shipley 1813 photoresist spin coat	3000 rpm, 40 s	Protect film surface during etch
5	Scotch™ tape removal	--	--
6	Hard-bake	115°C, 3 min	Residual solvent removal
7	10 H_2O:1 BOE$ etch	~0.1 μm/min	PZT film etching (1st step)
8	2 HCl:1 H_2O etch	1-3 min	Residue removal (2nd step)
9	Acetone rinse	~15 min	Photoresist removal

* HMDS – hexamethyldisilazane is a popular adhesion promoter in IC processing.[18]

$ BOE – buffered oxide etch ($10HN_4F$:1 HF).

3.4.3 Electrode Probing

For electrical measurements, joystick micropositioners (Signatone Corp., Gilroy, CA) were employed to probe capacitor electrodes. Two methods were used to contact Pt electrodes (shown schematically in Figure 3.2):

(a) Probe tip pressure contact to electrode

(b) Alligator clip contact to aforementioned wire leads

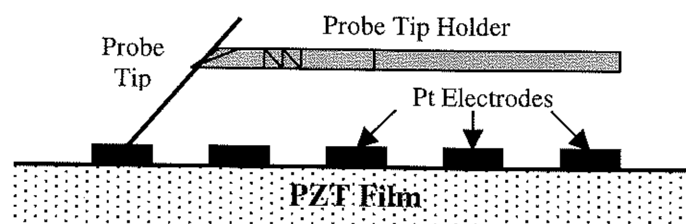

(a)

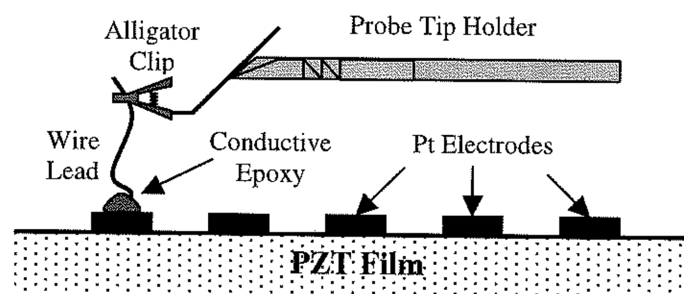

(b)

Figure 3.2 Pt electrodes were contacted in two ways: (a) probe tip pressure contact and (b) alligator clip contact to epoxied wire leads.

3.4.4 Low Field Characterization

Low field measurements of capacitance (used to determine relative permittivity) and dielectric loss tangent of the PZT films were made using a 4192A LF impedance analyzer (Hewlett-Packard, Palo Alto, CA). Unless otherwise indicated, all were carried out at a frequency of 1 kHz and oscillation voltage of 30 mV_{rms}.

3.4.5 High Field Characterization

Polarization-electric field hysteresis behavior of the PZT films was measured using an RT66A standardized ferroelectric test system (Radiant Technologies, Albuquerque, NM) in the virtual ground testing mode. Samples were measured using the "slow" mode (1.1 ms per point) at a peak field of ~300 kV/cm with 200 discrete voltage steps.

3.4.6 Temperature Dependent Characterization

Measurements of capacitance and dielectric loss tangent were carried out using a computer-automated system with a -73°C to 315°C temperature range using a 4284A precision LCR meter (Hewlett-Packard, Palo Alto, CA). Multiple spring-loaded sample holders mounted to the inside of the door of a 9023 environmental test chamber (Delta Design, Inc., Poway, CA) allowed characterization of as many as 8 film samples in a single run.

This same oven and sample holder were used in measuring P-E hysteresis loops as a function of temperature with the LCR meter replaced by the ferroelectric test system described in the previous section.

3.5 MEMS Accelerometers

As part of this investigation thick PZT films were deposited for use as the active piezoelectric sensing elements in a novel MEMS accelerometer. The design was innovative in that it utilized a novel annular sensing structure (designed by Kan Deng of Wilcoxon Research, Inc., Gaithersburg, MD) and combined PZT films and the silicon

bulk micromachining technique of deep-trench reactive ion etching (DRIE).[46] Details on the accelerometer design and fabrication are given elsewhere.[19]

Chemical solution-derived PZT films with Zr/Ti ratios of 52/48 and 5–6 μm thickness were used in the MEMS devices. A thickness near the upper limit for chemical solution processing was chosen because (1) piezoelectric coefficients increase with increasing film thickness[47] and (2) thicker films generate lower sensor capacitance, which was desirable for integration with the ASIC circuit chosen by Wilcoxon Research, Inc.

The next section briefly describes design, fabrication, and testing procedures associated with the MEMS accelerometer.

3.5.1 Design

As mentioned previously, the sensor design incorporates a novel circular diaphragm sensing structure. The device is intended to have a high resonance frequency (≥20 kHz) and large sensitivity (≥1.0 pC/g) in a mm-sized package. In this design, a thin annular diaphragm is supported at its edge by a rigid Si frame. The bottom electrode, thick PZT film, and top electrode are patterned on the top surface of the Si diaphragm and a proof mass is suspended at the center to enhance device sensitivity. The device is shown in cross-section in Figure 3.3. In response to an acceleration, strain is transferred from the Si diaphragm to the PZT film and charge develops on the electrodes by the direct piezoelectric effect. The amount of charge generated for a given strain is governed by the effective transverse piezoelectric coefficient ($e_{31,f}$) of the film.

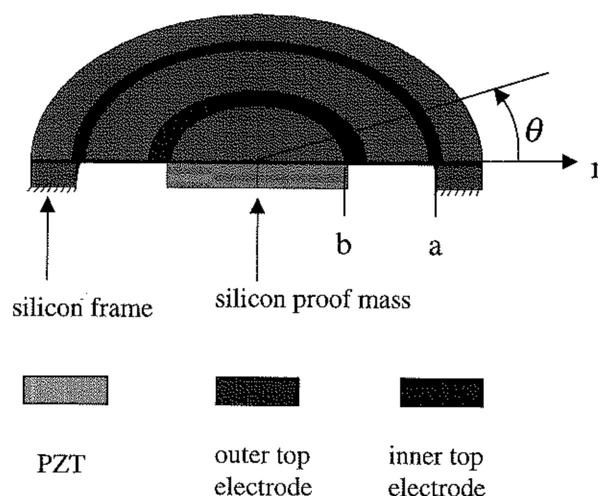

Figure 3.3 Cross-sectional view of circular diaphragm sensing structure of MEMS accelerometer (courtesy of Wilcoxon Research, Inc.).

It should be clear from Figure 3.3 that the structure is fully symmetric and transverse accelerations will not be detected. In response to a force normal to the plane of the device, the diaphragm is subjected to both radial and tangential stresses, σ_r and σ_θ, respectively, and these are responsible for the charge developed in the piezoelectric film. The stresses shift from compressive near the proof mass to tensile near the support frame. Stress is plotted in Figure 3.4 as a function of position along the radius of the diaphragm.

With this stress distribution in mind, the structure was designed with two annular top electrodes positioned at the inner and outer areas of the diaphragm where the stresses are greatest. These could then be poled in opposite directions (through the film thickness) to avoid charge cancellation. In addition, the top electrodes were designed with equal areas. This should give a cancellation of temperature-related (pyroelectric)

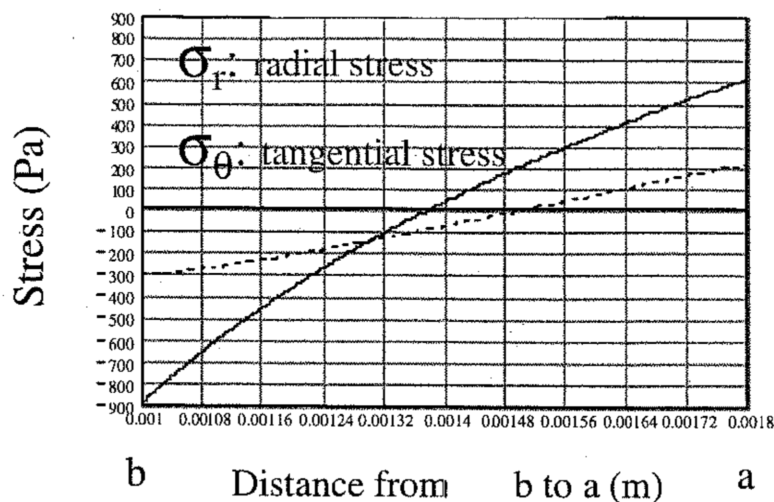

Figure 3.4 Radial and tangential stresses as a function of radial position along the annular diaphragm. σ_r and σ_θ correspond to the solid and dashed lines, respectively.

charge output when connected in parallel. Accelerometers were designed with a footprint of 6 mm × 6 mm.

3.5.2 Fabrication

The complete fabrication process for an earlier trampoline-type structure is illustrated in Figure 3.5 and is very similar to that used in fabrication of the annular devices. The detailed procedure has been reported.[19] 5–6 μm thick PZT 52/48 films were initially deposited on 4" (100 mm) platinized Si wafers using the chemical solution process detailed in section 3.2. The entire process involved five photomask levels and included a front-to-backside alignment, which was done using a mechanical jig with <25 μm accuracy.[19]

1) 4" SiO_2/Si/SiO_2/Ti/Pt/PZT/Cr/Au wafer

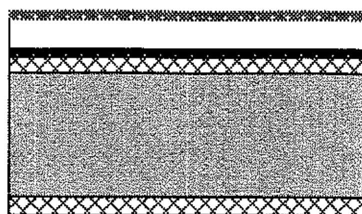

2) Front-to-backside alignment photolithography

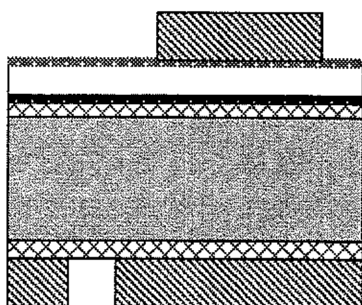

3) Cr/Au top electrode etched

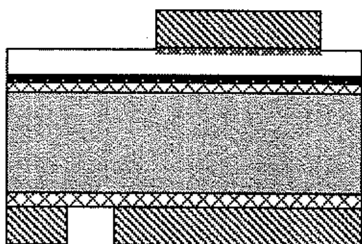

4) Backside SiO_2 etched using CF_4 and O_2 plasma

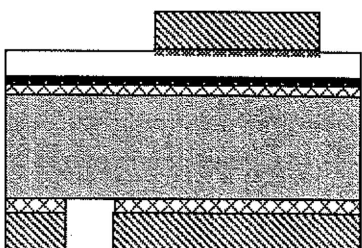

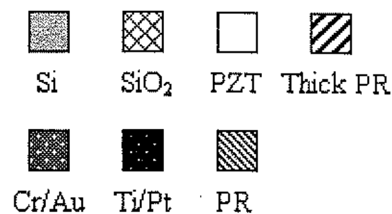

5) Thick PZT film was etched with the backside coated with photoresist

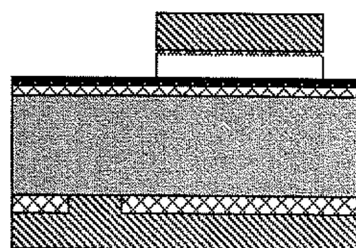

6) Ti/Pt bottom electrode etched using RIE (Cl_2 plasma); thick photoresist was used to achieve better step coverage

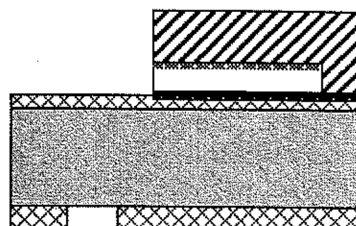

Figure 3.5 Fabrication process flow for MEMS accelerometer structure.[19] The two step DRIE sequence shown was used for through-etched parts. In the annular-type device, the entire backside of the structure was protected in step (7), and the annulus was exposed and etched during step (8).

7) 1st deep trench reactive ion etching (DRIE) step defined the beam thickness

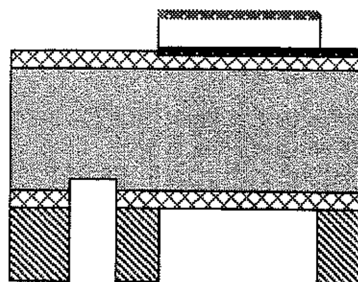

8) Following the HF backside oxide etch, the 2nd DRIE step released the beams

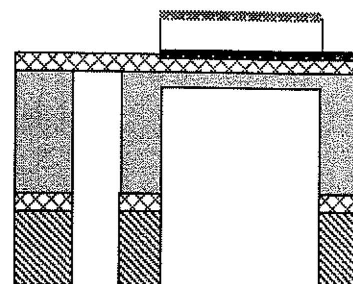

9) Frontside oxide was etched and photoresist stripped

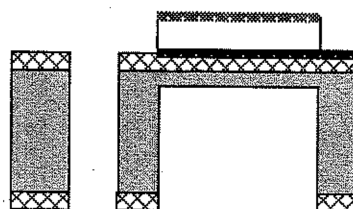

Figure 3.5 MEMS accelerometer fabrication process flow (continued).[19]

3.5.3 Testing

The frequency response and impedance resonance of the MEMS accelerometers were tested in this investigation. Measured results were compared both with those from finite element analysis (FEA) and with those measured independently at Wilcoxon Research, Inc.

3.5.3.1 Frequency Response Measurement

The frequency response measurement setup was assembled in-house and is shown schematically in Figure 3.6. Details of the setup can be found elsewhere.[19] The system consisted of a model F3 electromagnetic shaker (Wilcoxon Research, Inc., Gaithersburg, MD), a 3562A dynamic signal analyzer (Hewlett-Packard, Palo Alto, CA), and a

monoblock amplifier (AudioSource, Portland, OR). To circumvent difficulty in measuring the exact force applied to the MEMS chip during measurement, a model 736 high frequency accelerometer (Wilcoxon Research, Inc., Gaithersburg, MD) of known sensitivity (100 mV/g) was mounted to the shaker stage along with the MEMS chip. This enabled determination of the MEMS accelerometer sensitivity through a comparison of outputs from both devices.

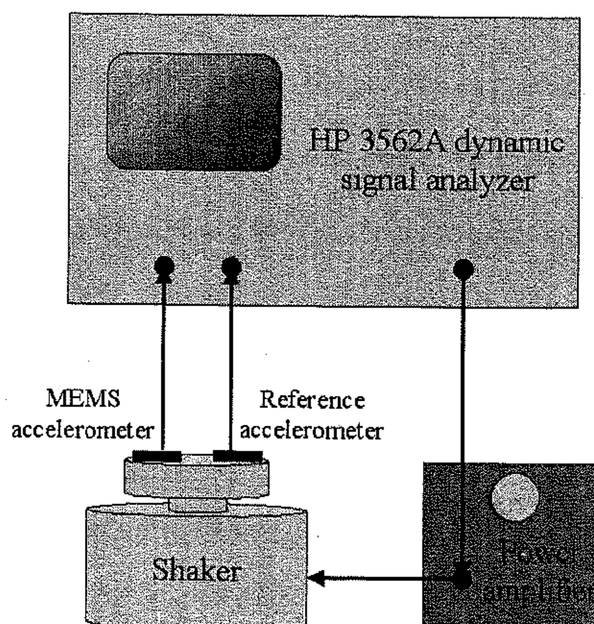

Figure 3.6 Frequency response measurement system.

3.5.3.2 Impedance Resonance Measurement

A 4194A impedance/gain-phase analyzer (Hewlett-Packard, Palo Alto, CA) was used to measure the impedance characteristics of the MEMS accelerometers as a function of frequency. Devices were excited with an oscillation voltage of 30 mV (no DC offset).

3.6 Modified Wafer Flexure Technique for Measurement of the Effective Transverse Piezoelectric Coefficient $e_{31,f}$ and its Variation with Temperature

For MEMS sensor and actuator applications, knowledge of the temperature dependence of the electromechanical properties of films is desired since devices are intended to operate within certain temperature limits. The wafer flexure technique was modified to characterize the $e_{31,f}$ piezoelectric coefficient of films as a function of temperature between -55°C and 85°C. Prior to piezoelectric characterization, films were poled at ~3E_c for 20 min. Films were then aged at room temperature for at least 72 hrs to ensure that the temperature dependence of the piezoelectric response could be separated from piezoelectric aging. Measurement details, temperature modification details, and validations of the technique will be discussed in the following sections.

3.6.1 Wafer Flexure Technique

This section describes the operating principle, strain analysis, uniform pressure rig, and peripheral electronics associated with the wafer flexure technique. Additional details have been reported elsewhere.[3] The only notable modification was the addition of a charge amplifier, which will be discussed later.

3.6.1.1 Principle of Operation

The wafer flexure technique is used to determine the direct $e_{31,f}$ coefficient of a film by placing it in an oscillating state of biaxial strain and measuring the output charge developed across it thickness. Equation 3.1 governs this behavior.

$$D_3 = \frac{Q_3}{A} = e_{31,f}(x_1 + x_2) \tag{3.1}$$

D_3 is the dielectric displacement (C/m^2) in the film thickness direction, Q_3 is the charge (C), A is the electrode area (m^2), and x_1 and x_2 are the principal in-plane strains. In the case of a circular plate, x_1 and x_2 correspond to planar radial and tangential strains, x_r and x_θ.

A periodic strain in the film produces current through the direct piezoelectric effect and this current is monitored. Charge is obtained from the root mean square current (i_{rms}) through Equation 3.2.

$$Q_3 = \frac{i_{rms}}{2\pi f} \tag{3.2}$$

f is the strain oscillation frequency (4 Hz was used throughout).

The room temperature measurement setup is shown schematically in Figure 3.7. Each of the main components will be described later.

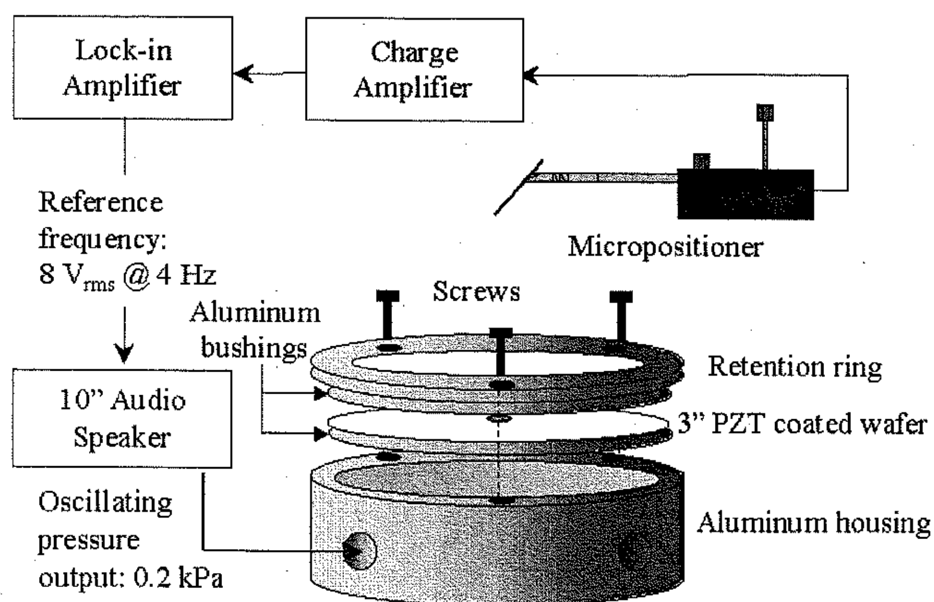

Figure 3.7 Room temperature wafer flexure measurement setup.

3.6.1.2 Theoretical Calculations of Film Strain

In the wafer flexure technique, film strain is achieved by driving air into a cavity below a film-coated wafer that is clamped about a given support radius. In this configuration, bending stresses in the wafer can be calculated for a given cavity pressure using small deflection plate theory.[48] The principal in-plane stresses at any position on the plate are given by Equations 3.3 and 3.4.

$$\sigma_r = \frac{3pz}{4t_{Si}^3}[(1+\nu_{Si})a^2 - (3+\nu_{Si})r^2] \tag{3.3}$$

$$\sigma_\theta = \frac{3pz}{4t_{Si}^3}[(1+\nu_{Si})a^2 - (1+3\nu_{Si})r^2] \tag{3.4}$$

σ_r and σ_θ are the radial and tangential stresses in the Si plate (N/m^2), p is the cavity pressure (N/m^2), z is the distance from its neutral axis (m), t_{Si} is the plate thickness, ν_{Si} is Poisson's ratio of Si, a is the support radius (m), and r is the distance from the center of the plate (m).

Complete transfer of strain from the Si substrate to the PZT film is assumed (i.e. $x_r^{Si} = x_r^{PZT}$ and $x_\theta^{Si} = x_\theta^{PZT}$) such that generalized Hooke's law, along with the elastic constants of Si, can be used to determine film strains from the known stresses in the Si substrate (Equations 3.5 and 3.6).

$$x_r = \frac{\sigma_{r,Si}}{Y_{Si}} - \nu_{Si}\left(\frac{\sigma_{\theta,Si}}{Y_{Si}}\right) \tag{3.5}$$

$$x_\theta = \frac{\sigma_{\theta,Si}}{Y_{Si}} - \nu_{Si}\left(\frac{\sigma_{r,Si}}{Y_{Si}}\right) \tag{3.6}$$

x_r and x_θ are the radial and tangential strains, respectively, and Y_{Si} is Young's modulus of Si.

Small deflection plate theory is applicable to the case of a film-coated substrate provided that (1) the thickness of the film is much smaller than that of the substrate such that deformation is dominated by the elastic properties of the substrate and (2) the maximum deflection of the coated substrate does not exceed 20% of its thickness such that membrane stresses can be ignored.[48] The first requirement is fulfilled in that the thickness ratio between the PZT film (≤ 6 μm) and Si wafer (375 μm) was less than 2%. The second was easily satisfied by selecting a suitable cavity pressure (0.2 kPa).

In stress and strain calculations, the <100> single crystal Si wafer was treated as an isotropic plate and the averages of maximum and minimum in-plane elastic constants (along <100> and <111>directions) were used.[3] These values are tabulated in Table 3.2.

Table 3.2 Elastic constants of Si used in this investigation. The Si wafer was treated as an isotropic plate.[49]

Elastic Property	***Value***
Young's modulus	150 GPa
Poisson's ratio	0.172

3.6.1.3 Uniform Pressure Rig

The uniform pressure rig consists of an aluminum housing, removable bushings, a retention ring, and 3 stainless steel screws. The film-coated wafer is carefully positioned between the bushings and secured with screws that run through the retention ring and into the housing (outside the outer radius of the wafer and bushings). This clamps the wafer such that an oscillating pressure can be fed into the underlying cavity to create periodic wafer flexure.

The unit used in this investigation was designed to accommodate 3"-diameter (76 mm) wafers. For room temperature characterization, aluminum bushings were polished to 5 μm using successively finer grit SiC paper. This was done to minimize creation of defects in the substrate and improve the pressure seal. Clamping was achieved by tightening the screws in 0.5 in-lb increments to a final torque of 1.5 in-lbs.

3.6.1.4 Peripheral Electronics

Peripheral electronics included:

- 7260 DSP lock-in amplifier (EG&G Instruments, United Kingdom)
- hk770 twin toroidal power ultrawideband DC amplifier (Harman Kardon, Northridge, CA)
- 10" audio speaker (Zenith Electronics Corp., Lincolnshire, IL)

The lock-in amplifier served two important functions during measurement. First, it provided a reference signal of 0.5 V_{rms} at 4 Hz, which was then amplified by the stereo amplifier (16X) and used to drive the audio speaker. The pressure created by the speaker was fed into the cavity through a plastic hose. The other role of the lock-in amplifier was to monitor the output voltage from the charge amplifier. This voltage was used to determine the current output from the film as it was strained.

3.6.1.5 Charge Amplifier

Because charge output from the 1.5 mm-diameter electrodes was small (~1 nF), a charge amplifier was employed for signal amplification. The circuit diagram for this

device is shown in Figure 3.8. The input charge (Q_{IN}) was amplified and converted to a voltage (V_{OUT}) through Equation 3.7.

$$V_{OUT} = \frac{Q_{IN}}{C} \tag{3.7}$$

For this work, a 1 nF capacitor was chosen such that voltage output was ~10 mV and could be displayed easily using an oscilloscope. In addition, the amplifier was designed such that the film was maintained at virtual ground (to within ±3 mV).

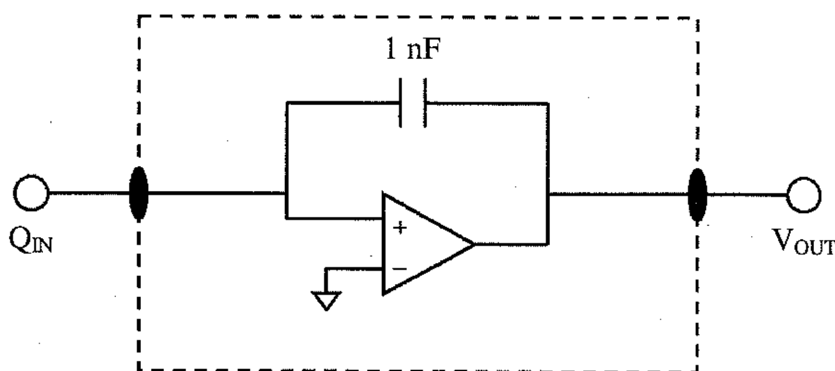

Figure 3.8 Simplified circuit diagram of charge amplifier.

3.6.2 Temperature Control Modifications

The temperature specification for the aforementioned MEMS accelerometer is -55°C to 85°C and consequently, the investigation focused on this particular range. The following sections outline the way in which the room temperature wafer flexure technique was adapted to enable temperature-variable measurement.

3.6.2.1 High Temperature Modification

Resistive heaters were used to heat the aluminum housing. A thermocouple (type K) was held in contact with the wafer surface using Kapton® polyimide tape (DuPont,

Wilmington, DE). The thermocouple and resistive heaters were wired to a CN9000A miniature autotune temperature controller (Omega Engineering, Inc., Stamford, CT) which displayed and regulated the temperature of the wafer to ±0.1°C.

Heat was efficiently transferred from the housing to the wafer as indicated by differential thermocouple measurements. One fixed (inserted into the housing) and one movable thermocouple (set at different radial positions on the wafer surface) were used to measure the temperature uniformity across the wafer and the efficiency of heat transfer. With the housing held at 125°C, there was a ±4°C temperature uniformity across the wafer (Figure 3.9). It is expected that uniformity was even better during piezoelectric measurements, where a maximum temperature of only 85°C was used. It should be noted that a thin layer of thermal joint compound (described in detail in section 3.6.2.3) enhanced heat transfer.

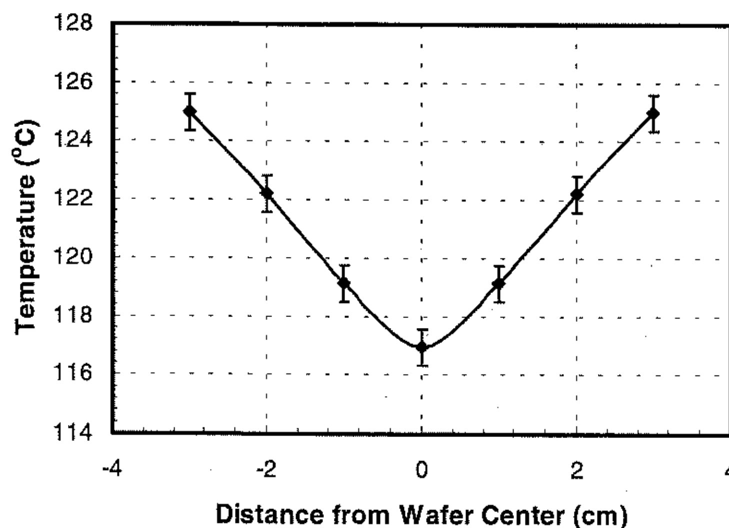

Figure 3.9 Measured temperature profile across a 3" wafer with the aluminum housing heated to 125°C. The maximum temperature used in subsequent experiments was 85°C.

3.6.2.2 Low Temperature Modification

For measurements below room temperature, the pressure rig and microprobes were placed inside an in-house-constructed liquid nitrogen-cooled enclosure insulated with 3/4"–thick Styrofoam sheathing. A 30 L liquid-nitrogen dewar was pressurized to ~5 psi with a tank of dry UHP (ultra-high purity) nitrogen and a copper pipe was fed from the dewar into the chamber. A manual flow control valve was used to regulate the flow of nitrogen. This setup is shown schematically in Figure 3.10.

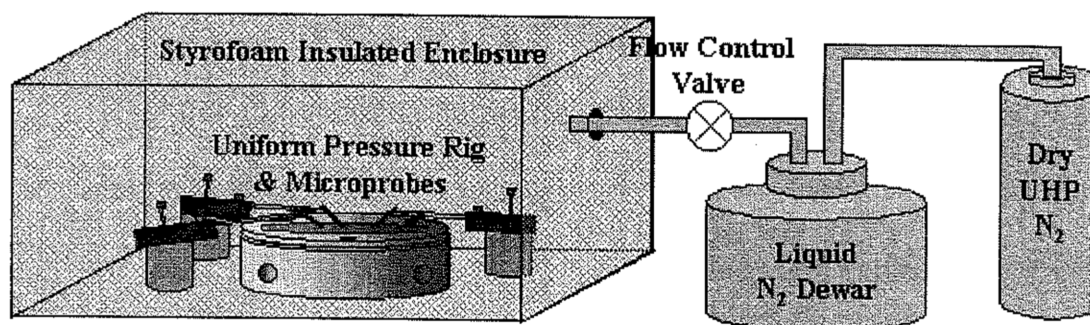

Figure 3.10 Low temperature wafer flexure measurement setup.

The chamber temperature was continuously monitored using an RTD (Pt100). The minimum attainable temperature within the enclosure was approximately -190°C and rapid cooling rates were possible (>15°C/min).

Moisture condensation (and subsequent ice formation) was significantly reduced by maintaining the wafer at least 10°C above the chamber temperature using the resistive heating system outlined in the previous section.

3.6.2.3 Wafer Clamping Modification

There is a significant difference in thermal expansion characteristics between the substrate and pressure rig materials ($\alpha_{TCE,Si}$ = 2.6 ppm/°C and $\alpha_{TCE,Al}$ = 23 ppm/°C). As a result, changes in temperature give rise to static stresses that either stretch or compress the wafer within the plane. This can complicate the measurement of $e_{31,f}$ with temperature by wafer flexure by introducing a stress dependence, which is difficult to separate from the temperature dependence. To minimize these types of static stresses, a different clamping condition was employed in all temperature-variable measurements. A thin layer of Thermalcote thermal joint compound (Thermalloy, Inc., Dallas, TX) was applied to the entire contact area between the wafer and the aluminum bushings. The viscosity of the thermal joint compound alone was sufficient to maintain a pressure seal with the lower bushing to well above a 0.2 kPa oscillating cavity pressure. In addition, no torque was imparted to the screws as they were used only to loosely secure the wafer between the bushings (they were hand-tightened until snug). These modifications (thermal joint compound at substrate/bushing contacts and screws loosened) at least partially relieved thermal expansion mismatch-related static stresses by allowing the wafer to expand/contract in-plane with respect to the pressure rig.

This type of configuration changed the clamping boundary conditions, and the film strain calculation by small deflection plate theory was no longer straightforward. The new configuration was intermediate between uniform loading of a circular plate with clamped edge and one with a simply supported edge. These two situations are illustrated in Figure 3.11.

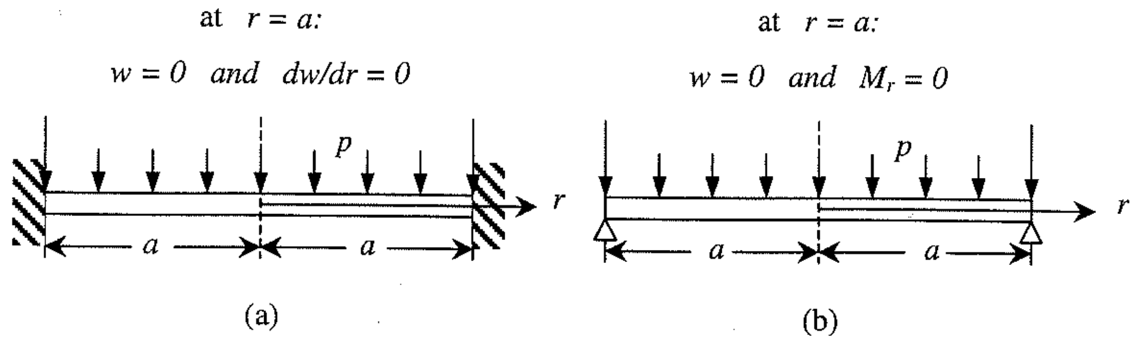

Figure 3.11 Uniformly loaded circular plate with (a) clamped edge and (b) simply supported edge. Boundary conditions are given above. r is radial position (m), a is support radius (m), p is pressure (N/m^2), w is deflection (m), and M_r is the radial bending moment (N·m).

Equations for calculation of in-plane stresses in the plate for the fully clamped situation have been given (Equations 3.3 and 3.4). In the simply supported case, these stresses are given by Equations 3.8 and 3.9.

$$\sigma_r = \frac{3pz}{4t_{Si}^3}(3+\nu_{Si})(a^2 - r^2) \tag{3.8}$$

$$\sigma_\theta = \frac{3pz}{4t_{Si}^3}[(3+\nu_{Si})a^2 - (1+3\nu_{Si})r^2] \tag{3.9}$$

The principal in-plane stresses for both situations are shown in Figure 3.12. It is seen that changing from a simply supported condition to a fully clamped one shifts the zero stress baseline upward on the stress axis by $\frac{3}{4}\frac{pa^2}{t^2}$. In contrast to the fully clamped case where there is a change from tensile to compressive stress along the radius, the radial stress is tensile everywhere in the simply supported case. In the situation of intermediate clamping, such as that under discussion, this zero stress baseline is positioned somewhere between these two limits. Because the exact clamping condition

was unknown, a strain gage was used to measure strain during all experiments where the clamping modification was employed.

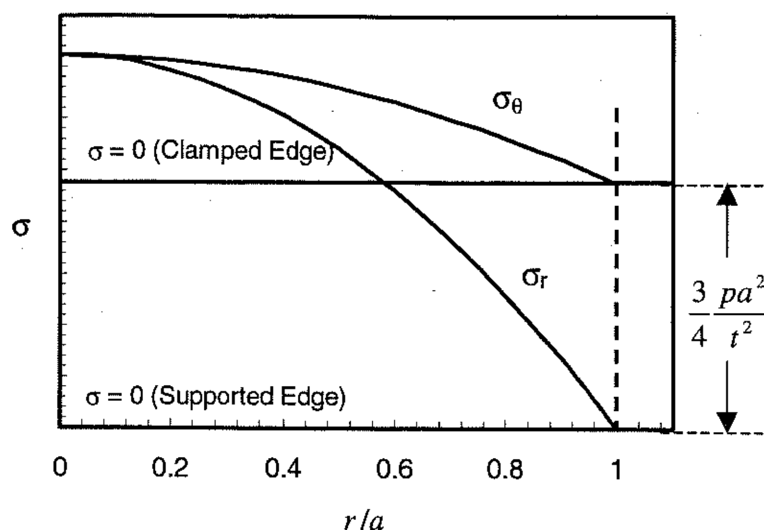

Figure 3.12 Stress variation with radial position for a uniformly loaded circular plate with clamped edge and simply supported edge. The zero stress baseline is shown for each case. The wafer clamping modification results in a condition intermediate between these extremes.

3.6.2.4 Strain Measurement

SG-2/350-LY11 foil strain gages (Omega Engineering, Inc., Stamford, CT) were used to measure strain, simultaneously with charge output, during temperature-variable $e_{31,f}$ measurements. These gages measured 2.0 mm × 1.8 mm and were bonded to the film surface using Instant Krazy Glue® cyanoacrylate adhesive (Elmer's Products, Inc., Columbus, OH). A quarter bridge circuit was used to ascertain the change in resistance of the gage during cavity pressure oscillation and is shown schematically in Figure 3.13. The 4 V DC excitation was provided by a PST-4130 regulated power supply (Omega Engineering, Inc., Stamford, CT).

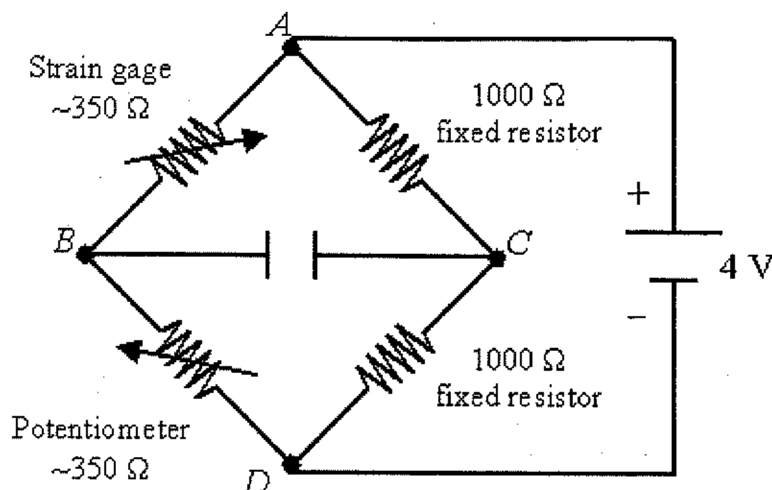

Figure 3.13 Schematic diagram of quarter bridge circuit used in strain measurements.

By adjusting the potentiometer, the bridge was initially balanced with the gage unstrained such that $V_B = V_C$. During measurement, the voltage difference between points *B* and *C* was monitored using a model SR830 DSP lock-in amplifier (Stanford Research Systems, Sunnyvale, CA), and was used to determine strain in the film for a given position and orientation.

A simple experiment was used to gauge our ability to duplicate clamping conditions after a sample had been unclamped. A strain gage was fixed 1.1 cm from the center of a film-coated wafer, the wafer was clamped between the bushings (only hand-tight with joint compound), and strain was measured with the oscillating speaker pressure applied. The wafer was then unclamped, rotated 60°, and the strain was measured as before. This was repeated until the wafer was rotated back to its original position (7 total measurements). This analysis revealed a uniformity of ±0.22 με (±7%) at 1.1 cm and room temperature.

3.6.2.5 Wafer Preparation

Simultaneous monitoring of strain, temperature, and piezoelectric current was required during temperature-variable $e_{31,f}$ measurements. The strain gage, thermocouple, and poled electrode should be closely spaced and accessible since both strain and temperature are functions of wafer position. To accommodate all of the measurements, it was assumed that strain and temperature were radially symmetric. As shown in Figure 3.14, the following were placed at a distance of 1.1 cm from the wafer center:

- Wire leads were attached to three distinct Pt top electrodes
- A strain gage was bonded in radial orientation
- A thermocouple was fixed with Kapton® tape

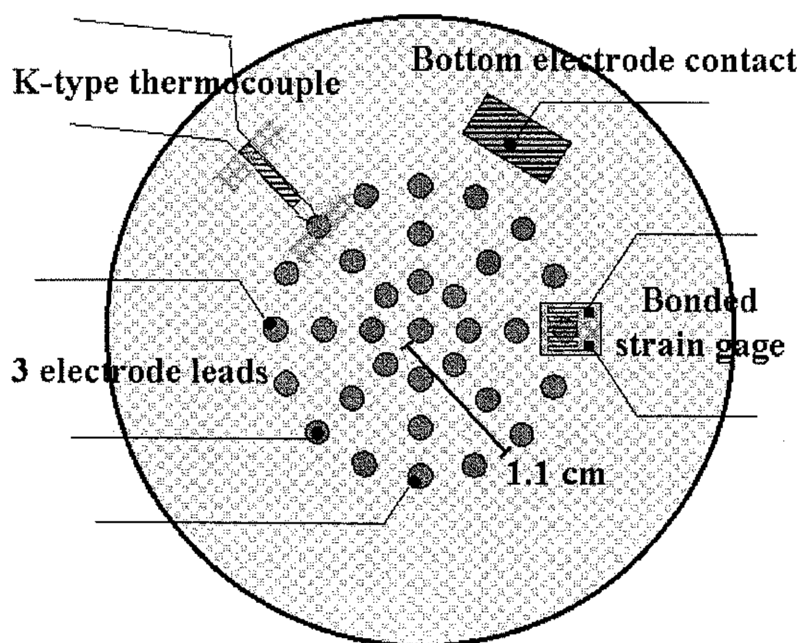

Figure 3.14 3" PZT-coated wafer preparation for modified wafer flexure measurement of $e_{31,f}$ with temperature (not to scale).

The three leaded electrodes were subsequently poled and films were allowed to age for at least three days at room temperature to minimize aging effects during measurement (at room temperature, piezoelectric constants in PZT films typically age at 5–10%/decade[50]).

It was stated previously that both radial and tangential strains are needed to calculate $e_{31,f}$ by the wafer flexure method (Equation 3.1). At a radius of 1.1 cm from the wafer center, these quantities are not equal. However, according to Figure 3.12, for a given clamping condition, the ratio of radial to tangential stress is constant.

To verify this experimentally, two strain gages were fixed at 1.1 cm from the center of a 3" PZT-coated wafer in radial and tangential orientations, respectively. The wafer was clamped in the pressure rig using the modified clamping condition and the output of each strain gage was monitored simultaneously as temperature was varied between -55°C and 85°C. The strain ratio x_θ / x_r remained essentially constant (±3%) at 1.27 throughout the measured temperature range. As a result of this calibration, it was assumed that the radial strain was directly proportional to the total strain ($x_r + x_\theta$). Because only relative changes in $e_{31,f}$ were of interest, measurements of the tangential strain were not done routinely.

Chapter 4 : Results and Discussion

4.1 Introduction

This chapter presents results related to the temperature dependent characterization of the effective transverse piezoelectric coefficient $e_{31,f}$ of PZT films using the modified wafer flexure technique. Thick films of varying thickness and Zr/Ti ratio were characterized to elucidate mechanisms responsible for the measured electromechanical properties. Dielectric, ferroelectric, and piezoelectric measurements were made as a function of temperature, and film microstructure, phase, and orientation were analyzed. In addition, measured characteristics of MEMS accelerometers are given and discussed.

4.2 Structural Characterization

Ten PZT films were analyzed in this chapter and all were prepared using the 2-methoxyethanol-based chemical solution deposition process outlined in section 3.2. They had thicknesses of 2 μm, 4 μm, or 6 μm and Zr/Ti ratios of 60/40, 52/48, 45/55, or 40/60.

4.2.1 X-Ray Diffraction Analysis

Figure 4.1 shows grazing angle XRD patterns for each film. Within the detection limits, the films were phase-pure perovskite (i.e. no pyrochlore phase was identified). Films were not strongly textured.

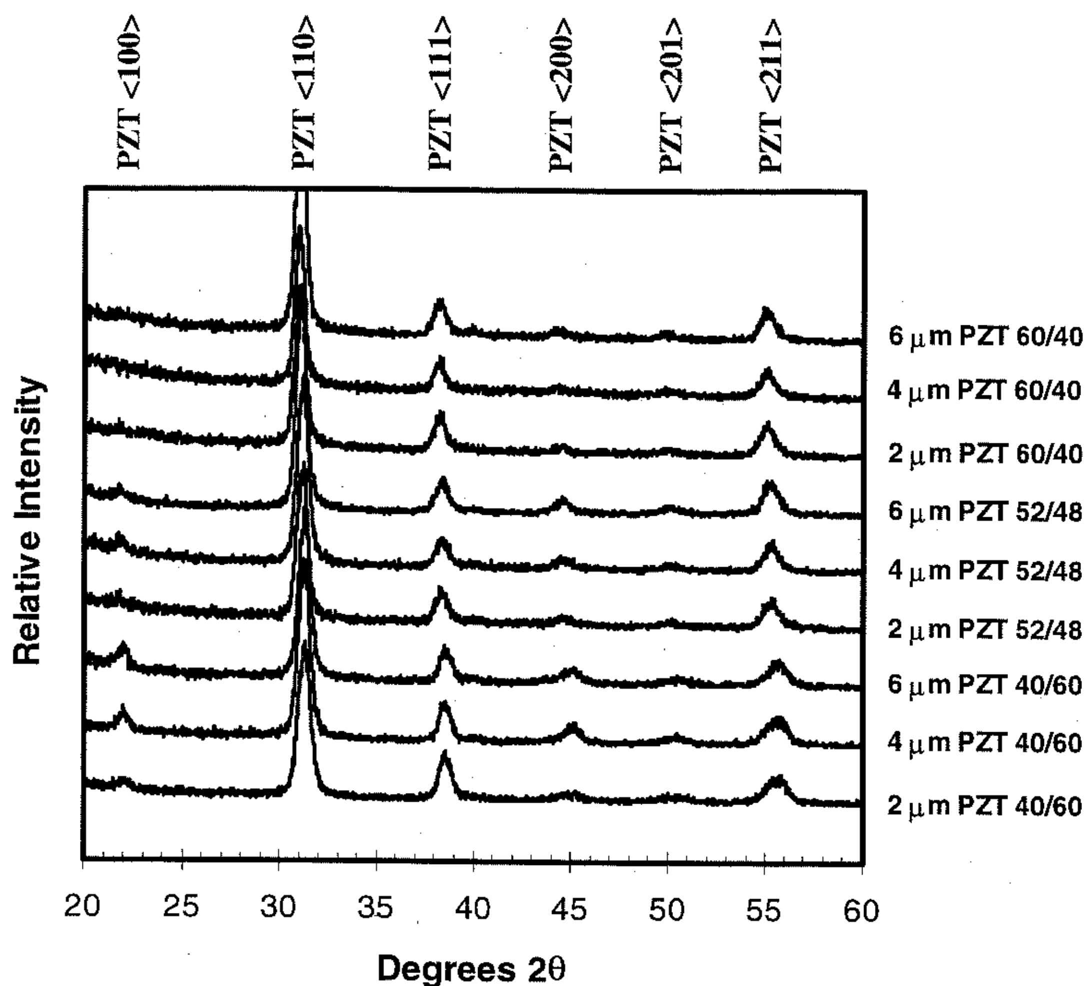

Figure 4.1 X-ray diffraction patterns of chemical solution deposited PZT films characterized in this study.

4.2.2 Atomic Force Microscopy Analysis

AFM was used to determine the average grain size of the films characterized in this study. Several films were analyzed and no significant change in grain size was observed as a function of thickness or composition. The surface grain size was found to be 150–200 nm. Figure 4.2 shows an image of the surface of a 2 μm PZT 40/60 film.

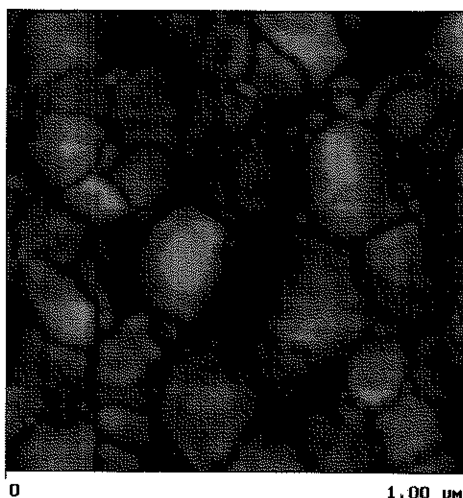

Figure 4.2 AFM image of the surface of a 2 µm PZT 40/60 film. Average grain size was 150–200 nm.

4.2.3 Scanning Electron Microscopy Analysis

SEM analysis was used to examine cross-sectional and near surface morphology. As seen in the cross-sectional micrograph of the 6 µm PZT 60/40 film (Figure 4.3a), a clear boundary is visible between each crystallized layer and layers appear to be one grain thick. Because each layer was crystallized separately in the RTA, it is likely that the top surface of each layer provided nucleation sites for the layer above it. An almost identical structure was seen in films of other thicknesses and Zr/Ti ratios. Also, the near surface investigation (Figure 4.3b) revealed an average grain size in agreement with that determined using AFM.

4.2.4 Surface Profilometry

The thickness of each film analyzed in this chapter was determined using a surface profilometer. Films were fabricated at each Zr/Ti ratio (60/40, 52/48, 45/55, and 40/60) and measured thicknesses are shown in Table 4.1.

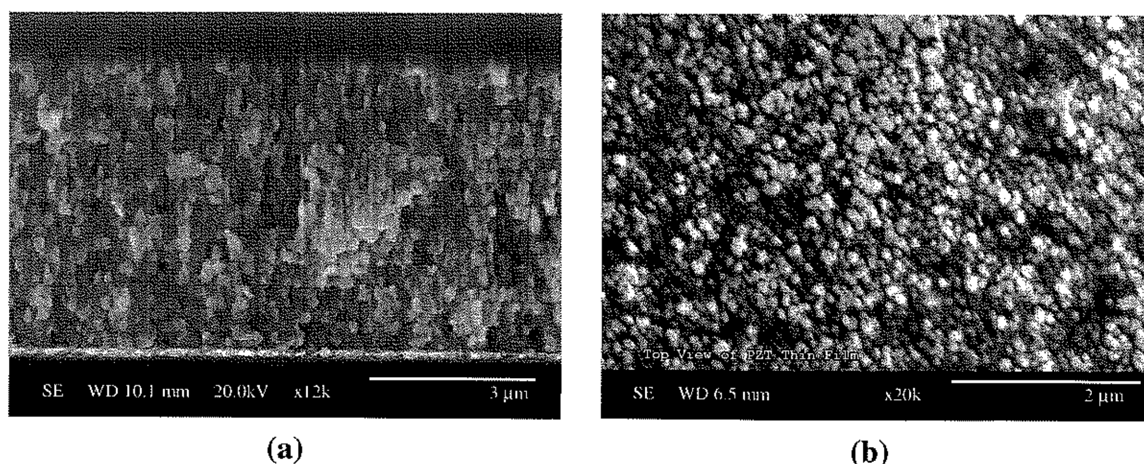

Figure 4.3 SEM micrographs of (a) cross-section of a 6 µm PZT 60/40 film and (b) near surface morphology of a 4 µm PZT 52/48 film.

Table 4.1 Measured thicknesses of ten PZT films characterized in this study.

Composition	*Thickness (µm) ± 0.03 µm*		
PZT 60/40	2.11	4.11	6.03
PZT 52/48	1.87	4.01	5.86
PZT 45/55	1.96	--	--
PZT 40/60	2.13	4.06	6.16

4.3 High and Low Field Electrical Characterization

4.3.1 Low Field Characterization

The dependence of the room temperature unpoled dielectric permittivity on PZT film thickness and composition is shown in Figure 4.4a. The observed Zr/Ti ratio dependence can be explained by intrinsic contributions, and it is useful to revisit Figure 2.14, which plots the phenomenologically-derived intrinsic permittivity as a function of temperature for each composition. At room temperature, the intrinsic relative

permittivities of 60/40 and 52/48 compositions are roughly equal and greater than that of the 40/60 composition (by several hundred). A similar relationship was seen in the measured values for films in Figure 4.4, although here extrinsic contributions (presumably 180° domain wall motion) are also included. Average values of relative permittivity were 908, 884, 784, and 653 for films with 60/40, 52/48, 45/55, and 40/60 ratios, respectively. All are accurate to ±10 or better. Note that the "average" value reported for the PZT 45/55 composition is simply the measured permittivity of the 2 μm film (784).

In the 60/40 and 52/48 compositions, the permittivity was found to increase with film thickness. Increased domain wall contributions,[51] a change in the substrate clamping, or the presence of lower dielectric constant interfacial or surface layers[29] are possible reasons for this apparent thickness dependence.

In all films, the measured dielectric loss tangent was ≤2.5% (Figure 4.4b). The maximum loss tangent occurred in the 52/48 composition, nearest to the MPB and there was no clear indication of a thickness dependence.

4.3.2 High Field Characterization

Figure 4.5 presents the results of the high field ferroelectric characterization performed at room temperature. Remanent polarization and coercive field values were extracted from P-E hysteresis data. Figure 4.6 shows P-E loops for all 6 μm PZT films. These relative loop shapes were similar in the 2 μm and 4 μm films as well, with loops becoming more square with increasing $PbTiO_3$ content. Results are consistent with the existing literature on PZT films.[52]

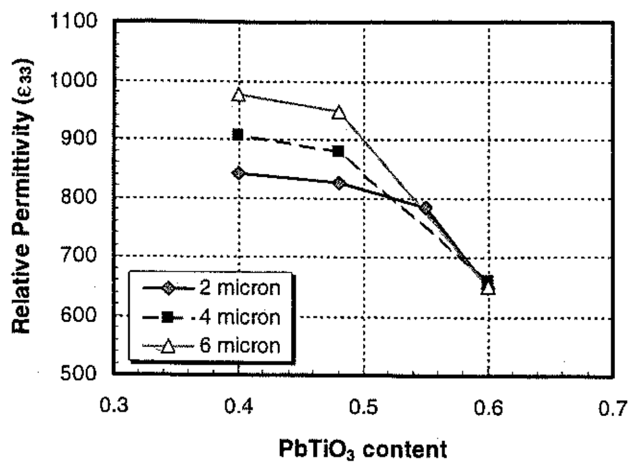

(a)

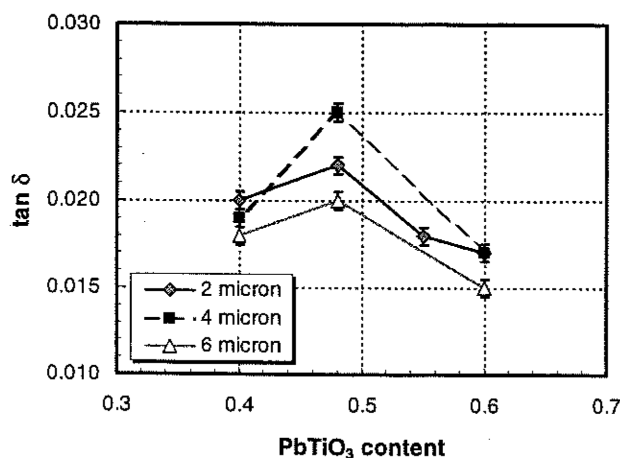

(b)

Figure 4.4 Plots of room temperature (a) relative permittivity and (b) loss tangent as a function of Zr/Ti ratio for 2 μm, 4 μm, and 6 μm PZT films. Error bars are nested within symbols in (a).

The highest and lowest measured values of remanent polarization occurred in the 6 μm PZT 52/48 (27.0 ± 1.0 $\mu C/cm^2$) and 2 μm PZT 40/60 films (19.4 ± 1.0 $\mu C/cm^2$), respectively. Coercive fields were found to be fairly independent of film thickness but appreciably dependent upon Zr/Ti ratio. E_c increased with $PbTiO_3$ content with average values of 33.6, 36.8, and 52.4 ± 0.4 kV/cm for films with 60/40, 52/48, and 40/60 Zr/Ti ratios, respectively.

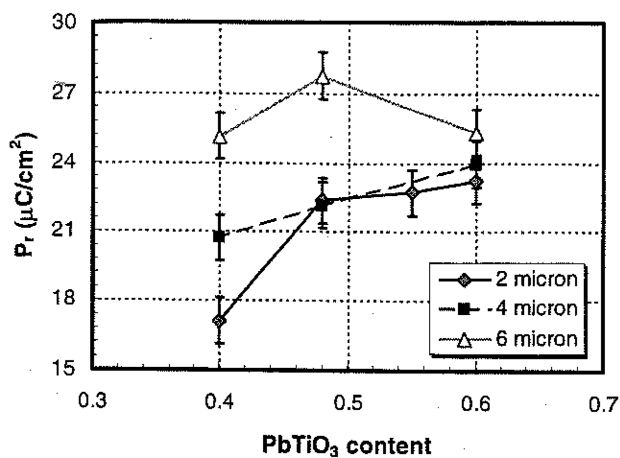

(a)

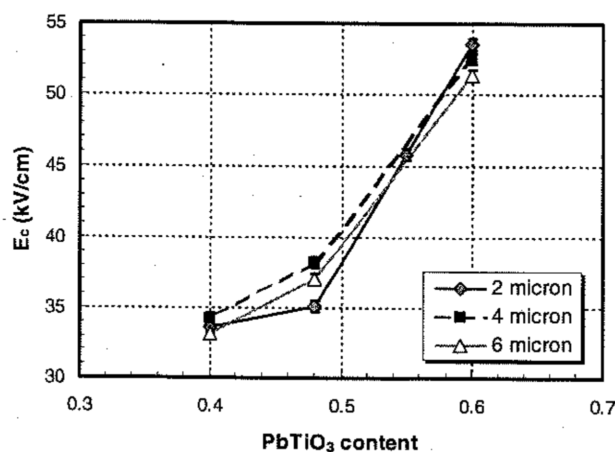

(b)

Figure 4.5 Plots of room temperature (a) remanent polarization and (b) coercive field as a function of Zr/Ti ratio for 2, 4, and 6 μm PZT films.

4.3.3 Temperature Dependent Characterization

The ultimate goal of the investigation was to characterize the temperature dependence of the $e_{31,f}$ coefficient of PZT films between -55°C and 85°C. However, it is important to recognize the interrelationship between dielectric, ferroelectric, and piezoelectric properties. For example, it was discussed previously that, intrinsically, the piezoelectric d coefficient is related to the dielectric permittivity and ferroelectric

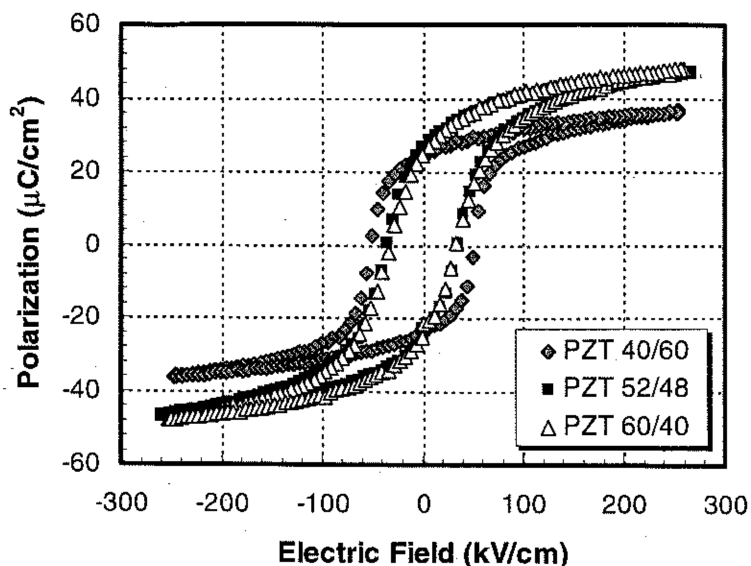

Figure 4.6 Polarization-electric field hysteresis loops for 6 μm PZT films measured at room temperature.

polarization through Equations 1.14 and 1.15 for tetragonal and rhombohedral PZTs. Consequently, a characterization of dielectric and ferroelectric properties between -55°C and 85°C was performed and results were used in rationalizing temperature dependent $e_{31,f}$ data obtained from modified wafer flexure measurements.

4.3.3.1 Low Field Results

4.3.3.1.1 Curie Temperature Determination

Due to effects of residual stresses, substrate clamping, grain size, etc. the Curie temperatures of bulk and film materials of the same composition may not be identical. Because it is known that intrinsic piezoelectric coefficients of PZT increase rapidly near T_c, accurate determination of film T_c's is important in analyzing relative contributions of intrinsic and extrinsic sources to the piezoelectric temperature dependence. High

temperature permittivity measurements are the common method for measuring Curie temperatures of both ceramics and films.

T_c is identified by the maximum in a plot of ε_r as a function of temperature. Figure 4.7 is a plot of measured relative permittivity for the 2 μm-thick PZT films. Curie temperatures determined from this data are given in Table 4.2 (bulk T_c's are included for comparison). Film T_c's were found to follow same trend but were shifted to slightly higher temperatures as compared to ceramic values. Part of this apparent shift could be an artifact of the rapidly rising dielectric loss at high temperatures. This is consistent with the observation that the apparent T_c was higher for lower frequencies, where the loss component was appreciably larger.

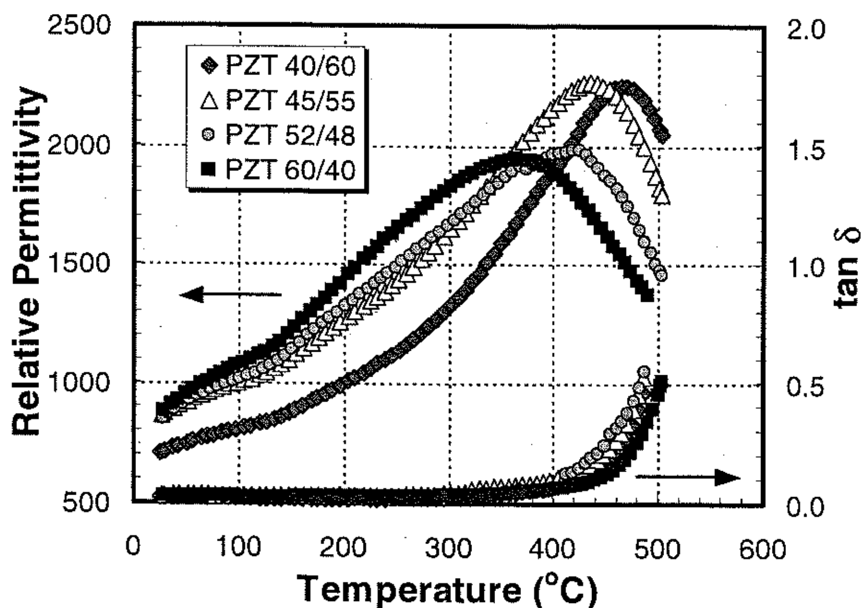

Figure 4.7 Plot of relative permittivity (ε_{33}) of 2 μm PZT films with different Zr/Ti ratios as a function of temperature used in determining Curie temperatures. Measurements were made at 20 kHz and ~0.15 kV/cm.

Table 4.2 Measured Curie temperatures of 2 μm-thick PZT films and bulk PZTs.

	Curie Temperature (°C)			
	PZT 40/60	**PZT 45/55**	**PZT 52/48**	**PZT 60/40**
Films	470	435	420	370
Ceramics*	419	407	399	366

*Ceramic data from Amin *et al.*[32]

4.3.3.1.2 Near Room Temperature Characterization

Figures 4.8 and 4.9 show results of relative permittivity versus temperature measurements carried out between -100°C and 100°C, which are plotted as a function of composition and film thickness, respectively. Data were taken on both heating and cooling (both sets of data are plotted) and it is clear that there was no hysteresis. The temperature dependence of the capacitance was ascribed to the temperature dependence of the permittivity (ε_{33}), since dimensional changes were expected to be small over this range.

In each film, permittivity increased with increasing temperature. Second order polynomial regression fits to the measured data had associated R^2-values > 0.99. Table 4.3 gives the percent increase in permittivity in the range of -55°C and 85°C based on these polynomial regression fits. While the temperature dependence of permittivity over this range was independent of film thickness, it was found to increase with decreasing $PbTiO_3$ content. Average ε_{33} increases were 43%, 35%, and 23% for films with 60/40, 52/48, and 40/60 ratios, respectively.

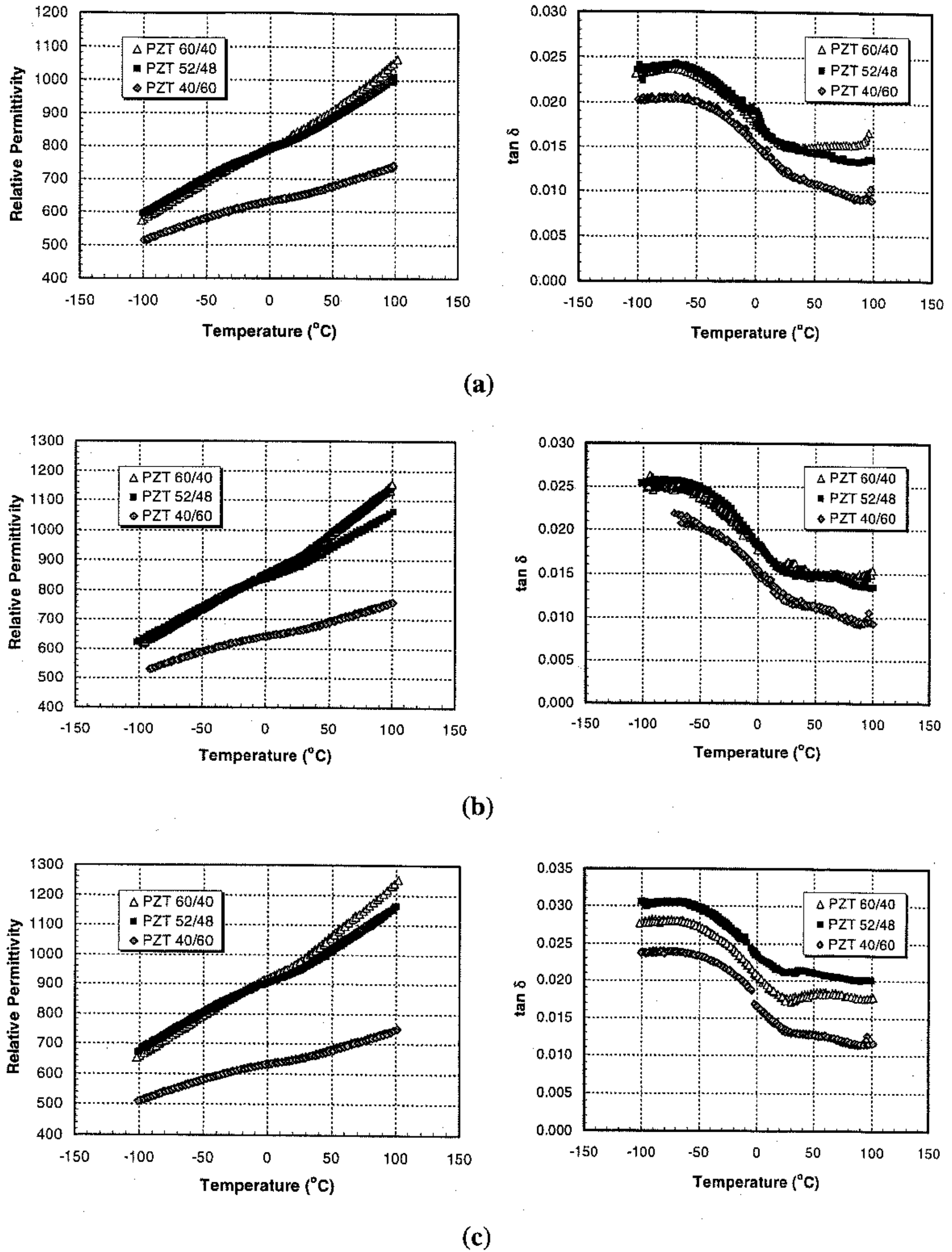

Figure 4.8 Relative permittivity and dielectric loss tangent of Pt/PZT/Pt stack plotted as a function of temperature for (a) 2 μm, (b) 4 μm, and (c) 6 μm films measured at 1 kHz.

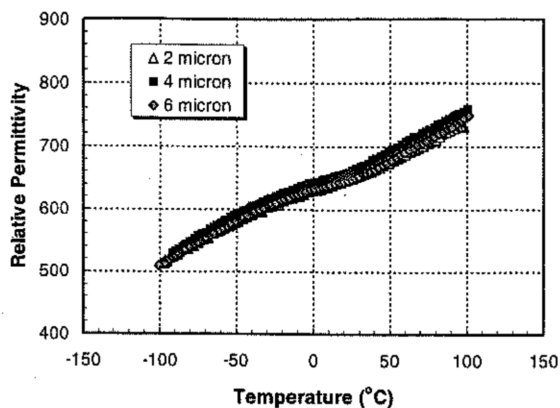

(a)

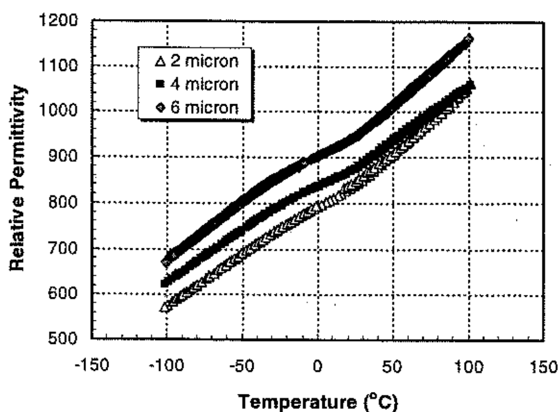

(b)

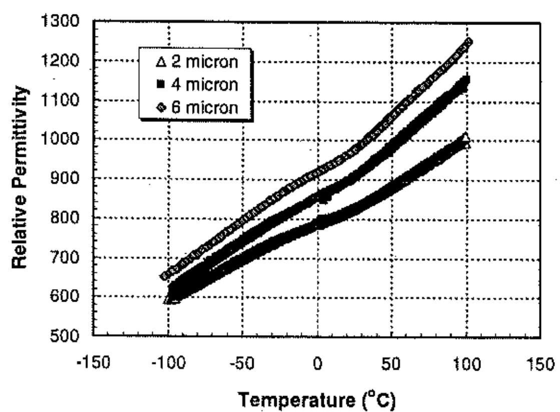

(c)

Figure 4.9 Relative permittivity of Pt/PZT/Pt stack plotted as a function of temperature for (a) PZT 40/60, (b) 52/48, and (c) 60/40 films measured at 1 kHz.

Table 4.3 Percent increase in permittivity from –55 to 85°C based on second order polynomial regression fits to measured data for PZT films.

Composition	*2 μm*	*4 μm*	*6 μm*
PZT 60/40	41 ± 2%	44 ± 3%	43 ± 3%
PZT 52/48	35 ± 2%	34 ± 3%	36 ± 3%
PZT 40/60	23 ± 3%	23 ± 3%	23 ± 3%

This permittivity versus temperature behavior is due to the approach to T_c (Figure 2.14). As a result, for a given temperature range, compositions with lower Curie temperatures are expected to exhibit a greater temperature dependence of permittivity. For the films analyzed, the percent increase in permittivity between -55°C and 85°C was greatest in the films with a Zr/Ti ratio of 60/40 and least in the PZT 40/60 films. This was consistent with the variation in T_c between the bulk compositions (Figure 2.23): PZT 60/40 (366°C), PZT 52/48 (389°C), and PZT 40/60 (419°C). Dielectric loss decreased slightly with increasing temperature but remain ≤3% in all films over the measured range.

The temperature dependence of the permittivity (i.e. slopes of the ε_{33} versus temperature curves) did not appear to be film thickness dependent in any of the films over the measured temperature range.

4.3.3.2 High Field Results

Figures 4.10 and 4.11 present the results of the high field ferroelectric characterization performed as a function of temperature between -55°C and 85°C. Data are plotted as a function of composition and film thickness, respectively. Again, remanent polarization and coercive field values were extracted from P-E hysteresis data.

Measurements were made with the samples held at temperature (5 min temperature stabilization). To illustrate relative changes in P-E loop shape with temperature that were characteristic of all film samples, Figure 4.12 shows P-E loops for the 2 μm PZT 40/60 film measured at -55°C, 15°C, and 85°C. As expected, both remanent polarization and coercive field decreased with increasing temperature.

P_r and E_c exhibited a nearly linear dependence on temperature between -55°C and 85°C. Linear regression fits to the data had associated R^2-values > 0.99. Tables 4.4 and 4.5 give the percent decrease in P_r and E_c, respectively, from -55°C to 85°C based on these fits.

The percent decrease in P_r from -55°C to 85°C was found to be highest in films with the lowest $PbTiO_3$ content. Average values were 34%, 26%, and 17%, in films with Zr/Ti ratios of 60/40, 52/48, and 40/60, respectively. The measured temperature dependence of P_r is consistent with the drop in spontaneous polarization as T_c is approached (Figure 2.15). Accordingly, for a given temperature range, one would expect compositions with lower Curie temperatures to exhibit a greater temperature dependence of remanent polarization.

It is also seen that for each composition, 6 μm films showed the smallest decrease in P_r over the measured range, although differences were slight. This may be due to increased domain contributions in these thicker films.[28] If domain wall motion was significant in these films, the extrinsic contributions to polarization would be expected to increase with temperature (section 2.5.2). This would counteract the intrinsic decrease in P_s, producing a flatter temperature response.

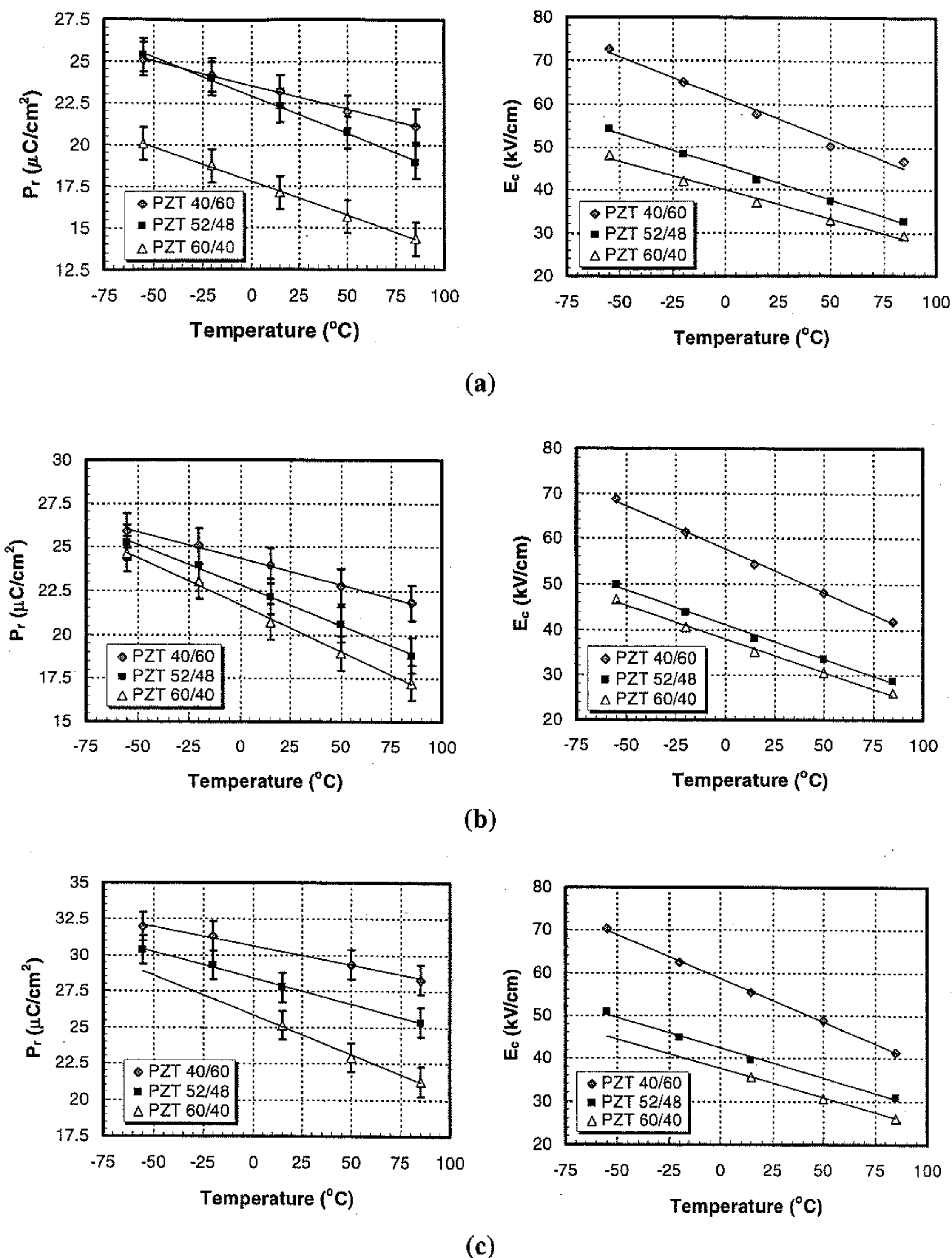

Figure 4.10 Temperature dependence of remanent polarization and coercive field for (a) 2 μm, (b) 4 μm, and (c) 6 μm PZT films. In E_c plots, error bars are nested within symbols.

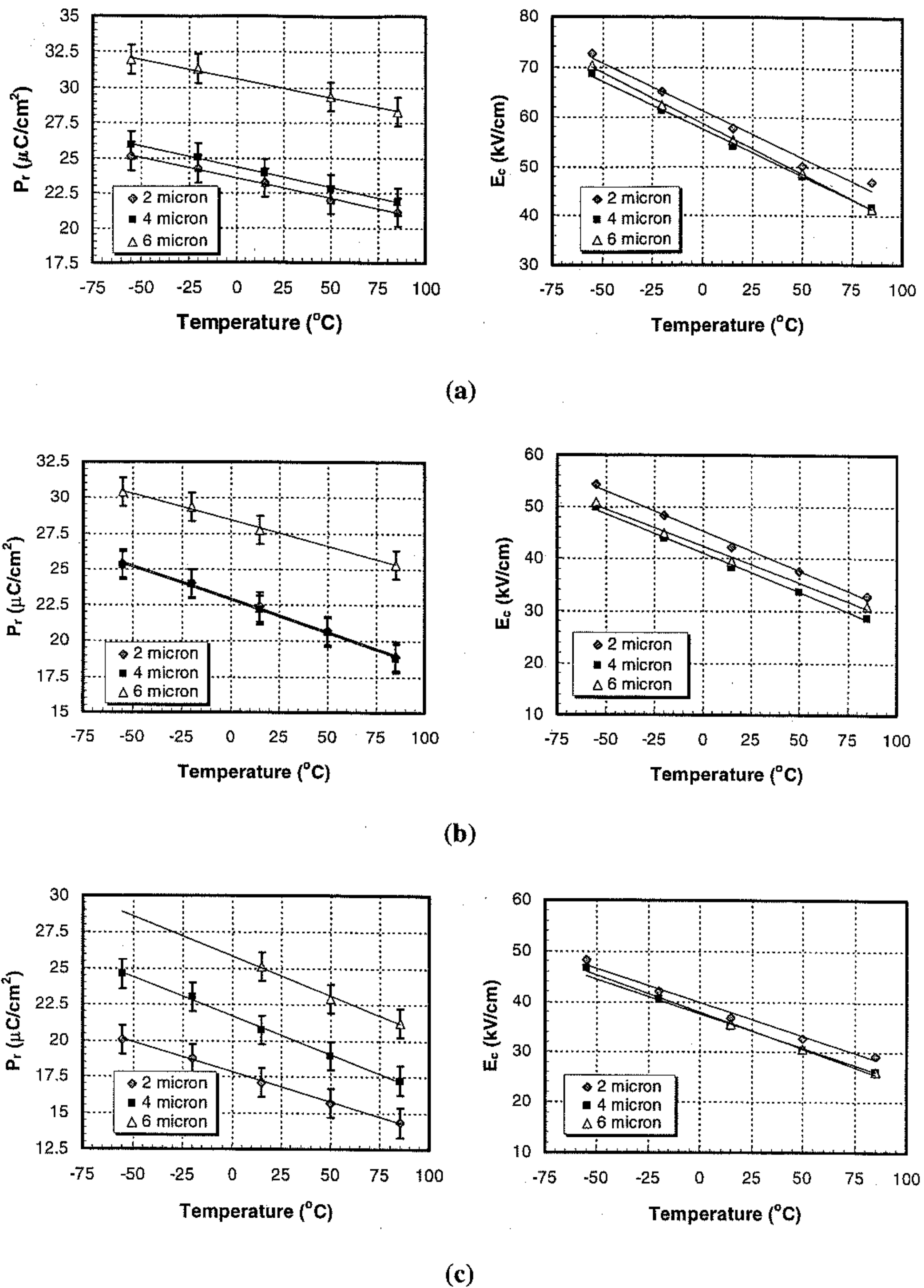

Figure 4.11 Temperature dependence of remanent polarization and coercive field for (a) PZT 40/60, (b) 52/48, and (c) 60/40 films. In E_c plots, error bars are nested within symbols.

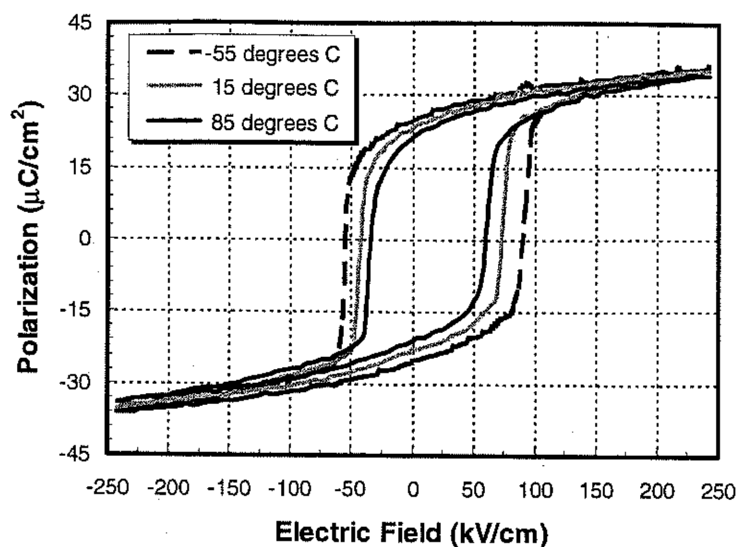

Figure 4.12 Polarization-electric field hysteresis loops as a function of temperature for the 2 μm PZT 40/60 film.

Table 4.4 Percent decrease in remanent polarization from -55°C to 85°C based on linear regression fits to measured data for PZT films.

Composition	*2 μm*	*4 μm*	*6 μm*
PZT 60/40	34 ± 4%	36 ± 5%	31 ± 4%
PZT 52/48	29 ± 5%	29 ± 5%	19 ± 4%
PZT 40/60	18 ± 6%	17 ± 5%	15 ± 5%

Table 4.5 Percent decrease in coercive field from -55°C to 85°C based on linear regression fits to measured data for PZT films.

Composition	*2 μm*	*4 μm*	*6 μm*
PZT 60/40	50 ± 2%	57 ± 2%	54 ± 2%
PZT 52/48	50 ± 2%	54 ± 2%	50 ± 2%
PZT 40/60	46 ± 1%	49 ± 1%	51 ± 1%

Table 4.6 gives both the percent change in P_s predicted by phenomenology (Figure 2.15) and the average measured decrease in P_r between -55°C and 85°C for each film composition. Trends in P_r are consistent with those in P_s, with PZT 60/40 films showing the largest temperature dependence, followed by PZT 52/48 and 40/60, respectively. However, for all Zr/Ti ratios, decreases in P_r over the measured temperature range are larger than decreases in P_s. The origin of this behavior is unclear. Nonetheless, results suggest that even under high field excitation, over the temperature range probed, there is no strong evidence for significantly increased non-180° domain wall motion (at least on the time scale of a P-E hysteresis measurement). If domain wall contributions had been significant, one would expect a weaker temperature dependence of P_r, not a stronger one such as that observed.

Table 4.6 Normalized percent changes in P_s predicted by phenomenology on heating from -55°C to 85°C based on PZT Zr/Ti ratio. Measured P_r values are shown for comparison.

Composition	*ΔP_s (calculated)*	*ΔP_r (measured)*
PZT 60/40	-17%	-34 ± 7%
PZT 52/48	-16%	-26 ± 8%
PZT 40/60	-10%	-17 ± 5%

4.4 Piezoelectric Characterization

In this section, the effective transverse piezoelectric coefficients $e_{31,f}$ of all films were characterized both at room temperature and as a function of temperature between -55°C and 85°C. Room temperature measurements were carried out using the wafer

flexure technique as described by Shepard *et al.*[3] Additionally, in light of the results obtained by Dubois *et al.*[30] in which the maximum $|e_{31,f}|$ coefficient occurred at the PZT 45/55 composition in ~900 nm <111> oriented sol-gel films (discussed in section 2.8.2), a 2 μm PZT 45/55 film was prepared by the method described in section 3.2 and its room temperature $e_{31,f}$ was measured.

$e_{31,f}$ measurements of films as a function of temperature between -55°C and 85°C were made using the modified wafer flexure method.

4.4.1 Room Temperature $e_{31,f}$ Characterization

Figure 4.13 shows the results of the room temperature $e_{31,f}$ characterization by the wafer flexure method. Measurements were taken ~30 s after removal of the poling field ($3E_c$) and, as a result, values approximate deaged piezoelectric coefficients.

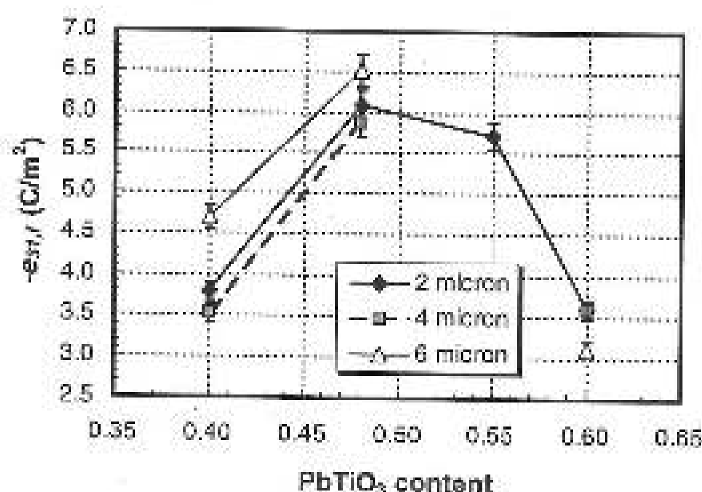

Figure 4.13 Room temperature transverse piezoelectric coefficient $e_{31,f}$ as a function of Zr/Ti ratio for 2 μm, 4 μm, and 6 μm PZT films.

The maximum $|e_{31,f}|$ was observed at the PZT 52/48 composition. Maximum electromechanical activity at the MPB is characteristic of bulk PZT ceramics (section 2.8.1). These data are also in agreement with the results of Chen[38] (1 μm sol-gel PZT films over a wide composition range) and Xu[28] (1 μm, <111> and <100> sol-gel PZT films near the MPB).

As mentioned previously, Dubois[30] (Figure 2.29) found $e_{31,f}$ to be a maximum on the tetragonal side of the phase boundary (PZT 45/55). Consequently, a 2 μm PZT 45/55 film was prepared and its room temperature $e_{31,f}$ was characterized in this study. $e_{31,f}$ of the 52/48 composition was found to be slightly higher that that of the 45/55 (6.09 and 5.71 C/m^2, respectively). It is possible that the observed disparity in the composition of maximum piezoelectric activity is due to differences in the concentration or distribution of orientable defect dipoles (i.e. $V_{Pb}'' - V_O^{\bullet\bullet}$) or space charges, asymmetric electrodes, poling efficiency[53] (especially in sputtered films), or grain size.

4.4.2 Temperature Dependent Piezoelectric Characterization

The modified wafer flexure technique was used to ascertain the temperature dependence of the transverse piezoelectric coefficient $e_{31,f}$ in the range of -55°C to 85°C. It is important to reiterate that all films were well-aged (≥3 days) prior to measurement. Measurements were made on both heating and cooling and for each film, the charge output from 2 to 3 leaded electrodes (all 1.1 cm from wafer center) was monitored in separate experiments.

4.4.2.1 Electrode-to-Electrode Uniformity

Figure 4.14 presents piezoelectric coefficient data collected from three distinct electrodes in three separate temperature experiments on a 2 µm PZT 60/40 film. Measured $e_{31,f}$ coefficients were normalized to their room temperature values and plotted as a function of temperature for each film.

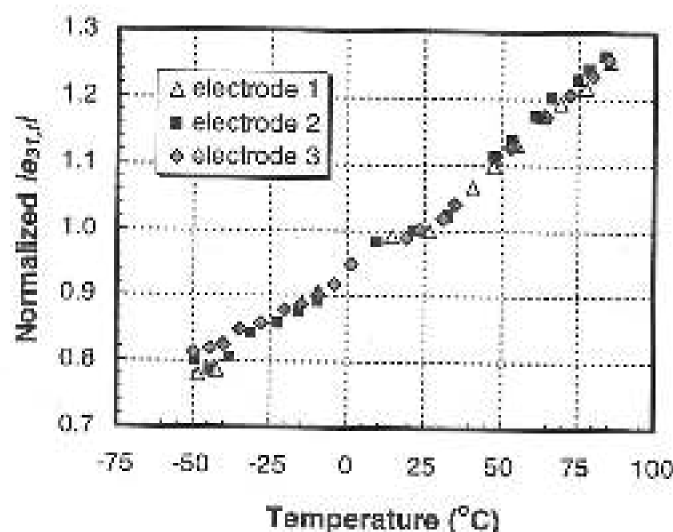

Figure 4.14 Plot of normalized $|e_{31,f}|$ as a function of temperature for a 2 µm PZT 60/40 film. Data were collected from three distinct electrodes (denoted 1, 2, and 3) during three separate experiments.

No significant hysteresis was observed in the measured data during temperature cycling, which indicated minimal depoling. Second order polynomial regression fits to data from each electrode were used to determine the percent increase in $|e_{31,f}|$ from -55°C to 85°C. For the 2 µm PZT 60/40 film, electrodes 1, 2, and 3 (Figure 4.14) yielded $|e_{31,f}|$ increases of 50%, 49%, and 44%, respectively. This resulted in a variation of ±3%. Electrode-to-electrode uniformities were calculated similarly for all films and variations were between ±1% and ±5%.

4.4.2.2 Wafer-to-Wafer Uniformity

Additionally, the wafer-to-wafer uniformity was determined. Two PZT 52/48 films, 2 μm in thickness were prepared on 3" Pt-coated Si wafers. Electrodes were deposited and room temperature dielectric, ferroelectric, and piezoelectric properties were measured. Variations in permittivity, remanent polarization, and $e_{31,f}$ were ±0.7%, ±2.1%, and ±1.8%, respectively. Subsequently, strain gages were affixed and temperature dependent $e_{31,f}$ measurements of 2 electrodes (from each film) were made. When data were averaged for each film, the percent increases in $|e_{31,f}|$ from -55°C to 85°C were determined to be 28% and 39%. This resulted in wafer-to-wafer variation of nearly ±6%.

It is believed that this uncertainty hinged primarily on the ability to duplicate the clamping conditions after removing a wafer from the rig (as described in section 3.6.2.4). Based on this experiment, and depending on the magnitude of the $e_{31,f}$ change over the temperature range, wafer-to-wafer uniformities for all films were expected to be in the range of ± 3–12%.

4.4.2.3 Temperature Dependence of $e_{31,f}$

Figure 4.15 shows plots of normalized $|e_{31,f}|$ as a function of temperature for PZT 60/40, 52/48, and 40/60 films for each film thickness. Second order polynomial regression fits to the measured $|e_{31,f}|$ versus temperature data had associated R^2-values > 0.98. Data collected from all measured electrodes for each film were averaged. Table 4.7 gives the percent increase in $|e_{31,f}|$ coefficient from -55°C to 85°C based on these polynomial fits.

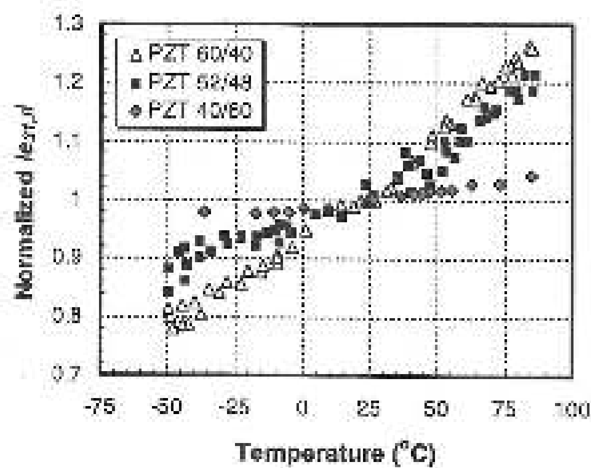

(a)

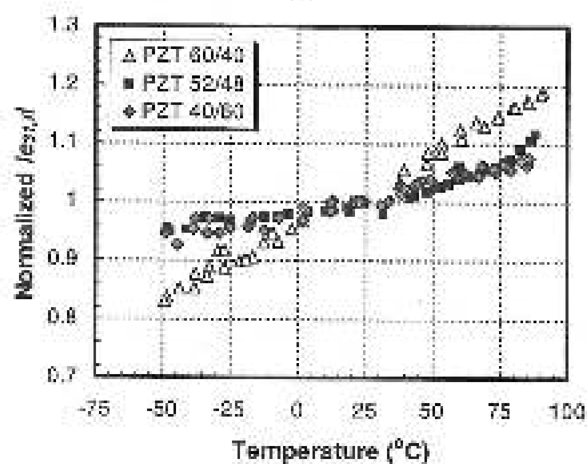

(b)

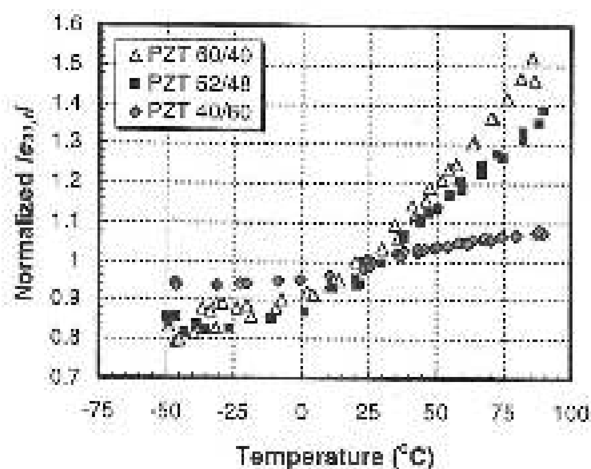

(c)

Figure 4.15 Temperature dependence of normalized $|e_{31,f}|$ for (a) 2 μm, (b) 4 μm, and (c) 6 μm PZT films measured using the modified wafer flexure technique.

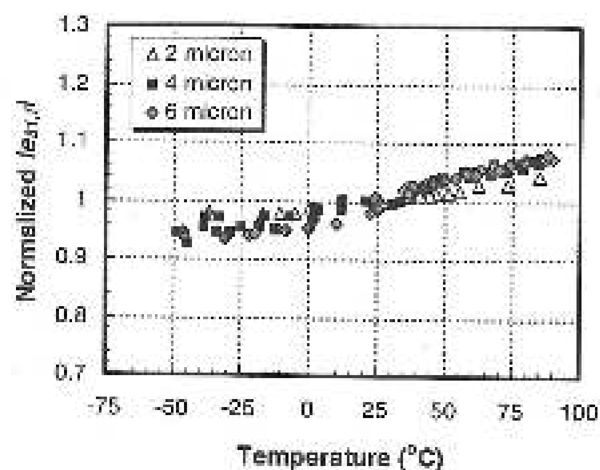

(a)

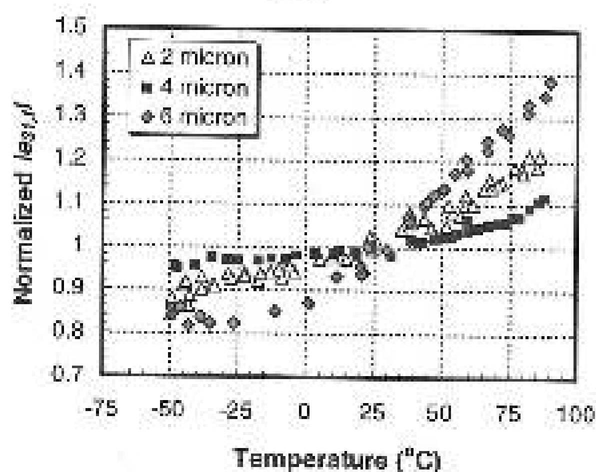

(b)

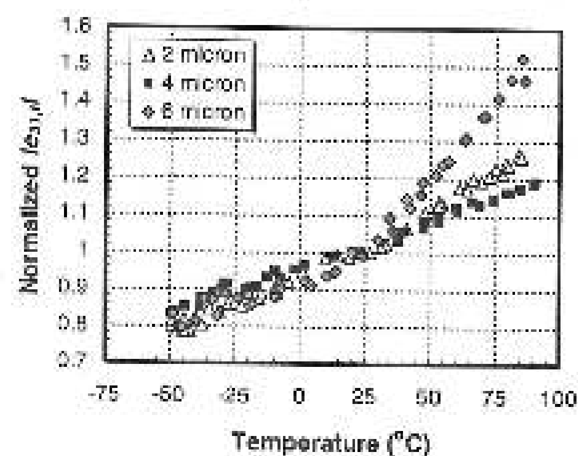

(c)

Figure 4.16 Temperature dependence of normalized $|e_{31,f}|$ for (a) PZT 40/60, (b) 52/48, and (c) 60/40 films measured using the modified wafer flexure technique.

Table 4.7 Percent increase in $|e_{31,f}|$ from −55°C to 85°C based on second order polynomial regression fits to measured data for PZT films.

Composition	*2 μm*	*4 μm*	*6 μm*
PZT 40/60	7 ± 3%	13 ± 4%	16 ± 5%
PZT 52/48	29 ± 7%	17 ± 5%	49 ± 11%
PZT 60/40	48 ± 10%	34 ± 8%	56 ± 12%

The percent increases in $|e_{31,f}|$ coefficient from -55°C to 85°C show an obvious dependence on composition. For films of a given thickness, the temperature dependence is stronger for decreasing $PbTiO_3$ content. Again, this is consistent with the intrinsic piezoelectric response, which increases rapidly approaching T_c (Figure 2.16).

In all cases, the thickest films (6 μm) exhibited the largest temperature variation, although the changes were comparatively small (particularly for PZT 40/60). Increased non-180° domain wall contributions, in comparison with 2 μm and 4 μm films, may have been the cause. This is consistent with the weaker temperature dependence of P_r measured for these films (section 4.3.3.2).

Results also agree with those of Xu *et al.*[28] where $d_{33,f}$ coefficients of 6.7 μm-thick PZT 52/48 films showed a much stronger dependence on sub-coercive AC electric field (at 1 kHz) as compared to 3.2 and 1.5 μm-thick films of similar grain size (Figure 2.19b). Also, Xu found that for films of ~0.1 μm average grain size, the threshold field for non-180° domain switching (as determined by the onset of the decrease in dielectric constant as a function of DC poling field) decreased with film thickness, indicating reduced non-

180° domain wall pinning in thicker films. Measured threshold fields were 600, 390, and 170 kV/cm for 3.2, 5.2, and 6.5 μm-thick PZT 52/48 films.

Furthermore, and consistent with the above discussion, it is postulated that the temperature dependence of the $e_{31,f}$ coefficient of PZT films will vary with the magnitude of the electric field (or strain) oscillation. Larger oscillations may enable a greater degree of non-180° domain switching and the effects of these increased extrinsic contributions will carry their own temperature dependence, which is added to the intrinsic dependence. The end result may be stronger temperature dependence of $e_{31,f}$ (at least between -55°C and 85°C) with increasing field or strain oscillation magnitude. This could be especially important is describing the temperature dependence of PZT film actuators.

4.5 Factors Affecting Electromechanical Properties of PZT Films During Temperature Cycling Between -55 and 85°C

Temperature dependent electromechanical analysis of a PZT film is complicated by the fact that it is clamped to a rigid substrate. Several factors can be cited that impact its piezoelectric behavior as temperature is varied. These include changes in (1) intrinsic and extrinsic contributions to piezoelectricity, (2) film elastic properties, (3) substrate elastic properties, and (4) the residual stress state. The following section identifies and discusses the contributions of each of these on the measured changes in the $e_{31,f}$ piezoelectric coefficient of the chemical solution deposited PZT films deposited on Si substrates in cycling between -55 and 85°C.

4.5.1 Intrinsic Contributions to Piezoelectricity

Revisiting Equation 2.16, $e_{31,f}$ is directly proportional to d_{31}. As a starting point, it is assumed that the temperature dependence of d_{31} is largely controlled by intrinsic contributions over the measured temperature range, in accordance with Equations 2.14 and 2.15. Table 4.8 gives intrinsic $|d_{31}|$ values as calculated from phenomenology (Figure 2.16) for near MPB compositions. PZT 60/40 exhibits the greatest piezoelectric temperature dependence of the three from -55 to 85°C (+50%).

Table 4.8 Intrinsic d_{31} values of several PZT compositions (from Figure 2.16). The percent increase from -55°C to 85°C is also given.

Zr/Ti ratio	*40/60*	*50/50*	*60/40*
$\|d_{31}\|$ @ -55°C	51 pC/N	134	62
$\|d_{31}\|$ @ 85°C	67 pC/N	180	104
increase	27%	29%	50%

4.5.2 Film Elastic Properties

Equation 2.16 also reveals that $e_{31,f}$ is inversely proportional to the sum of film elastic compliance coefficients, s_{11}^E and s_{12}^E. If it is assumed that ferroelastic wall motion is limited, s_{11} will be dominated by intrinsic sources and, as shown in section 2.7.2, should be relatively stable with temperature. Per Figure 2.26, the greatest temperature dependence from -55 to 85°C was exhibited by the PZT 52/48 composition (increasing by 4%) while compositions further from the MPB showed even lower dependences (1–2%). If domain wall motion were allowed, the temperature variation of $s_{11} + s_{12}$ should be ~4–14% (Figure 2.25). Given these relatively modest changes, it is

believed that the observed temperature dependence of $e_{31,f}$ is dominated by the dependence of d_{31} (Equation 2.16).

4.5.3 Substrate Elastic Properties

The elastic properties of the substrate also change with temperature and this may impact the way in which the PZT film is clamped. McSkimin[54] determined the elastic stiffness coefficients (c_{11}, c_{12}, and c_{44}) of single crystal silicon over a range of temperature using high frequency ultrasonic waves. Measured stiffness coefficients decreased linearly with temperature. On heating from -55 to 85°C, Young's modulus and Poisson's ratio were found to change by –0.3% and +1.3%, respectively.

This type of substrate softening can affect the measured properties of PZT films. A reduction in substrate stiffness with temperature could act to relieve local stresses, which may free up pinned domain walls and result in increased extrinsic contributions to film properties. However, because silicon's elastic constants are not expected to vary appreciably over the measured temperature range (as shown above), it is unlikely that substrate softening had a strong effect on the $e_{31,f}$ versus temperature results measured for PZT films in this study.

4.5.4 Residual Stress State

Cooling a PZT film from its crystallization temperature (~700°C) can give rise to significant residual stresses. A difference in thermal expansion characteristics between film and substrate materials is the primary cause.[55] Equation 4.1 can be used to calculate

the magnitude and sign of the stress (σ) developed through a temperature change (ΔT) based on linear coefficients of thermal expansion (ppm/°C) of the film and substrate.

$$\sigma_{film} = (\frac{E_{film}}{1-\nu_{film}})(\alpha_{substrate} - \alpha_{film})\Delta T \quad (4.1)$$

The thermal expansion coefficient of silicon is about 2.6 ppm/°C.[18] Above the Curie temperature, expansion coefficients of bulk PZTs near the MPB range from 5–10 ppm/°C.[56] Consequently, PZT films are known to be in relatively large tensile states of tensile stress (several hundred MPa) as they are cooled through T_c.[55]

Figure 4.17 plots stress in a PZT 53/47 film deposited on Pt-coated (100) Si below its Curie temperature as measured in wafer curvature measurements.[55] Tensile stress in the film was found to decline as the sample was cooled, which is an indication that the thermal expansion coefficient was slightly lower that that of silicon. This is in agreement with reported thermal expansion coefficients of bulk PZT at the MPB composition (2.0 ppm/°C).[56] However, it should be noted that the high stresses present during formation of the domain structure (at T_c) may act to modify the relative populations of ferroelastic domains within the film plane in an attempt to minimize these stresses (i.e. domain texturing will occur), which will adjust the thermal expansion coefficient from its bulk value. This is particularly important in tetragonal PZT compositions were there is considerable anisotropy in the linear thermal expansion coefficient. Figure 4.18 plots thermal expansion behavior of *a* and *c* axes of the unit cell of PZT 32/68. As temperature increases toward T_c, *a* axes lengthen at the expense of *c* axes.

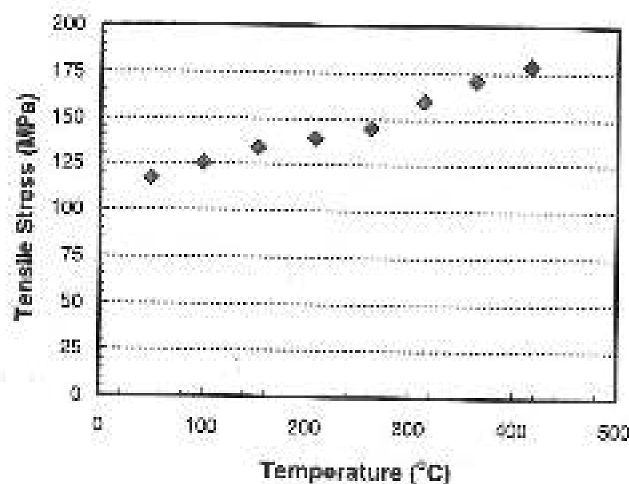

Figure 4.17 Chemical solution deposited PZT 53/47 thin film stress as a function of temperature on cooling from T_c for a film deposited on platinum-coated (100) silicon.[55]

For example, large tensile stress at the Curie temperature may preferentially pull the larger c axes of tetragonal PZT films into the plane, resulting in a large population of a domains. Taking Figure 4.18 into consideration, this will result in a lower thermal expansion coefficient as compared to a randomly oriented bulk sample (where the population ratio of c- to a-domains is 1:2 in any direction).

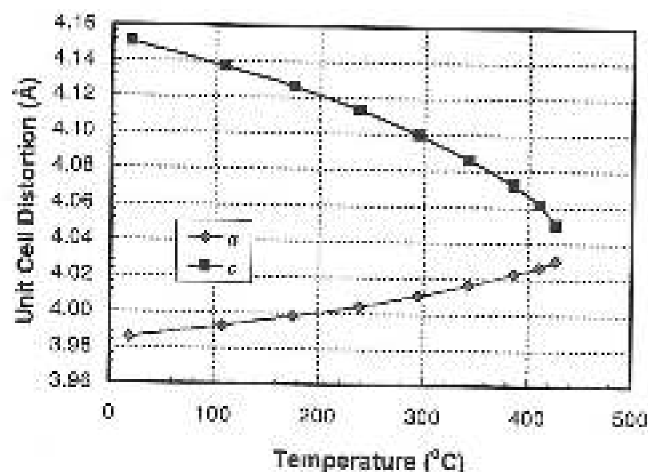

Figure 4.18 Unit cell distortions along a- and c-axes of PZT 32/68 as a function of temperature measured by high temperature powder x-ray diffraction.[26]

Film stress can have a significant impact on measured properties.[57] It is also known that, during $e_{31,f}$ measurements as a function of temperature, the residual stress in the PZT films was changing with temperature. According to the results reported by Tuttle[55] (Figure 4.17), the stress magnitude can vary on the order of 100–200 kPa/°C in a PZT film at the MPB. Between -55 and 85°C, this translates to a non-trivial stress change of ~15–30 MPa.

4.5.5 Biaxial Stress Measurements

An experiment involving the uniform pressure rig (section 3.6.1.3) was designed to assess the impact of biaxial stress changes of this magnitude (tens of MPa) on the piezoelectric response of a PZT film. By attaching a small film sample to a thin aluminum plate and plastically deforming the plate, an external biaxial strain was imposed on the film. The wafer flexure method was then used to measure current output for a given cavity pressure oscillation. Due to the complexity of the sample configuration, it was difficult to calculate film stresses theoretically, and direct strain measurement (using a resistance strain gage) was utilized. The measured ratio of piezoelectric charge output to strain was directly proportional to $e_{31,f}$.

First, a 7 mm × 7 mm square sample was cut from a 2 µm PZT 52/48 film deposited on a Pt-coated Si wafer (processed according to section 3.2) with 1.5 mm-diameter Pt top electrodes (section 3.4.1). A small corner was etched with dilute HF/HCl solution (section 3.4.2) to allow electrical contact to the bottom electrode. The backside of the sample (Si) was then polished until the sample thickness was 175–225 µm. The sample was fixed to the center of an 8 mm-thick, 3.5 in-diameter circular aluminum plate

using a very thin layer of Torr Seal® low vapor pressure resin (Varian Vacuum Technologies, Lexington, MA) and a strain gage was fixed at the center of the film sample (according to section 3.6.2.4). The film was poled at $3E_c$ for 20 min and allowed to age at least 3 days at room temperature. Figure 4.19 shows the sample configuration at this point.

The aluminum plate was placed in the pressure rig and the screws were lightly secured. To impose an external biaxial strain on the film, the cavity was pressurized using an Ar gas tank equipped with a regulator, causing the aluminum plate to deform, both elastically and plastically. Typically, several minutes at pressures as high as 700 kPa were required for the desired level of plastic deformation. Insertion of the aluminum plate into the rig either sample-side-up or sample-side-down controlled the sign of the external strain imposed, tensile or compressive, respectively. After the cavity pressure was released, static film strain caused by the plate deformation was determined using a model 3800 wide range strain indicator (Vishay Instruments Group, Inc., Raleigh, NC).

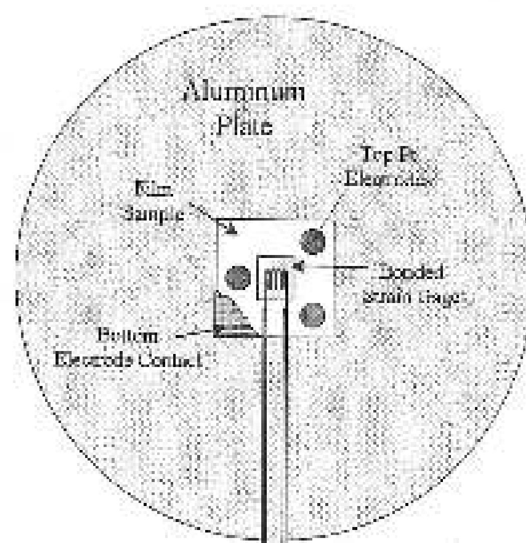

Figure 4.19 Sample preparation for room temperature measurement of $e_{31,f}$ as a function of external biaxial stress (schematic not to scale).

In this way, external biaxial strains between on the order of several hundred microstrain were achieved in the film.

Relative changes in $e_{31,f}$ at each external stain level were quantified by simultaneously measuring current output and strain when an oscillating pressure was driven into the cavity in the setup described in section 3.6.1. Top and bottom electrodes were contacted using point probes. The reference voltage from the lock-in amplifier was increased to 16 V_{RMS} at 4 Hz to raise the periodic strain level (the ratio of film strain to cavity pressure is altered for dome-shaped plates).

Figure 4.20 shows the measured results of the external strain dependence of $e_{31,f}$ for several 2 μm PZT 52/48 films. Assuming a PZT film Young's modulus and Poisson's ratio of 101 GPa and 0.3, respectively,[3] that are constant over the measured strain range, external stresses are calculated and included in the plot. $e_{31,f}$ was found to increase with increasing tensile strain. An increase of ~2% was observed between –300 and +200 με. This is in agreement with findings of Dubois in which $e_{31,f}$ was measured as a function of static strain using a measurement technique based on forced deflection of a PZT film-coated Si cantilever.[30] In that work, an ~8% increase was observed from -800 and +800 με for a 900 nm sol-gel PZT 45/55 film deposited on a Pt-coated Si substrate.

It is believed that during the temperature dependent $e_{31,f}$ measurements made between -55 and 85°C, biaxial strain varied ~15–30 MPa as a result of differences in thermal expansion coefficients between film and substrate materials. Based on the results presented above, this thermal mismatch strain variation is responsible for 1–3% of the measured change in $e_{31,f}$ of the PZT films characterized in this study.

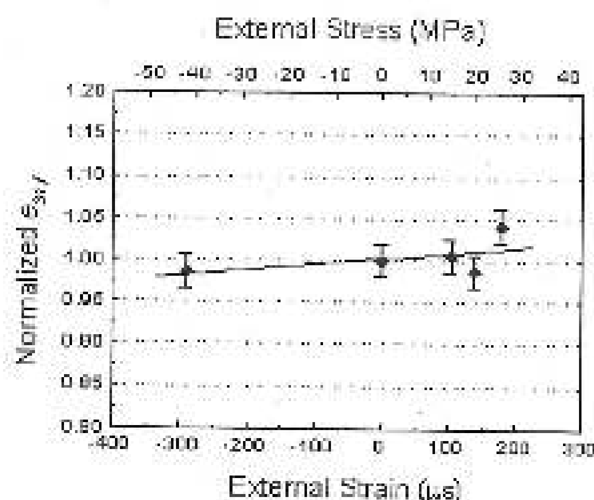

Figure 4.20 Normalized $e_{31,f}$ coefficient of a 2 μm PZT 52/48 film measured at room temperature as a function of external strain. The stress was calculated assuming E = 101 GPa and ν = 0.3 for the PZT film.

4.6 MEMS Accelerometers

Figure 4.21 presents photographs of annular-type MEMS accelerometers that were successfully fabricated in this study. Additional details on the fabrication are given elsewhere.[19]

4.6.1 Frequency Response Results

Figure 4.22 is a frequency response plot for an annular-type MEMS accelerometer. Note the flat frequency response between ~260 Hz and just below the fundamental resonance frequency at 22.1 kHz. The near DC frequency drop-off is a result of piezoelectric charge leakage, a common feature in piezoelectric accelerometers.[13] Observed response versus frequency data for MEMS accelerometers of several types all exhibited similar characteristics with a relatively flat frequency response up to the first resonance frequency.

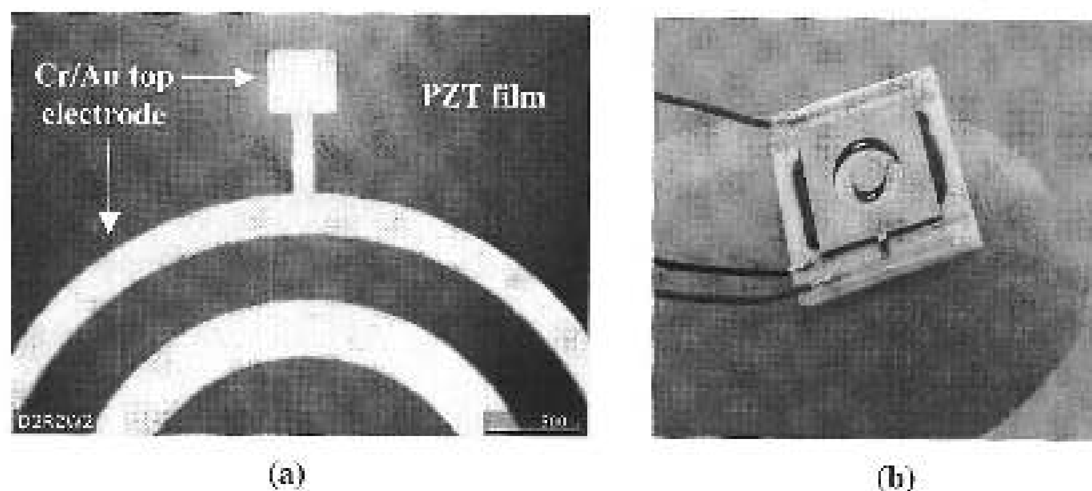

(a) (b)

Figure 4.21 Photographs of (a) frontside and (b) backside processed annular MEMS accelerometers (courtesy of Wilcoxon Research, Inc.).[19] Device packaging is also included in (b).

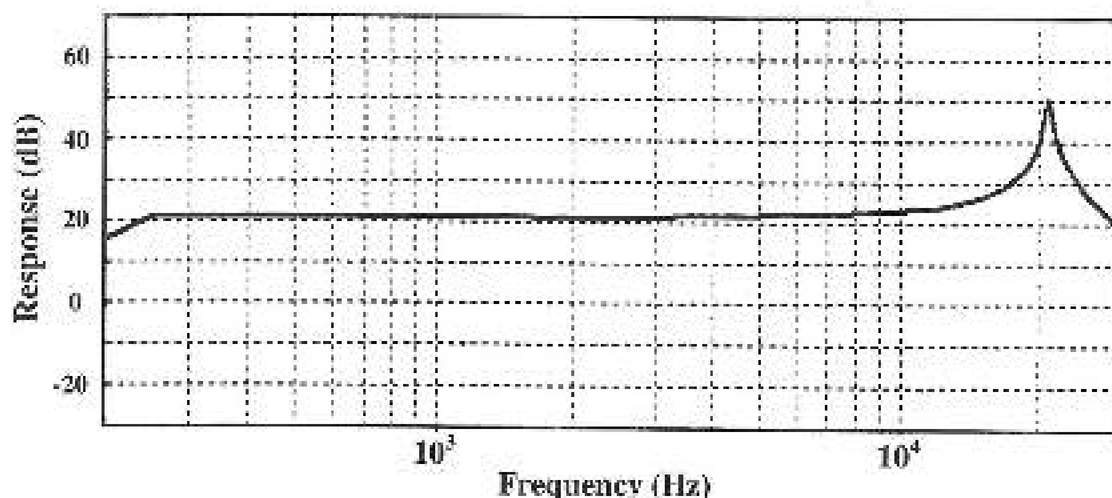

Figure 4.22 Measured frequency response of an annular diaphragm-type MEMS accelerometer. The resonant frequency was 22.1 kHz and the sensitivity was 0.47 pC/g.

Reported sensitivities were chosen at 1 kHz and these are plotted as a function of device resonance frequency in Figure 4.23. These results reemphasize the tradeoff between sensitivity and resonance frequency. As described previously (section 3.5.1), the target resonance frequency and charge sensitivity of the MEMS accelerometer were

≥20 kHz and ≥1.0 pC/g, respectively. Of the MEMS chips fabricated and tested in this study, the highest measured sensitivity for a device with a resonance frequency greater than 20 kHz was 0.52 pC/g (f_R = 21.7 kHz). It may therefore be desirable to use multiple chips, optimize poling efficiency, or increase electrode area to obtain the target charge sensitivity.

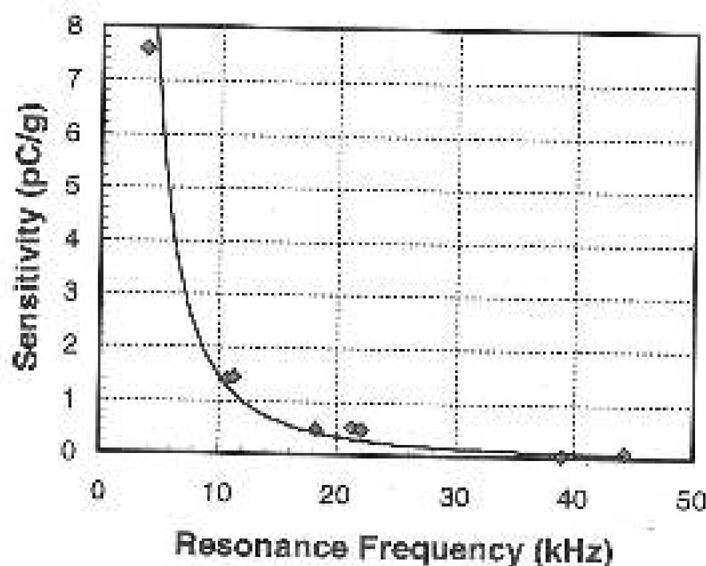

Figure 4.23 Sensitivity plotted as a function of resonance frequency for several types of MEMS accelerometers with varying support beam thicknesses.[19]

4.6.2 Impedance Resonance Results

Impedance resonance measurements were made to (1) double-check resonance frequencies measured using the shaker setup and (2) analyze device resonance frequencies that exceeded the maximum frequency of the shaker (~40 kHz). Figure 4.24 shows one of these curves for a cantilever-type device with a resonance frequency of 8.2 kHz.

Results from frequency response and impedance resonance measurements were in excellent agreement. For all chips tested, device resonance frequencies determined by these two methods were generally within 0.2 kHz (maximum of 0.4 kHz).

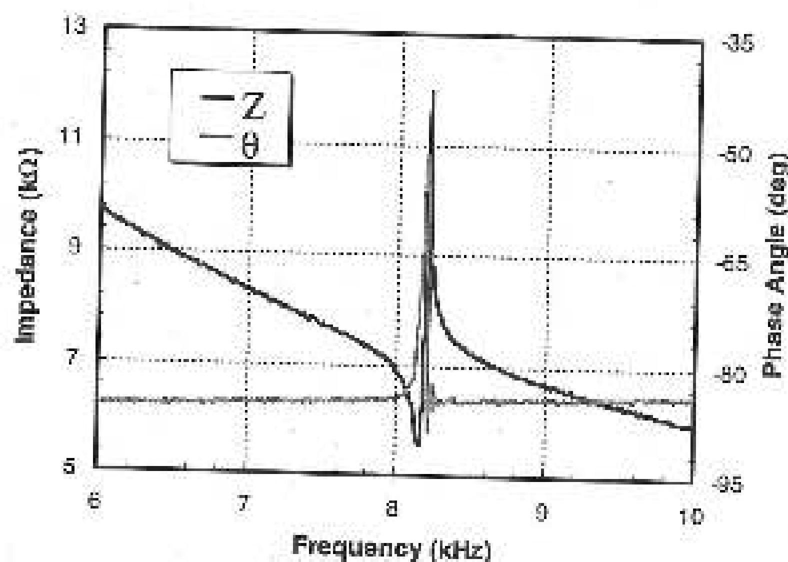

Figure 4.24 Impedance characteristics of a cantilever-type MEMS accelerometer showing fundamental resonance at 8.2 kHz. Z and θ are impedance and phase angle, respectively.

4.6.3 Temperature Considerations

The $e_{31,f}$ measurements of PZT films as a function of temperature reported earlier give insight into the temperature performance of the MEMS accelerometers. The observed piezoelectric coefficient variation with temperature will impact device sensitivity (i.e. accelerometers will be more sensitive above room temperature and less sensitive below). If it is assumed that the temperature dependence of $e_{31,f}$ is dominated by the intrinsic d_{31} response, the sensitivity of a device utilizing a 6 μm PZT 52/48 film will vary about 30% over the temperature specification range. For a device with a

measured sensitivity of 0.5 pC/g at room temperature, this translates to sensitivities of 0.35 and 0.65 pC/g at -55 and 85°C, respectively.

For applications where temperature variations of this magnitude are not tolerable, it may be useful to choose a PZT composition with higher $PbTiO_3$ content (higher T_c). These films will exhibit lower $e_{31,f}$ values (as compared to near MPB compositions) but with weaker temperature dependence. To illustrate this idea, let us assume that a PZT film was chosen to serve the piezoelectric function in a MEMS sensor. Based on the results obtained in this study, the normalized sensitivity and temperature dependence (between -55 and 85°C) are given in Table 4.9.

Table 4.9 Normalized sensitivity and temperature dependence of sensitivity of a hypothetical MEMS sensor involving a piezoelectric PZT film element. Values are based on $e_{31,f}$ vs. temperature data obtained in this study.

Film Composition	*Normalized Sensitivity*	*% Increase in Sensitivity (from -55 to 85°C)*
PZT 52/48	1.00	32%
PZT 45/55	0.97	not measured
PZT 40/60	0.57	12%

Chapter 5 : Conclusions and Future Work

5.1 Conclusions

5.1.1 The Modified Wafer Flexure Technique for Temperature Dependent Measurement of the Effective Transverse Piezoelectric Coefficient $e_{31,f}$ of Films

In this investigation, the wafer flexure technique[3] was modified to allow measurement of the $e_{31,f}$ coefficient of films as a function of temperature between -55 and 85°C (a common device specification). Measurements above room temperature were achieved by uniformly heating the pressure rig using resistive heaters. Low temperature measurements were made in a liquid nitrogen-cooled chamber. A periodic pressure was driven into the cavity below a PZT film-coated Si wafer, producing an oscillating flexure in the wafer.

Previously, the room temperature biaxial strain imposed on the film was calculated using simple plate mechanics and the measured cavity pressure. However, due to differences in thermal expansion characteristics between the pressure rig and the wafer, a modified clamping condition was chosen, which made theoretical modeling of the strain difficult (particularly as the temperature was varied). As a result, strain was measured directly using a strain gage. During measurement, a strain gage, thermocouple, and top electrode were positioned at the same radius near the center of the wafer. By simultaneously monitoring the piezoelectric charge output and the magnitude of biaxial strain in the film (using dual lock-in amplifiers), $e_{31,f}$ was calculated over the -55 to 85°C temperature range.

5.1.2 Temperature Dependent Characterization of the Piezoelectric Behavior of PZT Films on Pt-coated Silicon Substrates Between -55 and 85°C

PZT films of varying thickness (2 μm, 4 μm, 6 μm) and Zr/Ti ratio (40/60, 45/55, 52/48, and 60/40) were prepared on Pt/Ti/SiO_2/Si substrates by chemical solution deposition and rapid thermal annealing. Structural characterization (XRD, SEM, AFM) revealed phase-pure perovskite and an average grain size of 150–200 nm for all films.

Low field dielectric properties of films were determined as a function of temperature over the temperature range of interest (-55 to 85°C). At room temperature, average permittivities of PZT 52/48 and 60/40 films were similar (884 and 908, respectively) and considerably larger than the 40/60 composition (653). Additionally, permittivity increased with film thickness at all Zr/Ti ratios, which may be due to decreased impact of surface or interfacial layers, a decrease in substrate clamping, or increased extrinsic contributions from 180° and non-180° domain walls. In all films, the dielectric loss remained low (≤3%) over the measured temperature range.

The permittivity (ε_{33}) was found to increase linearly with temperature from -55 to 85°C in all films. The temperature dependence was independent of film thickness but showed a strong dependence on composition. Over the measured range, ε_{33} increased by 43%, 35%, and 23% in 60/40, 52/48, and 40/60 compositions, respectively. Differences were attributed to differences in Curie temperatures between compositions, as both intrinsic and extrinsic contributions are known to increase rapidly near T_c.

High field ferroelectric properties were also measured between -55 and 85°C. Room temperature remanent polarizations were found to increase with both thickness and

$PbTiO_3$ content. Measured coercive fields also increased with $PbTiO_3$ content. E_c was independent of film thickness.

The remanent polarization decreased linearly with temperature over the measured range. The greatest variability was observed in films with the lowest $PbTiO_3$ content. On average, P_r decreased by 34%, 26%, and 17% for films with PZT 60/40, 52/48, and 40/60 compositions, respectively.

The wafer flexure technique was used to determine room temperature $e_{31,f}$ coefficients. At each film thickness, maximum $|e_{31,f}|$ values were observed at the PZT 52/48 composition, which is a result consistent with available data for ceramic PZTs. The thickest (6 μm) PZT 52/48 film exhibited the largest $e_{31,f}$ value (-6.5 C/m^2).

The temperature dependence of $|e_{31,f}|$ was characterized from -55 and 85°C by the modified wafer flexure technique. In all films, $|e_{31,f}|$ was found to increase with temperature and average increases were 46%, 32%, and 12% for films with PZT 60/40, 52/48, and 40/60 compositions, respectively. Within films of a given composition, the thickest (6 μm) films exhibited the highest temperature dependences. Uncertainty in these measurements ranged from ±3–12%. Similar to the behavior of ε_{33} and P_r, the greatest variability in $e_{31,f}$ was observed in films with lower $PbTiO_3$ content. This is best explained by the fact that PZTs with lower $PbTiO_3$ content have lower T_c values. For a set temperature range, these compositions are influenced to a greater extent by the sharp rise in intrinsic piezoelectric activity near T_c.

In addition, potential contributors to the measured variation in electromechanical response of the PZT films between -55 and 85°C were identified and discussed. These included changes in film elastic properties, substrate elastic properties, and the biaxial

stress state of the film. Consistent with the intrinsic compliance behavior PZT with temperature, it was postulated that film softening was responsible for decreasing $e_{31,f}$ by 1–4% in heating from -55 to 85°C. Due to the relatively small changes calculated for Si elastic constants over the measured temperature range (E and ν changed 0.3% and 1.3%, respectively), it is unlikely that substrate softening produced substantial changes in $e_{31,f}$. Finally, changes in the biaxial stress in the film caused by the film/substrate thermal expansion mismatch were expected to influence the measured $e_{31,f}$ versus temperature results. Measurements of normalized $e_{31,f}$ as a function of externally imposed biaxial film strain were made with the uniform pressure rig and used to quantify the residual stress contribution. Based on the results obtained for a 2 μm PZT 52/48 film, changes in biaxial film stress with temperature are expected to account for 1–3% of the measured increase in $e_{31,f}$ from -55 to 85°C.

To the best of our knowledge, this is the first comprehensive study focusing on the temperature dependence of the electromechanical response of PZT films.

5.1.3 Piezoelectric MEMS Accelerometers Involving PZT Films

The other aspect of this study was to design, fabricate, and characterize MEMS accelerometers that utilized chemical solution deposited thick PZT films as the active piezoelectric sensing element. It was a cooperative effort involving groups at Penn State University and Wilcoxon Research, Inc. This is the first known MEMS device that combines thick PZT films with deep-trench reactive ion etch (DRIE) processing.

The charge sensitivity and resonance frequency of the MEMS chips were analyzed using frequency response and impedance resonance measurements, which

excited responses both mechanically and electrically, respectively. As expected, there was a tradeoff between sensitivity and resonance frequency. This was largely controlled by variations in diaphragm thickness within the annular sensing structure. The highest measured sensitivity for a device with a resonance frequency ≥20 kHz was ~0.5 pC/g. The device with the highest sensitivity (7.6 pC/g) had an associated resonance frequency of ~4 kHz.

The temperature dependent $e_{31,f}$ measurements discussed previously were used to predict the influence of temperature on the MEMS accelerometer sensitivity. It was suggested that changes in $e_{31,f}$ with temperature could be approximately treated by changes in the intrinsic d_{31} calculated from ferroelectric phenomenology. For the MEMS accelerometer using a 6 μm PZT 52/48 film, the measured sensitivity is thus expected to increase about 30% from -55 to 85°C. In addition, it was suggested that PZT film compositions with higher $PbTiO_3$ contents may be desirable in applications where a relatively stable piezoelectric response with temperature is of paramount importance.

5.2 Recommendations for Future Work

5.2.1 Investigation of the Stress Dependence of Non-180° Domain Wall Mobility

Due to the ferroelastic nature of domains in PZT, film stresses have a profound effect on non-180° domain wall contributions to piezoelectricity.[2] The film/substrate thermal expansion mismatch has been identified as the major contributor to residual stresses that arise in PZT films on cooling from the crystallization temperature into the ferroelectric phase.

Based on the findings of several authors,[47,55] the residual tensile stress in near-MPB composition PZT films deposited on silicon is assumed to be on the order of ~100 MPa at room temperature. A tensile stress of this magnitude may act to pull the ferroelectric polarization into the plane of the film, making field- or stress-induced non-180° domain switching more difficult.

An interesting study would be to determine the absolute magnitude of tensile and compressive stresses at which extrinsic contributions to the piezoelectric effect in thick PZT films (i.e. non-180° domain wall motion) are eliminated and whether the drop-off is abrupt or gradual. This could be accomplished by measuring the external stress dependence of $e_{31,f}$ of PZT films deposited on substrate with various coefficients of thermal expansion. External stress dependent piezoelectric measurements were made in this investigation and the magnitude of external strains obtainable were in the range of ±300–400 με (roughly equivalent to ±40–60 MPa), relative to the initial residual stress. Stress dependent $e_{31,f}$ measurements of films deposited on substrates with a range of thermal expansion coefficients would vary this starting point and enable determination of the piezoelectric response of PZT films across a wider range of stress states (potentially ±several hundred MPa). It would be important in such a case to ensure that as the substrate was varied that all other factors (grain size, film orientation, etc.) remained constant.

Table 5.1 gives the thermal expansion coefficients of several candidate substrate materials[58] and, using Equation 4.1, approximates the stress development in a PZT film of near-MPB composition (1) between the crystallization temperature and T_c and (2) between T_c and room temperature. The following parameters were assumed for the

calculation: film crystallization temperature = 700°C, T_c = 400°C, PZT Young's modulus = 100 GPa, PZT Poisson's ratio = 0.3, $\alpha_{TCE,\ paraelectric\ PZT}$ = 6.7 ppm/°C,[55] $\alpha_{TCE,\ ferroelectric\ PZT}$ = 2.0 ppm/°C.[55] Note that stress relief by ferroelastic domain reorientation may significantly reduce these calculated stresses.

Table 5.1 Approximate magnitudes of film stress developed on cooling as a result of the thermal mismatch between PZT film and substrate. Calculations based on Equation 4.1 using substrate thermal expansion coefficients (from Bever[58]). Stress is given in three columns: 700°C–T_c is the stress developed on cooling from the crystallization temperature to T_c, T_c–25°C is that developed on cooling from T_c to room temperature, and 700–25°C is the total residual stress at room temperature.

		Stress (MPa)		
	$\alpha_{TCE,\ 25\text{-}500°C}$	**700°C–T_c**	**T_c–25°C**	**700–25°C**
Cordierite (non-vitreous)	–1.2	236	43	279
Vitreous cordierite	1.5–2.0	212	13	226
Si	2.6	176	-32	144
Mullite porcelain	4–6	73	-161	-88
High Al_2O_3 (88.5–99.8%)	6–7	9	-241	-233
BeO	7.3–7.6	-32	-292	-324
Sapphire: ⊥ c-axis	7.75	-45	-308	-353
ZrO_2 (fully stabilized)	8.4	-73	-343	-416
MgO	11.6	-210	-514	-724

5.2.2 Introduction of Porosity in Films as a Means of Enhancing Figures of Merit for Specific Applications

Figures of merit for piezoelectric films were discussed in section 2.2.1. It is postulated that the controlled introduction of porosity in various connectivity patterns[59] could potentially be used to optimize film properties and enhance device figures of merit.

To illustrate, experimental results of Seifert[7] have indicated that piezoelectric anisotropy (d_{33}/d_{31}) can be amplified by incorporating porosity in $Pb_{0.85}Ca_{0.15}TiO_3$ (PCT) films. $d_{33,f}$ was found to *increase* with increasing pore fraction.
with measured values of 40 and 57 pm/V for 96% and 75% dense films, respectively. These results are in opposition with those predicted by mixing rules for 0–3 and 3–3 ceramic composites[60], most likely due to effects of substrate clamping. A possible explanation for these observations may be that the porous film is effectively behaving as a 1–3 composite where the film is well-connected in the thickness direction but only weakly-connected within the plane. Reduced coupling within the plane of the film would act to suppress the transverse piezoelectric response. High piezoelectric anisotropy such as this is attractive for biomedical transducer applications.

Pertaining to this investigation, as described in section 3.5, high piezoelectric coupling and low permittivity were required of the PZT film for maximum charge sensitivity in the microaccelerometer. These requirements were realized by increasing the film thickness. An alternate approach would have been to introduce a controlled amount of porosity in the film such that increasing the pore fraction would increase the piezoelectric coefficient-to-permittivity ratio. Varying the heating rate during the

crystallization anneal[7] and spin coating in a humid atmosphere[61] are two ways that have been shown to introduce porosity in chemical solution deposited PZT films.

An attempt was made to impart porosity in PZT films by varying the temperature of the first pyrolysis (300°C to 475°C). The governing assumption was that at higher temperatures, solvent evaporation proceeds faster than film shrinkage and densification, a situation that leads to pore formation. Figure 5.1 presents the results of this preliminary study. The observed increase in final layer thickness (following pyrolyses and RTA anneal) with pyrolysis temperature was attributed to increased porosity. It appears that $e_{31,f}$ decreases faster than the permittivity, which makes porous films of this type undesirable for the MEMS accelerometer application.

5.2.3 Doping to Modify Dielectric and Piezoelectric Responses in Thick Ferroelectric Films

The addition of dopants to PZT ceramics is used to optimize particular properties of interest for commercial applications. For instance, soft doping (where donor ions such as Nb^{5+} or Ta^{5+} substitute for Zr^{4+} and Ti^{4+}, thereby creating V_{Pb}'') improve domain wall mobility, which considerably enhances piezoelectric coefficients for transducer applications.[20] Unfortunately, similar results have not been obtained in soft doped PZT thin films. Nb^{5+} additions to ~0.3 μm PZT films have produced only minimal increases in dielectric and ferroelectric properties at best.[62-64] Thus, it is postulated that residual stresses and clamping by the comparatively massive substrate dominated domain wall mobility in these films.

Soft doping of thicker films, or films deposited on a substrate that has been thinned to a dimension comparable to the film thickness, could allow significant domain wall contributions and boost $e_{31,f}$ coefficients. To date, there is no experimental work in this area.

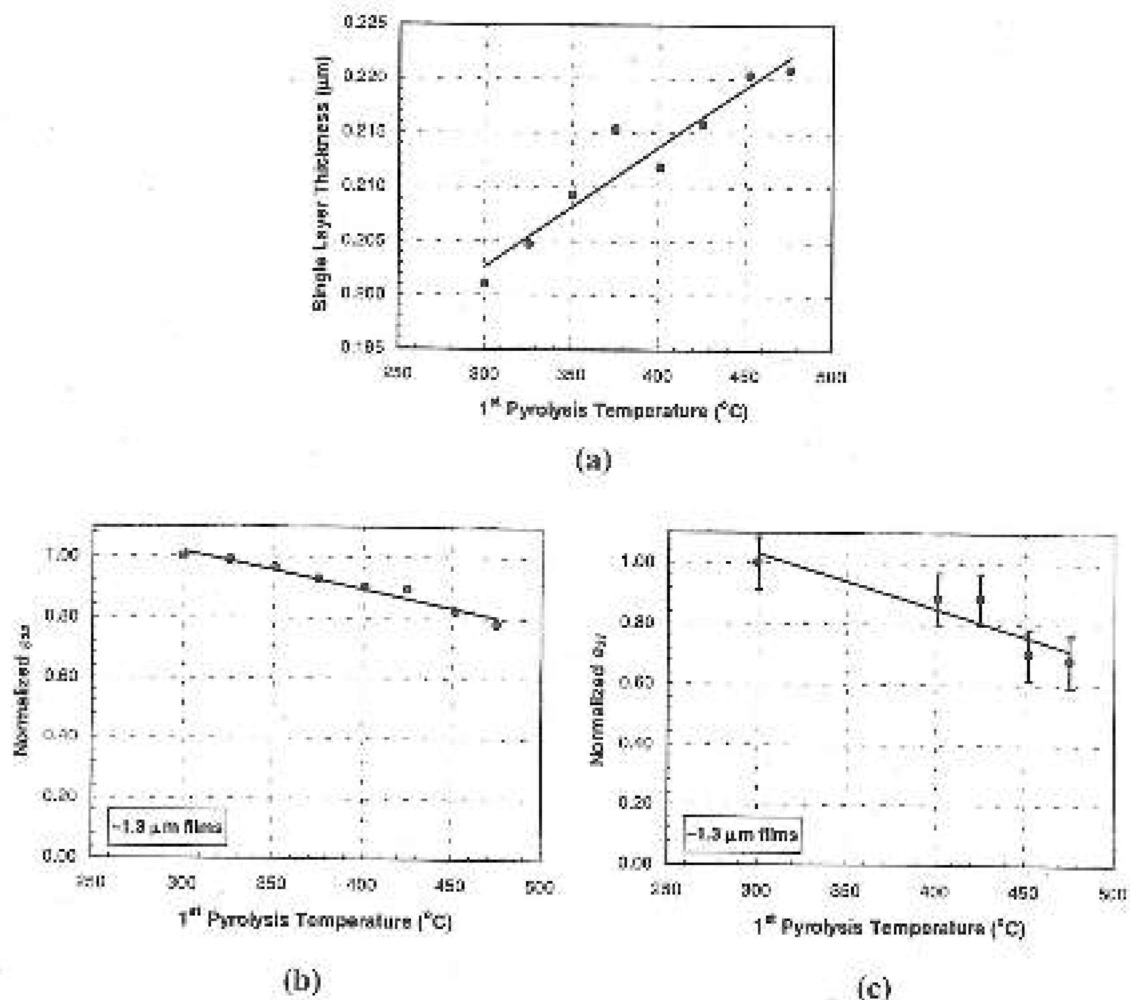

Figure 5.1 PZT film porosity study. The observed layer thickness increase shown in (a) is attributed to an increasing pore fraction. Normalized permittivity ε_{33} and piezoelectric coefficient $e_{31,f}$ plotted in (b) and (c).

References

1 G. T. A. Kovacs, *Micromachined Transducers Sourcebook* (McGraw-Hill, Boston, MA, 1998).

2 S. Trolier-McKinstry, "Piezoelectric Films for MEMS Applications," *J. Ceram. Soc. Jpn.*, **109** [5] S76-S79 (2001).

3 J. F. Shepard, P. J. Moses, and S. Trolier-McKinstry, "The Wafer Flexure Technique for the Determination of the Transverse Piezoelectric Coefficient d_{31} of PZT Thin Films," *Sens. Actuators A*, **71** 133-38 (1998).

4 D. L. Polla and L. F. Francis, "Ferroelectric Thin Films in Microelectromechanical Systems Applications," *MRS Bulletin*, **21** [7] 59-65 (1996).

5 P. Muralt, M. Kohli, T. Maeder, A. Kholkin, K. G. Brooks, N. Setter, and R. Luthier, "Fabrication and Characterization of PZT Thin-Film Vibrators for Micromotors," *Sens. Actuators A*, **48** 157-65 (1995).

6 S. Krishnaswamy, personal communication (2001).

7 A. Seifert, "The Influence of Porosity on the Electromechanical and Pyroelectric Properties of Ca-Modified $PbTiO_3$ Thin Films," *J. Sol-Gel Sci. Tech.*, **16** 13-20 (1999).

8 N. Yazdi, F. Ayazi, and K. Najafi, "Micromachined Inertial Sensors," *Proceedings of the IEEE*, **86** [8] 1640-59 (1998).

9 A. Partridge, J. K. Reynolds, B. W. Chui, E. M. Chow, A. M. Fitzgerald, L. Zhang, N. I. Maluf, and T. W. Kenny, "A High-Performance Planar Piezoresistive Accelerometer," *J. Microelectromech. Syst.*, **9** [1] 58-66 (2000).

10 N. Yazdi and K. Najafi, "An All-Silicon Single-Wafer Micro-g Accelerometer with a Combined Surface and Bulk Micromachining Process," *J. Microelectromech. Syst.*, **9** [4] 544-50 (2000).

11 A. Iula, N. Lamberti, and M. Pappalardo, "Analysis and Experimental Evaluation of a New Planar Piezoelectric Accelerometer," *IEEE/ASME Transactions on Mechatronics*, **4** [2] 207-12 (1999).

12 P. Muralt, "PZT Thin Films for Microsensors and Actuators: Where Do We Stand?," *IEEE Trans. Ultrason., Ferroelect., Freq. Contr.*, **47** [4] 903-15 (2000).

13 P. L. Chen, R. S. Muller, and A. P. Andrews, "Integrated Silicon PI-FET Accelerometer with Proof Mass," *Sens. Actuators*, **5** 119-26 (1984).

14 Y. Nemirovsky, A. Nemirovsky, P. Muralt, and N. Setter, "Design of a Novel Thin-Film Piezoelectric Accelerometer," *Sens. Actuators A*, **56** 239-49 (1996).

15 R. de Reus, J. O. Gulløv, and P. R. Scheeper, "Fabrication and Characterization of a Piezoelectric Accelerometer," *J. Micromech. Microeng.*, **9** 123-26 (1999).

16 D. L. DeVoe and A. P. Pisano, "Surface Micromachined Piezoelectric Accelerometers (PiXLs)," *J. Microelectromech. Syst.*, **10** [2] 180-86 (2001).

17 S. P. Beeby, N. Ross, and N. M. White, "Design and Fabrication of a Micromachined Silicon Accelerometer with Thick-Film PZT Sensors," *J. Micromech. Microeng.*, **10** 322-28 (2000).

18 S. Wolf and R. N. Tauber, *Silicon Processing for the VLSI Era*, 2nd ed. (Lattice Press, Sunset Beach, CA, 2000).

19 L.-P. Wang, "Microelectromechanical Systems (MEMS) Sensors Based on Lead Zirconate Titanate (PZT) Films," *Ph. D. Thesis* (The Pennsylvania State University, University Park, PA, 2001).

20 B. Jaffe, W. R. Cook, and H. Jaffe, *Piezoelectric Ceramics* (R.A.N. Publishers, Marietta, OH, 1971).

21 A. J. Moulson and J. M. Herbert, *Electroceramics: Materials, Properties, Applications* (Chapman and Hall, London, 1990).

22 B. Noheda, J. A. Gonzalo, L. E. Cross, R. Guo, S.-E. Park, D. E. Cox, and G. Shirane, "Tetragonal-to-Monoclinic Phase Transition in a Ferroelectric Perovskite: The Structure of $PbZr_{0.52}Ti_{0.48}O_3$," *Phys. Rev. B*, **61** [13] 8687-95 (2000).

23 F. Jona and G. Shirane, *Ferroelectric Crystals* (Dover Publications, New York, 1993).

24 A. R. Freeman and S. P. Joshi, "The Effect of Nonlinear Stress and Temperature on the Ferroelectric Properties of Perovskites. Part I: Phenomenological Equations," *Ferroelectrics*, **227** [1-4] 1-14 (1999).

25 J. F. Nye, *Physical Properties of Crystals* (Oxford University Press, Oxford, 1985).

26 M. J. Haun, "Thermodynamic Theory of the Lead Zirconate Titanate Solid Solution System," *Ph. D. Thesis* (The Pennsylvania State University, University Park, PA, 1988).

27 X. L. Zhang, Z. X. Chen, L. E. Cross, and W. A. Schulze, "Dielectric and Piezoelectric Properties of Modified Lead Titanate Zirconate Ceramics from 4.2 to 300 K," *Journal of Materials Science*, **18** 968-72 (1983).

28 F. Xu, "Longitudinal Piezoelectric Characterization and Domain Wall Contributions in Lead Zirconate Titanate Thin Films," *Ph. D. Thesis* (The Pennsylvania State University, University Park, PA, 1999).

29 F. Xu, S. Trolier-McKinstry, W. Ren, B. Xu, Z.-L. Xie, and K. J. Hemker, "Domain Wall Motion and its Contribution to the Dielectric and Piezoelectric Properties of Lead Zirconate Titanate Films," *J. Appl. Phys.*, **89** [2] 1336-48 (2001).

30 M.-A. Dubois and P. Muralt, "Measurement of the Effective Transverse Piezoelectric Coefficient $e_{31,f}$ of AlN and $Pb(Zr_x,Ti_{1-x})O_3$ Thin Films," *Sens. Actuators*, **77** 106-12 (1999).

31 A. L. Kholkin, E. K. Akdogan, A. Safari, P.-F. Chauvy, and N. Setter, "Characterization of the Effective Electrostriction Coefficients in Ferroelectric Thin Films," *J. Appl. Phys.*, **89** [12] 8066-73 (2001).

32 A. Amin, M. J. Haun, B. Badger, H. A. McKinstry, and L. E. Cross, "A Phenomenological Gibbs Function for the Single Cell Region of the $PbZrO_3$:$PbTiO_3$ Solid Solution System," *Ferroelectrics*, **65** 107 (1985).

33 D. Wang, Y. Fotinich, and G. P. Carman, "Influence of Temperature on the Electromechanical and Fatigue Behavior of Piezoelectric Ceramics," *J. Appl. Phys.*, **83** [10] 5342-50 (1998).

34 Z. Q. Zhuang, M. J. Haun, S.-J. Jang, and L. E. Cross, "Composition and Temperature Dependence of the Dielectric, Piezoelectric and Elastic Properties of Pure PZT Ceramics," *IEEE Trans. Ultrason., Ferroelect., Freq. Contr.*, **36** [4] 413-16 (1989).

35 L. E. Cross, personal communication (2001).

36 R. Herbiet, U. Robels, H. Dederichs, and G. Arlt, "Domain Wall and Volume Contributions to Material Properties of PZT Ceramics," *Ferroelectrics*, **98** 107-21 (1989).

37 G. Arlt, H. Dederichs, and R. Herbiet, "90-degree Domain Wall Relaxation in Tetragonally Distorted Ferroelectric Ceramics," *Ferroelectrics*, **74** [1-2] 37-53 (1987).

38 H. D. Chen, K. R. Udayakumar, C. J. Gaskey, and L. E. Cross, "Electrical Properties' Maxima in Thin Films of the Lead Zirconate-Lead Titanate Solid Solution System," *Appl. Phys. Lett.*, **67** [23] 3411-13 (1995).

39 D. A. Berlincourt, C. Cmolik, and H. Jaffe, *Proc. IRE*, **48** 220 (1960).

40 F. Xu, F. Chu, and S. Trolier-McKinstry, "Longitudinal Piezoelectric Measurement for Bulk Ceramics and Thin Films Using Pneumatic Pressure Rig," *J. Appl. Phys.*, **86** [1] 588-94 (1999).

41 S. Hiboux, P. Muralt, and T. Maeder, "Domain and Lattice Contributions to Dielectric and Piezoelectric Properties of $Pb(Zr_xTi_{1-x})O_3$ Thin Films as a Function of Composition," *J. Mater. Res.*, **14** [11] 4307-18 (1999).

42 C. D. E. Lakeman and D. A. Payne, "Sol-Gel Processing of Electrical and Magnetic Ceramics," *Materials Chemistry and Physics*, **38** [4] 305-24 (1994).

43 Q. Zhou, E. Hong, R. Wolf, and S. Trolier-McKinstry, "Dielectric and Piezoelectric Properties of PZT 52/48 Thick Films with (100) and Random Crystallographic Orientation," *Mat. Res. Soc. Symp. Proc.*, **655** (2001).

44 K. D. Budd, S. K. Dey, and D. A. Payne, "Sol-Gel Processing of $PbTiO_3$, $PbZrO_3$, PZT, and PLZT Thin Films," *Brit. Ceram. Proc.*, **36** 107-21 (1985).

45 M. Hendrickson, S. Tao, S.Trolier-McKinstry, B. J. Rod, R. J. Zeto, B. M. Kulwicki, A. Amin, and A. Safari, "Processing of PZT Piezoelectric Thin Films for Microelectromechanical Systems," *ISAF '96. Proc. 10th IEEE Int. Symp. Appl. Ferroelect.*, **2** 683-86 (1996).

46 F. Larmar and P. Schilp, Patent DE 4241045, Germany (1994).

47 J. F. Shepard, "The Investigation of Biaxial Stress Effects and the Transverse Piezoelectric (d_{31}) Characterization of Lead Zirconate Titanate Thin Films," *Ph. D. Thesis* (The Pennsylvania State University, University Park, PA, 1998).

48 S. Timoshenko and S. Woinowsky-Krieger, *Theory of Plates and Shells*, 2nd ed. (McGraw-Hill, New York, 1959).

49 W. A. Brantley, "Calculated Elastic Constants for Stress Problems Associated with Semiconductor Devices," *J. Appl. Phys.*, **44** 534-35 (1973).

50 R. G. Polcawich, "Piezoelectric and Dielectric Reliability in Lead Zirconate Titanate Thin Films," *M.S. Thesis* (The Pennsylvania State University, University Park, PA, 1999).

51 S. Li, W. Cao, and L. E. Cross, "The Extrinsic Nature of Nonlinear Behavior Observed in Lead Zirconate Titanate Ferroelectric Ceramic," *J. Appl. Phys.*, **69** [10] 7219-24 (1991).

52 J.-P. Maria, personal communication (2001).

53 M. Kohli and P. Muralt, "Poling of Ferroelectric Thin Films," *Ferroelectrics*, **225** [1-4] 155-62 (1999).

54 H. J. McSkimin, "Measurement of Elastic Constants at Low Temperature by Means of Ultrasonic Waves - Data for Silicon and Germanium Single Crystals, and for Fused Silica," *J. Appl. Phys.*, **24** [8] 988-97 (1953).

55 B. A. Tuttle, J. A. Voigt, T. J. Garino, D. C. Goodnow, R. W. Schwartz, D. L. Lamppa, T. J. Headly, and M. O. Eatough, "Chemically Prepared $Pb(Zr,Ti)O_3$ Thin Films: The Effects of Orientation and Stress," *ISAF '92, Proc. 8th IEEE Int. Symp. Appl. Ferroelect.* 344-48 (1992).

56 G. Shirane, K. Suzuki, and A. Takeda, *J. Phys. Soc. Jpn.*, **7** 12-18 (1952).

57 T. J. Garino and M. Harrington, "Residual Stress in PZT Thin Films and Its Effect on Ferroelectric Properties," *Mat. Res. Soc. Symp. Proc.*, **243** 341-47 (1992).

58 *Encyclopedia of Materials Science and Engineering*; *Vol. 7*, edited by M. B. Bever (Pergamon Press, Oxford, 1986).

59 R. E. Newnham, D. P. Skinner, and L. E. Cross, "Connectivity and Piezoelectric-Pyroelectric Composites," *Mater. Res. Bull.*, **13** 525-36 (1978).

60 D. P. Skinner, R. E. Newnham, and L. E. Cross, "Flexible Composite Transducers," *Mater. Res. Bull.*, **13** 599-607 (1978).

61 J. S. Wright and L. F. Francis, "Processing of Porous Lead Titanate and Lead Zirconate Titanate Coatings," *J. Phys. IV France*, **8** [P9] 27-31 (1998).

62 R. D. Klissurska, A. K. Tagantsev, K. G. Brooks, and N. Setter, "Use of Ferroelectric Hysteresis Parameters for Evaluation of Niobium Effects in Lead Zirconate Titanate Thin Films," *J. Am. Ceram. Soc.*, **80** [2] 336-42 (1997).

63 R. D. Klissurska, K. G. Brooks, I. M. Reaney, C. Pawlaczyk, M. Kosec, and N. Setter, "Effect of Nb Doping on the Microstructure of Sol-Gel-Derived PZT Thin Films," *J. Am. Ceram. Soc.*, **78** [6] 1513-20 (1995).

64 J. L. Lacey, "Effects of Dopants and Microstructure on the Properties of Lead Zirconate Titanate Thin Films Deposited by Pulsed Laser Deposition," *M. S. Thesis* (The Pennsylvania State University, University Park, PA, 1997).